Small-Signal Dynamic Stability Enhancement Of A DC-Segmented AC Power System

by

Sahar Pirooz Azad

A thesis submitted in conformity with the requirements
for the degree of Doctor of Philosophy
Graduate Department of Electrical and Computer Engineering
University of Toronto

Abstract

Small-Signal Dynamic Stability Enhancement Of A DC-Segmented AC Power System

Sahar Pirooz Azad
Doctor of Philosophy
Graduate Department of Electrical and Computer Engineering
University of Toronto
2014

This thesis proposes a control strategy for small-signal dynamic stability enhancement of a DC-segmented AC power system. This control strategy provides four control schemes based on HVDC supplementary control or modification of the operational condition of the HVDC control system to improve the system stability by (i) damping the oscillations within a segment using supplementary current control of a line-commutated HVDC link, based on the model predictive control (MPC) method (control scheme 1), (ii) minimizing the propagation of dynamics among the segments based on a coordinated linear quadratic Gaussian (LQG)-based supplementary control (control scheme 2), (iii) selectively distributing the oscillations among the segments based on a coordinated LQG-based supplementary control (control scheme 3) and (iv) changing the set-points of the HVDC control system in the direction determined based on the sensitivities of the Hopf stability margin to the HVDC links set-points (control scheme 4). Depending on the system characteristics, one or more of the proposed control schemes may be effective for mitigating the system oscillations.

Study results show that (i) control scheme 1 leads to damped low-frequency oscillations and provides fast recovery times after faults, (ii) under control scheme 2, each segment in a DC-segmented system can experience major disturbances without causing adjacent segments to experience the disturbances with the same degree of severity, (iii) control scheme 3 enables the controlled propagation of the oscillations among segments and damps out the oscillatory dynamics in the faulted segment, and (iv) control scheme 4 improves the stability margin for Hopf bifurcations caused by various events.

Since power system software tools exhibit limitations for advanced control design, this thesis also presents a methodology based on MATLAB/Simulink software to (i) systematically construct the nonlinear differential-algebraic model of an AC-DC system, and (ii) automatically extract a linearized state space model of the system for the design of the proposed control schemes. The nonlinear model also serves as a platform for the time-domain simulation of power system dynamics. The accuracy of the MATLAB/Simulink-based AC-DC power system model and time-domain simulation platform is validated by comparison against PSS/E.

Dedication

To my dear parents, Alireza and Marzeyeh, whom I will always be indebted to.

To my loving husband

Kasra

who made it all possible.

Acknowledgements

First and foremost, I would like to express my sincere gratitude to my supervisors, Professor Reza Iravani and Professor Zeb Tate. My first debt of gratitude must go to Professor Reza Iravani for his deep insight, wisdom, invaluable guidance, advice and limitless support during the development of this thesis. His patience and understanding has been an inspiration during my graduate studies.

My deepest gratitude and thanks also go to Professor Zeb Tate who generously dedicated his time and energy to long discussions and without whose help, guidance, encouragement and patience, this dissertation would have never been possible.

I also want to express my thanks for the comments and suggestions provided by the thesis committee members Professor Alexander Prodic, Professor Joshua Taylor, and Professor Peter Lehn.

I also acknowledge the generous financial support I received from the University of Toronto, Professor Iravani and Professor Tate.

Finally, I would also like to thank the members of the Energy Systems Group for valuable advice and instructive discussions.

Contents

List of Tables

List of Figures

Nomenclature

α_{ord}, β_{ord}	rectifier and inverter firing angles
$\bar{\mathbf{I}}$, $\bar{\mathbf{V}}$	vectors of current and voltage phasors of each bus in the DQ reference frame
$\bar{\mathbf{I}}_{inj}$, $\bar{\mathbf{V}}_{inj}$	vectors of current and voltage phasors at the injection buses
$\bar{\mathbf{V}}_{gen}$	vector of voltage phasors at the generator buses
$\bar{V}_t$	terminal voltage phasor in the dq reference frame
$\boldsymbol{\epsilon}$, $\boldsymbol{\nu}$	process and measurement noises
δ	rotor angle with respect to a synchronous reference frame
ω_s, ω	stator and rotor angular frequencies
Ψ	stator flux linkage
Ψ_{1d}, Ψ_{2q}	direct and quadrature axis damper winding flux linkages
$\square_d$, $\square_q$	direct and quadrature axis elements
$\square_{conv}$	inverter/rectifier quantities
$\mathbf{x}_{ac}$, $\mathbf{u}_{ac}$, $\mathbf{y}_{ac}$	AC system state vector, input vector and algebraic variables
$\mathbf{x}_{dc}$, $\mathbf{u}_{dc}$, $\mathbf{y}_{dc}$	DC system state vector, input vector and algebraic variables
$\mathbf{Y}_N$	network admittance matrix
$\mathbf{y}_b$, $\mathbf{u}_b$	output and input vectors of the DC system block
$\mathbf{Y}_{red}$	reduced network admittance matrix
C_{DC}, L_{DC}, R_{DC}	HVDC line parameters

D	damping constant
E_{conv}, γ_{conv}	equivalent generator bus voltage magnitude and angle at the converter internal bus
E_{fd}	field voltage
H	rotor inertia constant
I, V	stator current and voltage
$I_{d_{ref}}$, $V_{d_{ref}}$	rectifier current order and inverter voltage reference
I_{conv}, V_{conv}	converter current and voltage
K_A, T_A	regulator gain and time constant
K_E, T_E, S_E	exciter gain, time constant and saturation
K_F, T_F	rate feedback gain and time constant
$K_{I_{Icon}}$, $K_{P_{Icon}}$	HVDC rectifier current controller integral and proportional gains
$K_{I_{Vcon}}$, $K_{P_{Vcon}}$	HVDC inverter voltage controller integral and proportional gains
n	converter transformer turns ratio
n_{inj}, n_{pas}	number of buses with and without current injection
n_{TG}, n_{dc}	number of T-G units and HVDC links
P_{conv}, Q_{conv}	converter injected active and reactive powers
T_m, T_e	mechanical and electrical torques
T_1, T_3, R	governor time constants and droop
T'_{qo}, T''_{qo}	damper winding transient and subtransient time constants
V_{ref}, P_{ref}	terminal voltage and mechanical power references
$V_{ac_{conv}}$, $\theta_{ac_{conv}}$	AC voltage magnitude and angle at the converter bus
X, X', X''	leakage, transient, and subtransient reactances
X_C	commutation reactance

X_T	converter transformer reactance
X_{ls}, R_s	stator leakage reactance and resistance
$\triangle\mathbf{x}$, $\triangle\mathbf{u}$	perturbations of the system state variables and inputs around the given operating point
T'_{do}, T''_{do}	field winding transient and subtransient time constants
CC	constant current
CV	constant voltage
GSC	global supplementary control
LSC	local supplementary control
MPC	model predictive control
WSCC	Western Systems Coordinating Council

Chapter 1

Introduction

1.1 Large-Scale Integration of HVDC Transmission in AC Power Systems

Power system stability is defined as the ability of the power system to remain in a state of equilibrium under normal conditions and regain a state of equilibrium after being subjected to disturbances [1]. Different forms of power system instabilities, e.g., rotor angle instability and voltage instability, have been comprehensively explored in the technical literature. Rotor angle stability requires the rotors of all interconnected synchronous machines to be in synchronism. Perturbing the system equilibrium leads to an acceleration or deceleration of the machines' rotors and may lead to loss of synchronism. Rotor angle stability phenomena are categorized as small-signal dynamic stability and transient stability. In this thesis the focus is on small-signal rotor angle stability.

Small-signal rotor angle stability is fundamental to the safe operation of the power system [1], and enables the power system to maintain synchronism under small disturbances. The disturbances are considered to be sufficiently small such that the linearized system model can be used for stability analyses. Small-signal instability is due to lack of sufficient damping of oscillations. Small-signal oscillations appears in the form of local modes, inter-area modes, control modes and torsional modes [1]. Local modes are associated with the swing of one or a group of generators against the rest of the power system. Inter-area modes are associated with the swing of a group of generators in one part of the power system against other aggregates of generators in other parts. The inter-area oscillations are often experienced over a large part of the power system and local oscillations usually appear in only a small part of the system [1].

One incident of the inter-area oscillation problem was the oscillations experienced

on Aug. 14, 2003, where Ontario and much of the northeastern U.S. were subjected to the largest blackout in North America's history [2]. More than 263 power plants tripped offline in Canada and the U.S., leaving 50 million people without power for up to nine hours. However, Quebec was not affected by the blackout, because its major interconnections are the high voltage direct current (HVDC) transmission lines.

The classical application of HVDC system is the transmission of bulk power over long distances due to the lower overall transmission cost and losses as compared with the AC transmission lines [3]. Furthermore, the amount of transmitted power on HVDC lines and the transmission distance are not limited by stability constraints. The constraints associated with stability problems or control strategies are removed by interconnecting systems via HVDC lines [3]. HVDC system provides some degree of buffering against cascading failures in the grid and compared to the conventional AC transmission system has a higher degree of controllability for the operation of power systems [3]. An HVDC link connected between two AC systems operates regardless of the voltage and frequency conditions of the two systems. Therefore, it provides an independent control for transmitting power between systems. The same applies for an HVDC link within one AC system. HVDC technology can resolve a large number of existing AC power system steady-state and dynamic instability issues and improve the security of the system. The integration of HVDC technology in an AC system can be achieved by

- connecting AC buses of a single AC grid through HVDC links,
- embedding an HVDC grid in an AC system, and
- DC segmentation.

In the first configuration, known as an embedded HVDC system in an AC grid, one or multiple point-to-point (PTP) HVDC links connect a set of AC system buses in a single AC grid. In the second configuration, known as the HVDC grid, several AC buses are interconnected through converter stations which share a common DC transmission system [3]. In the third configuration, the AC grid is decomposed into smaller AC segments connected through DC links (and potentially weak AC lines) and the main power corridors among the segments are the DC links.

1.1.1 Embedded HVDC System in an AC Grid

In this configuration, PTP HVDC links are used for the bulk transmission of electrical power in a single AC grid. Fig. 1.1 (a) shows a schematic diagram of embedded HVDC links in a single AC grid. The longest embedded HVDC link in the world is currently

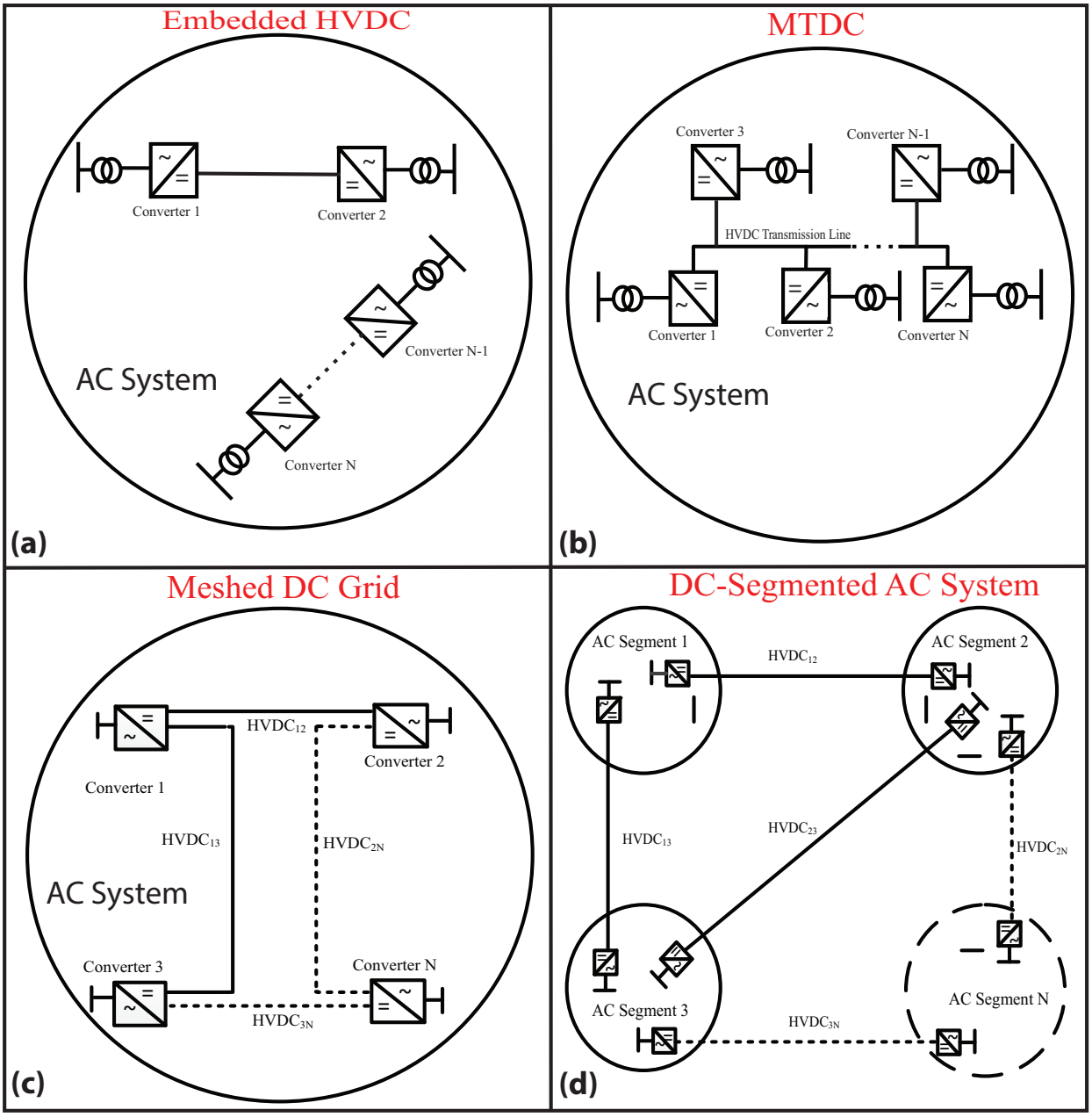

Figure 1.1: The integration of HVDC technology in an AC system: (a) Embedded HVDC system in an AC grid, (b) MTDC, (c) Meshed DC grid, and (d) DC segmentation.

the 2071 km, ±800 kV, 6400 MW link in the People's Republic of China [4]. The longest transmission link in the world, 2375 km, will be the Rio Madeira link in Brazil, which is scheduled for completion in 2013 [4].

1.1.2 HVDC Grid

Another approach for the integration of HVDC transmission in an AC grid is embedding an HVDC grid in the AC system. The meshed HVDC grid includes multiple DC converters which are interconnected by a meshed DC transmission network. In this configuration, if one HVDC line is lost, another line supports the partially isolated node [5]. This configuration should contain at least one loop and can be realized only based on self-commutated voltage-sourced converter (VSC) technology. Fig. 1.1 (c) shows a schematic diagram of a meshed HVDC grid. Multi-terminal HVDC (MTDC) configuration is a special type of the HVDC grid, where both line-commutated current-sourced converter (LCC) and VSC technologies can be utilized [3]. Fig. 1.1 (b) shows a schematic diagram of an MTDC grid.

The HVDC grid offers fast response time, reduces congestion, improves system dynamic stability and performance under disturbances, provides flexibility in power flow control and facilitates the integration of renewable energy sources [3, 6–9]. In the European power system, where massive renewable energy sources in offshore or remote locations are utilized, this configuration is a solution that will integrate substantial amount of renewable energy to the grid [10]. Besides, effective oscillation damping can be provided by the independent active and reactive power modulations and transmission bottlenecks can be addressed via the fast power flow controllability of the VSC-HVDC system, oscillation damping and dynamic voltage support. In comparison to a multiple point-to-point HVDC configuration, the MTDC configuration has less number of converter stations and lower transmission loss. Currently, for MTDC applications, only LCC-based HVDC has been used. Most notable lines are the one from Hydro-Quebec to New England and the one between Sardinia, Corsica and Italy (SACOI). In comparison to an LCC-based MTDC system, where the function of each converter station (rectifier or inverter) is often fixed, the VSC technology of the DC grid provides bi-directional power transfer by varying the current direction and facilitates the realization of DC grids of more than a few terminals [7].

1.1.3 AC Grid Segmentation

One approach to mitigate and/or geographically localize oscillatory modes of an AC system to enhance the system stability is to partition the AC system into segments by back-to-back (BTB) and/or PTP HVDC links [11, 12], based on VSC and/or LCC technologies as shown in Fig. 1.1 (d). The segments can also have AC lines connections; however, the AC lines should not constitute major power corridors.

Segmentation of the AC grid can be achieved through the conversion of AC links to BTB or PTP DC links [12, 13], and/or the installation of new HVDC links. The size of each AC segment is based on a trade-off between the converter cost, potential gain in reliability and power transfer capability enhancement, geographical/political boundaries, and the system operational characteristics and requirements [14]. The boundaries of the AC segments are determined according to

- congested areas that need more transfer capability,
- locations where longer HVDC lines can be formed from existing AC lines,
- locations that require the least back-to-back MVA, and
- locations where HVDC links can replace stability-limited AC links [15].

Some of the key benefits of the DC segmentation are [11, 12, 15]:

- minimizing cascading outages and widespread blackouts,
- confining system collapse to the faulted segment,
- increasing power transfer capability among segments,
- providing significant local oversight on the grid,
- potentially easier grid expansion planning and investment decisions,
- state estimators performance enhancement,
- feasibility of intelligent/self-healing grid planning,
- more effective wide area measurement system (WAMS)-based applications,
- controllability of the inter-area power flows,
- reducing operational complexity and uncertainty, and
- increasing system resiliency to natural and man-made disturbances.

The work reported in [11] is the first systematic assessment of the DC segmentation concept and its potential advantages. In [11], the reliability and transfer capability improvement of the Eastern Interconnection (EI) of North America with segmentation is examined by comparing the dynamic performance of the system before and after segmentation. In [12], the response of an AC test system with and without segmentation to two

typical disturbances, generation loss and line-trip, are studied. The study shows that segmentation can prevent cascading outages and reduces fault impacts on neighboring segments. Decomposing the AC grid into smaller segments does not eliminate all the stability problems associated with large AC grids. However, conceptually, DC segmentation of the interconnected AC system results in more localized and more manageable problems [15].

1.1.4 Mitigation of Dynamic Oscillatory Modes of an AC-DC System

Two general methods of improving power system small-signal stability are the installation of new devices and improving the control of existing devices. In particular, the following methods have been investigated [16]:

- installing new infrastructure, such as adding new transmission lines to the power system or installing new generation capacity,
- installing flexible AC transmission system (FACTS) controllers, e.g. unified power flow controllers (UPFCs) [17–19], thyristor controlled phase shifting transformers [17], thyristor controlled series capacitors (TCSCs) [17,20,21], static VAR compensators (SVCs) [22,23], static phase shifters (SPSs) [24] and static synchronous compensators (STATCOMs) [25],
- modifying the control scheme by adopting power system stabilizers (PSSs) [26–31], and
- modifying the control scheme by adopting HVDC modulation and set-point adjustment [29,32].

Improving the HVDC control scheme, i.e., adopting HVDC modulation techniques and adjusting the set-point of the HVDC links, is an attractive alternative to additional infrastructure installation. Reported studies have shown that the stability of power systems can be improved by the judicious control of the existing HVDC connections [33]. In this thesis, we focus on the HVDC power modulation to mitigate oscillatory dynamics and we refer to this controller as the supplementary controller (SC). Furthermore, a set-point tuning method is proposed to increase the power system stability margin (a metric for the stability of the closed loop system). A higher stability margin corresponds to a more stable system with smaller amplitude oscillatory transients.

1.2 Statement of the Problem and Thesis Objectives

Although there have been studies on the conceptual segmentation of the AC grid with HVDC links, small-signal stability enhancement in such a configuration has not been investigated. The objective of this thesis is to enhance the small-signal stability of a DC-segmented AC power system. Four control schemes have been proposed to achieve the main objective of this thesis. Control schemes 1-4 improve the system stability by damping the oscillations within the segment, minimizing the propagation of the oscillations to the neighboring segments, distributing the oscillations among the segments and changing the set-points of the HVDC control system, respectively. Depending on the system characteristics, one or more of the proposed control schemes may be effective for the mitigation of system oscillations. Improving the system stability by modifying the control scheme is appealing since it is cost effective in comparison to the installation of additional equipment, and can be implemented by modifying the existing control schemes instead of installing physical power apparatus.

To achieve the main objective of this thesis, this research work focuses on:

- Developing a small-signal dynamic model based on computer-assisted linearization of AC-DC systems for control design, time-domain simulation and systematic performance evaluation of the control scheme (The developed model can be used for various control designs and its application is not limited to the controllers designed in this thesis).

- Developing a HVDC local supplementary control (LSC) scheme, using the small-signal dynamic model of the system, to damp inter-area oscillations in the AC-DC system.

- Developing a HVDC global supplementary control (GSC) scheme, using the small-signal dynamic model of the system, to improve the system stability by distributing the oscillations among the segments.

- Developing a GSC scheme, using the small-signal dynamic model of the system, to improve the system stability by minimizing the propagation of the oscillations to the other segments.

- Developing an operating point tuning scheme to adjust the HVDC control set-points, to enhance the small-signal stability of an AC-DC system.

Each of these milestones has been achieved based on HVDC supplementary control or modification of the operational condition of the HVDC control system.

1.3 Methodology

In order to achieve the aforementioned thesis objective, the following methodology is employed:

- Systematically construct the nonlinear differential-algebraic model of an AC-DC system,
- Automatically extract a linearized state space model of the nonlinear system (using the developed MATLAB/Simulink-based platform),
- Design linear control schemes for the linearized system model (using the developed MATLAB/Simulink-based platform) and design a control scheme based on the sensitivity of the system stability margin with respect to the parameter space, and
- Perform time-domain simulation: MATLAB/Simulink environment is used to evaluate the agreement between the corresponding dynamic responses of the automatically generated linearized model and the nonlinear model to small disturbances and validate the accuracy of the linearized model. The performance of the proposed control schemes and the dynamic behaviour of the system, including the proposed controllers, under various faults and disturbances are investigated through time-domain simulations in the developed MATLAB/Simulink-based platform.

1.4 Thesis Layout

The rest of this thesis is organized as follows:

- chapter 2 introduces a modeling approach and integration procedure for developing AC-DC power system models in the MATLAB/Simulink environment and demonstrates the effectiveness of the automatic linearization provided by Simulink. In the following chapters, the developed AC-DC model will be used to design the control schemes to damp oscillations.
- chapter 3 introduces, formulates and evaluates an approach for damping the oscillations of power systems based on supplementary current control of an LCC HVDC link within a segment. The proposed control is based on the model predictive control (MPC) method. This chapter presents the MPC design procedure and evaluates the performance of a discrete-time MPC-based HVDC supplementary controller for mitigating oscillatory modes of two study systems. This chapter

also compares the damping effect of the designed MPC-based controller with that of a linear quadratic Gaussian (LQG) controller for the same test systems.

- chapter 4 introduces two control schemes based on the supplementary control of inter-segment HVDC links, to (i) confine the oscillatory dynamics initiated in a segment within that segment and minimize their propagation to other segments, or (ii) distribute the oscillatory modes among the segments. An LQG control method is adopted to design the HVDC supplementary controls. Each HVDC supplementary control provides simultaneous modulation of the current order and voltage reference of the corresponding rectifier and inverter stations. Performances of both GSC schemes are evaluated and compared. This chapter also introduces a sensitivity measure to evaluate the performance of each design to the variations in the system parameters and operating point.

- chapter 5 presents a control scheme based on the adjustment of the set-point value of the HVDC lines to improve the stability margin and control Hopf bifurcations (at a Hopf point, a complex pair of eigenvalues of the linearized system crosses the imaginary axis) caused by gradual variation of the parameters such as loads. In this chapter, local bifurcation theory and computation of the sensitivity of the stability margin and the real part of the critical eigenvalues with respect to the parameter space are discussed. The optimization problem together with a brief description of modeling the system for this type of optimization are also presented. The proposed control scheme is evaluated on two test systems for several Hopf bifurcations caused by a variety of events such as load and line impedance variations.

- chapter 6 summarizes the contributions of the thesis, presents its conclusions, and recommends future research directions.

Chapter 2

Small-Signal Dynamic Model Development Based on Computer-Assisted Linearization

2.1 Introduction

Systematic design of a controller, e.g., a linear HVDC supplementary controller, requires a differential-algebraic model of the system, which includes both DC and AC components. Linearization of the models is one of the requirements for the control design process, since most of the controllers applied to power systems are linear controllers. The characteristics of the nonlinear system to be controlled vary due to topological changes, load/generation variations, etc. These changes must be taken into account in the linearized model. Therefore, to achieve the desired performance in the system, the linearization process often has to be repeated each time the system is subjected to a change. Thus, automation of the linearization process is highly desirable and makes the controller design process faster and more accurate.

The design of a linear controller requires (i) a mathematical description of the nonlinear AC-DC system model, (ii) steady-state solution of the system to obtain the operating point about which the linearized model is developed, and (iii) linearization of the nonlinear model. The automation of steps (ii) and (iii) is essential for the practical design of controllers, given that the operating point and parameters of the system vary and, with each change, the linearization process has to be repeated.

There exists a host of software packages, e.g., PSS/E, DIGSILENT, and PST, for the analysis of low-frequency dynamics and steady-state response of power systems. There

are three main limitations in using the existing software tools to design controllers for AC-DC systems: (i) lack of provisions to provide a full nonlinear state-space model of the AC-DC system, (ii) inability to automatically generate a state-space linearized model, and (iii) limited component modeling capability. For example, two of the popular commercial packages for power system analysis, DIGSILENT and PSS/E, provide some limited information of the linearized model to the user, but do not provide the full linear model needed in controller design. The NEVA-Eigenvalue and Modal Analysis module of the PSS/E software only provide eigenvalues and eigenvectors, and DIGSILENT only provides the eigenvalues, eigenvectors, controllability, observability and participation factors for each state variable. Although these eigenvalue analyses are likely based on an internal linearized model, the full linearized state space model is not available to the user. Instead, only data extracted from that model is provided to the user, whereas for control design purposes, the full linearized state space model is required.

The Power System Toolbox (PST) consists of a set of coordinated MATLAB m-files that model the power system components for power flow and stability studies, provides a full linearized model of the AC-DC system [34] and does not have the above mentioned limitation. However, PST has a limited set of models (e.g., the dynamics of the HVDC controllers and the DC transmission line are not included in this software) and is not being actively developed. In addition, custom models cannot be automatically linearized in this software.

As an alternative to specialized power system software, MATLAB/Simulink [35] has been successfully used for time-domain simulation of AC-DC power systems and offers specific advantages when compared with standard power system analysis packages. For example, once a model is built in Simulink, one can obtain alternative representations of the system (e.g., state-space models or transfer functions), using the automated tools that are parts of the Simulink software [35]. Furthermore, the block structure of this software enables a controller designer to construct new device and controller models using Simulink's extensive library of standard control blocks and obtain the new linearized model automatically. Given its capabilities, this platform is a suitable environment for controller design.

The objective of this chapter is to present a nonlinear state-space model of an interconnected AC-DC power system and describe the approach to define the model in Simulink. Particular emphasis is placed on describing the approach to combine the differential and algebraic models of the DC and AC subsystems and to enable automatic linearization for control design. Furthermore, the accuracy of the automatic linearization provided by Simulink is demonstrated.

2.2 Low-Frequency Dynamic Model of the AC System

The balanced AC systems under consideration include the turbine-generator (T-G) units and their controls, AC transmission lines, and transformers. The detailed model of each of these components is given in [36], and a brief summary of each is provided below.

2.2.1 Turbine-Generator (T-G) Unit Model

The electromechanical system of each T-G unit is assumed to include a synchronous machine (SM) and a turbine system. The electrical system of each SM is represented by one field winding and one damper winding on the rotor d-axis and two damper windings on the rotor q-axis. The stator dynamics of each SM are neglected and it is assumed that the SM magnetic circuit is linear. The model of each machine rotor electrical system is expressed in a d-q reference frame which rotates at the corresponding rotor speed. The stator circuitry of the i^{th} SM is represented by the following algebraic equations [36]

$$R_{si}I_{di} + \frac{\omega_i}{\omega_s}\Psi_{qi} + V_{di} = 0, \tag{2.1}$$

$$R_{si}I_{qi} - \frac{\omega_i}{\omega_s}\Psi_{di} + V_{qi} = 0, \tag{2.2}$$

where

$$\Psi_{di} = -X_d^{''}I_{di} + \frac{(X_{di}^{''} - X_{lsi})}{(X_{di}^{'} - X_{lsi})}E_{qi}^{'} + \frac{(X_{di}^{'} - X_{di}^{''})}{(X_{di}^{'} - X_{lsi})}\Psi_{1di}, \tag{2.3}$$

$$\Psi_{qi} = -X_{qi}^{''}I_{qi} - \frac{(X_{qi}^{''} - X_{lsi})}{(X_{qi}^{'} - X_{lsi})}E_{di}^{'} + \frac{(X_{qi}^{'} - X_{qi}^{''})}{(X_{qi}^{'} - X_{lsi})}\Psi_{2qi}. \tag{2.4}$$

The dynamics of the rotor electrical system of the i^{th} SM in a dqo frame rotating at the rotor speed (zero sequence is neglected) are given by

$$T_{doi}^{'}\frac{dE_{qi}^{'}}{dt} = E_{fdi} - (X_{di} - X_{di}^{'})\Big(I_{di} - \frac{X_{di}^{'} - X_{di}^{''}}{(X_{di}^{'} - X_{lsi})^2}(\Psi_{1di} + (X_{di}^{'} - X_{lsi})I_{di} - E_{qi}^{'})\Big) - E_{qi}^{'}, \tag{2.5}$$

$$T_{doi}^{''}\frac{d\Psi_{1di}}{dt} = -\Psi_{1di} + E_{qi}^{'} - (X_{di}^{'} - X_{lsi})I_{di}, \tag{2.6}$$

$$T_{qoi}^{'}\frac{dE_{di}^{'}}{dt} = (X_{qi} - X_{qi}^{'})\Big(I_{qi} - \frac{X_{qi}^{'} - X_{qi}^{''}}{(X_{qi}^{'} - X_{lsi})^2}\big(\Psi_{2qi} + (X_{qi}^{'} - X_{lsi})I_{qi} + E_{di}^{'}\big)\Big) - E_{di}^{'}, \tag{2.7}$$

$$T''_{qoi}\frac{d\Psi_{2qi}}{dt} = -\Psi_{2qi} - E'_{di} - (X'_{qi} - X_{lsi})I_{qi}. \tag{2.8}$$

The mechanical system of the i^{th} T-G unit is represented by an equivalent rigid mass and its dynamics are given as [36]

$$\frac{d\delta_i}{dt} = \omega_i - \omega_s, \tag{2.9}$$

$$\frac{2H_i}{\omega_s}\frac{d\omega_i}{dt} = T_{mi} - D_i(\omega_i - \omega_s) - \frac{\omega_s}{\omega_i}\left(V_{di}I_{di} + V_{qi}I_{qi} + R_{si}(I_{di}^2 + I_{qi}^2)\right). \tag{2.10}$$

2.2.2 Excitation System Model

It is assumed that each SM is equipped with an IEEE Type-I exciter system [36] and dynamically described by

$$T_{Ei}\frac{dE_{fdi}}{dt} = -\left(K_{Ei} + S_E\left(E_{fdi}\right)\right)E_{fdi} + V_{Ri}, \tag{2.11}$$

$$T_{Fi}\frac{dR_{fi}}{dt} = -R_{fi} + \frac{K_{Fi}}{T_{Fi}}E_{fdi}, \tag{2.12}$$

$$T_{Ai}\frac{dV_{Ri}}{dt} = -V_{Ri} + K_{Ai}R_{fi} - \frac{K_{Ai}K_{Fi}}{T_{Fi}}E_{fdi} + K_{Ai}(V_{refi} - |\bar{V}_{ti}|). \tag{2.13}$$

If V_{Ri} reaches its limit, it is set to that limit in (2.11).

2.2.3 Governor System Model

Each T-G unit is equipped with a TGOV1 type governor [36] which is dynamically described by

$$\frac{dT_{svi}}{dt} = 1/T_{1i}\Big(-T_{svi}\frac{\omega_i}{\omega_s} + \frac{P_{refi}}{R_i} - \frac{1}{R_i}(\omega_i - \omega_s)\Big), \tag{2.14}$$

$$\frac{dT_{mi}}{dt} = 1/T_{3i}\Big(-T_{mi} + T_{svi}\Big). \tag{2.15}$$

2.2.4 AC Network Model

The AC network is composed of AC transmission lines and transformers. Since the objective of this study is to investigate low-frequency dynamics, e.g., 0.1 to 2 Hz, the AC transmission network is represented by the positive sequence algebraic equations associated with the network nodal equations

$$\bar{\mathbf{I}} = \mathbf{Y}_N \bar{\mathbf{V}}, \tag{2.16}$$

where $\bar{\mathbf{I}}$ and $\bar{\mathbf{V}}$ are expressed in the system global DQ reference frame at the high voltage bus of T-G unit 1 [36] with components $\bar{I}_i = I_{Di} + jI_{Qi}$ and $\bar{V}_i = V_{Di} + jV_{Qi}$, respectively. Power system loads are modeled as constant impedances and included in the $\mathbf{Y}_N$ matrix.

2.2.5 Multi-Machine System Model

The dynamic model of each T-G unit, (2.1)-(2.2) and (2.5)-(2.15) is transformed to the system global DQ reference frame and arranged in a state-space form. These equations constitute the following set of nonlinear differential-algebraic equations (DAEs)

$$\dot{\mathbf{x}}_{ac} = \mathbf{f}_{ac}(\mathbf{x}_{ac}, \mathbf{u}_{ac}, \mathbf{y}_{ac}), \tag{2.17}$$

$$\mathbf{g}_{ac}(\mathbf{x}_{ac}, \mathbf{y}_{ac}) = \mathbf{0}, \tag{2.18}$$

where

$$\mathbf{x}_{ac} = \begin{bmatrix} \mathbf{x}_{1_{ac}}^T & \mathbf{x}_{2_{ac}}^T & \dots & \mathbf{x}_{n_{TGac}}^T \end{bmatrix}^T, \tag{2.19}$$

$$\mathbf{x}_{i_{ac}} = [E_{qi}^{'}\, E_{di}^{'}\, \Psi_{1di}\, \Psi_{2qi}\, \delta_i\, \omega_i\, E_{fdi}\, R_{fi}\, V_{Ri}\, T_{svi}\, T_{mi}]^T, \tag{2.20}$$

$$\mathbf{u}_{ac} = \begin{bmatrix} \mathbf{u}_{1_{ac}}^T & \mathbf{u}_{2_{ac}}^T & \dots & \mathbf{u}_{n_{TGac}}^T \end{bmatrix}^T, \tag{2.21}$$

$$\mathbf{u}_{i_{ac}} = \begin{bmatrix} P_{refi} & \omega_s & V_{refi} \end{bmatrix}^T, \tag{2.22}$$

$$\mathbf{y}_{ac} = \begin{bmatrix} \mathbf{y}_{1_{ac}}^T & \mathbf{y}_{2_{ac}}^T & \dots & \mathbf{y}_{n_{TGac}}^T \end{bmatrix}^T, \tag{2.23}$$

$$\mathbf{y}_{i_{ac}} = \begin{bmatrix} V_{Di} & V_{Qi} & V_{di} & V_{qi} & I_{Di} & I_{Qi} & I_{di} & I_{qi} \end{bmatrix}^T, \tag{2.24}$$

$$\mathbf{f}_{ac} = \begin{bmatrix} \mathbf{f}_{1_{ac}}^T & \mathbf{f}_{2_{ac}}^T & \dots & \mathbf{f}_{n_{TGac}}^T \end{bmatrix}^T, \tag{2.25}$$

$$\mathbf{f}_{i_{ac}} = \begin{bmatrix} 1/T'_{doi}\Big(E_{fdi} - (X_{di} - X'_{di})\Big(I_{di} - \frac{X'_{di}-X''_{di}}{(X'_{di}-X_{lsi})^2}(\Psi_{1di} + (X'_{di} - X_{lsi})I_{di} - E'_{qi})\Big) - E'_{qi}\Big) \\ 1/T'_{qoi}\Big((X_{qi} - X'_{qi})\Big(I_{qi} - \frac{X'_{qi}-X''_{qi}}{(X'_{qi}-X_{lsi})^2}(\Psi_{2qi} + (X'_{qi} - X_{lsi})I_{qi} + E'_{di})\Big) - E'_{di}\Big) \\ 1/T''_{doi}\Big(- \Psi_{1di} + E'_{qi} - (X'_{di} - X_{lsi})I_{di}\Big) \\ 1/T''_{qoi}\Big(- \Psi_{2qi} - E'_{di} - (X'_{qi} - X_{lsi})I_{qi}\Big) \\ \omega_i - \omega_s \\ \Big(\frac{\omega_s}{2H_i}\Big)\Big(T_{mi} - D_i(\omega_i - \omega_s) - \frac{\omega_s}{\omega_i}\left(V_{di}I_{di} + V_{qi}I_{qi} + R_{si}(I_{di}^2 + I_{qi}^2)\right)\Big) \\ 1/T_{Ei}\Big(- (K_{Ei} + S_E\left(E_{fdi}\right))E_{fdi} + V_{Ri}\Big) \\ 1/T_{Fi}\Big(- R_{fi} + \frac{K_{Fi}}{T_{Fi}}E_{fdi}\Big) \\ 1/T_{Ai}\Big(- V_{Ri} + K_{Ai}R_{fi} - \frac{K_{Ai}K_{Fi}}{T_{Fi}}E_{fdi} + K_{Ai}(V_{refi} - |\bar{V}_{ti}|)\Big) \\ 1/T_{1i}\Big(- T_{svi}\frac{\omega_i}{\omega_s} + \frac{P_{refi}}{R_i} - \frac{1}{R_i}(\omega_i - \omega_s)\Big) \\ 1/T_{3i}\Big(- T_{mi} + T_{svi}\Big). \end{bmatrix} \tag{2.26}$$

In (2.18), $\mathbf{g}_{ac}(\mathbf{x}_{ac}, \mathbf{y}_{ac}) = \mathbf{0}$ represents the algebraic equations of the stator circuitry of the SMs ($\mathbf{g}_{SM_{ac}}$), (2.28)-(2.29), network nodal equations ($\mathbf{g}_{NE_{ac}}$), (2.16), and coordinate transformation equations ($\mathbf{g}_{CO_{ac}}$), (2.30)-(2.33).

$$\mathbf{g}_{ac} = \begin{bmatrix} \mathbf{g}_{SM_{ac}}^T & \mathbf{g}_{NE_{ac}}^T & \mathbf{g}_{CO_{ac}}^T \end{bmatrix}^T, \tag{2.27}$$

$$\mathbf{g}_{SM_{ac}} = \begin{bmatrix} \mathbf{g}_{1_{ac}}^T & \mathbf{g}_{2_{ac}}^T & \cdots & \mathbf{g}_{n_{TG}ac}^T \end{bmatrix}^T, \tag{2.28}$$

$$\mathbf{g}_{i_{ac}} = \begin{bmatrix} R_{si}I_{di} + \frac{\omega_i}{\omega_s}\Psi_{qi} + V_{di} \\ R_{si}I_{qi} - \frac{\omega_i}{\omega_s}\Psi_{di} + V_{qi} \end{bmatrix}. \tag{2.29}$$

Coordinate transformation algebraic equations $g_{CO_{ac}}$ include (2.30)-(2.33) for all the generator buses.

$$V_{Di} - V_{di}\sin\delta_i - V_{qi}\cos\delta_i = 0, \tag{2.30}$$

$$V_{Qi} - V_{qi}\sin\delta_i + V_{di}\cos\delta_i = 0, \tag{2.31}$$

$$I_{di} - I_{Di}\sin\delta_i + I_{Qi}\cos\delta_i = 0, \tag{2.32}$$

$$I_{qi} - I_{Qi}\sin\delta_i - I_{Di}\cos\delta_i = 0. \tag{2.33}$$

The complete differential-algebraic model of the multi-machine AC system including the T-G units, coordinate transformation and AC network algebraic equations (2.17)-(2.18) are combined based on the block diagram of Fig. 2.1.

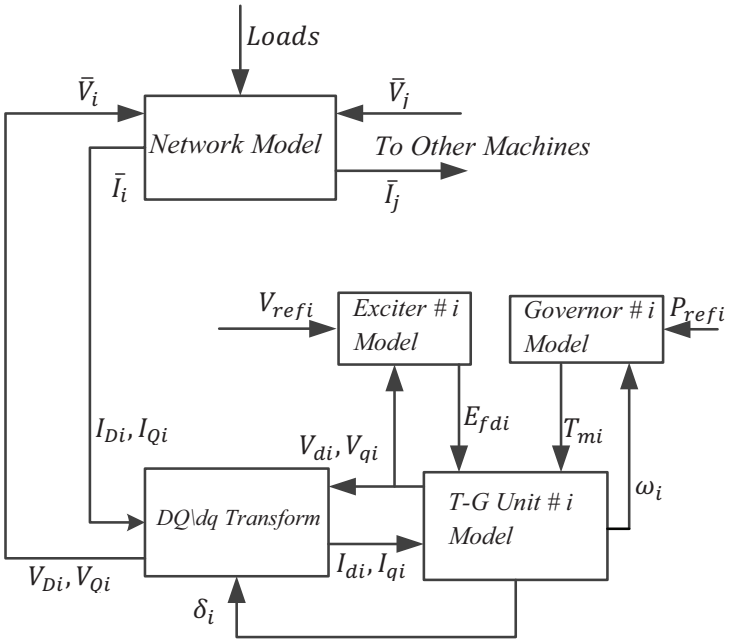

Figure 2.1: Block diagram of the AC system model

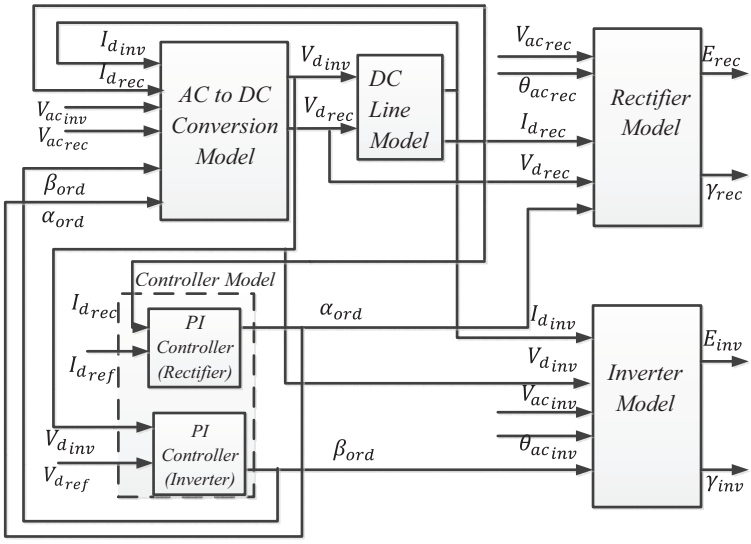

Figure 2.2: Block diagram of the DC system model

2.3 Low-Frequency Model of the DC System

The model of a DC system, to be integrated with the AC network model, includes models of four components, i.e., the HVDC controller, DC line, AC to DC conversion block and converter stations, Fig. 2.2. The models of these components are described in the following sections.

2.3.1 AC to DC Conversion Model

This block relates the corresponding AC and DC quantities based on the steady-state voltage-current relationship of the HVDC rectifier (rec) and inverter (inv) buses, i.e.,

$$V_{d_{reci}} = \frac{3\sqrt{2}}{\pi} n V_{ac_{reci}} \cos\alpha_{ord_i} - \frac{3X_{c_i}}{\pi} I_{d_{reci}}, \tag{2.34}$$

$$V_{d_{invi}} = \frac{3\sqrt{2}}{\pi} n V_{ac_{invi}} \cos\beta_{ord_i} + \frac{3X_{c_i}}{\pi} I_{d_{invi}}. \tag{2.35}$$

2.3.2 DC System Controller Models

The HVDC control system consists of the HVDC main and supplementary controllers [1]. Supplementary controllers are used to enhance the AC system dynamic performance. In this thesis, the supplementary controllers will be used to improve the damping of AC system oscillations and will be further explained in chapter 3.

In the HVDC main controller, the voltage and current regulation responsibilities are assigned to separate stations. Under normal operation, the rectifier station controls the corresponding DC side current (constant current mode (CC)) and the inverter station regulates the corresponding DC side voltage (constant voltage mode (CV)), e.g., using proportional-integral (PI) controllers. The rectifier regulates the current by adjusting the valve firing angle, α_{ord}, and the inverter regulates the voltage by adjusting the inverter firing angle, β_{ord}.

The block diagram of the HVDC control system is shown in Fig. 2.3. In Fig. 2.3, the CC and CV modes of the main HVDC controller and also HVDC supplementary controllers are depicted. The supplementary controllers modulate the current order and voltage reference and their outputs are added to the input of the main HVDC controllers.

2.3.3 DC Transmission Line Model

The DC line is represented by a T-equivalent shown in Fig. 2.4, and dynamically modeled as

$$\frac{dI_{d_{reci}}}{dt} = \frac{1}{L_{dc_i}}(V_{d_{reci}} - V_{ci} - R_{dc_i} I_{d_{reci}}), \tag{2.36}$$

$$\frac{dI_{d_{invi}}}{dt} = \frac{1}{L_{dc_i}}(-V_{d_{invi}} + V_{ci} - R_{dc_i} I_{d_{invi}}), \tag{2.37}$$

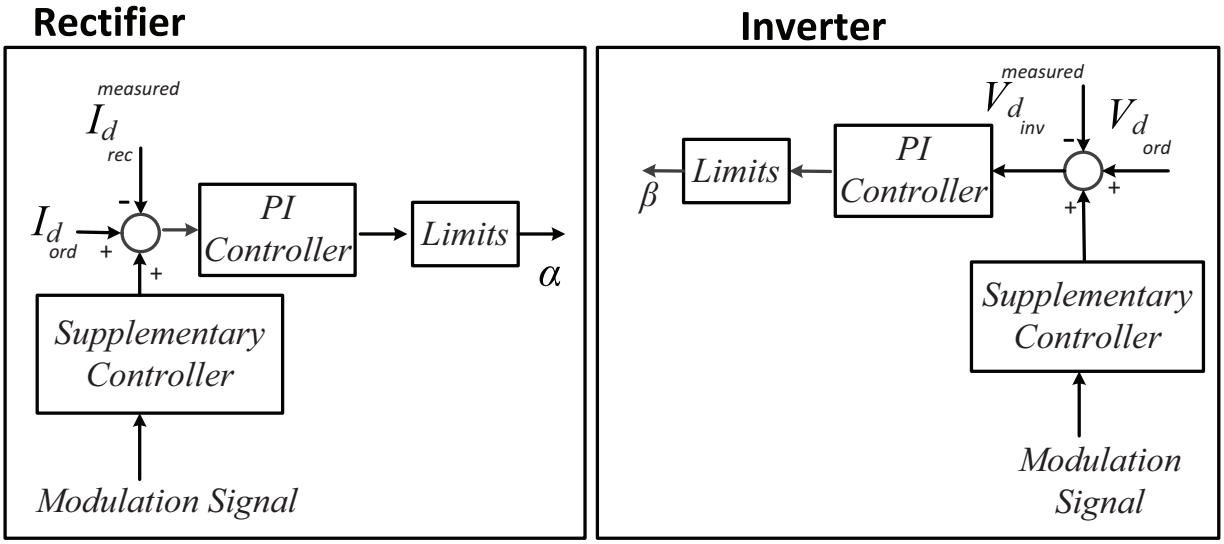

Figure 2.3: HVDC control system

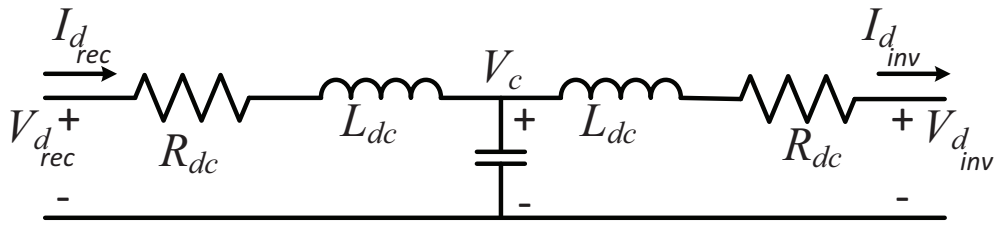

Figure 2.4: DC transmission line model

$$\frac{dV_{ci}}{dt} = \frac{1}{C_{dc_i}}(I_{d_{reci}} - I_{d_{invi}}). \tag{2.38}$$

2.3.4 Converter Model

The injection modeling approach [37] is used to represent each converter station. Each converter station is represented by a dynamic equivalent generator behind the reactance of the corresponding converter transformer, Fig. 2.5. The voltage and angle at the equivalent generator buses are adjusted to generate the desired active and reactive power flows as

$$P_{convi} = \frac{E_{convi} V_{ac_{convi}} \sin(\gamma_{convi} - \theta_{ac_{convi}})}{X_{T_i}}, \tag{2.39}$$

$$Q_{convi} = \frac{E_{convi}^2 - E_{convi} V_{ac_{convi}} \cos(\gamma_{convi} - \theta_{ac_{convi}})}{X_{T_i}}. \tag{2.40}$$

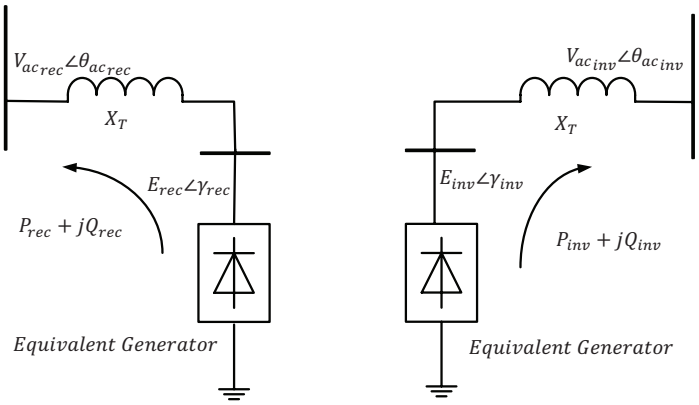

Figure 2.5: Injection model for HVDC converter stations

Therefore, the voltage and angle at the equivalent generator buses are

$$E_{convi} = \sqrt{a_{convi}^2 + b_{convi}^2}, \tag{2.41}$$

$$\gamma_{convi} = \theta_{ac_{convi}} + \tan^{-1}\left(\frac{a_{convi}}{b_{convi}}\right), \tag{2.42}$$

where

$$a_{convi} = \frac{X_T P_{convi}}{V_{ac_{convi}}}, \tag{2.43}$$

$$b_{convi} = \frac{1}{2}\left(V_{ac_{convi}} + \sqrt{V_{ac_{convi}}^2 - 4\left(\frac{X_{T_i}^2 P_{convi}^2}{V_{ac_{convi}}^2} - X_{T_i} Q_{convi}\right)}\right), \tag{2.44}$$

$$P_{reci} = -V_{d_{reci}} I_{d_{reci}},\ Q_{reci} = P_{reci}\tan\varphi_{\text{reci}}, \tag{2.45}$$

$$\varphi_{reci} = \cos^{-1}\left(\cos\alpha_{ord_i} - \frac{X_{c_i} I_{d_{reci}}}{\sqrt{2} n V_{ac_{reci}}}\right), \tag{2.46}$$

$$P_{invi} = V_{d_{invi}} I_{d_{invi}},\ Q_{invi} = P_{invi}\tan\varphi_{\text{invi}}, \tag{2.47}$$

$$\varphi_{invi} = \cos^{-1}\left(\cos\beta_{ord_i} + \frac{X_{c_i} I_{d_{invi}}}{\sqrt{2} n V_{ac_{invi}}}\right). \tag{2.48}$$

2.3.5 Overall DC System Model

The HVDC link equations are arranged in a state-space form and constitute a set of nonlinear differential and output equations which represent the HVDC system block as

given by

$$\dot{\mathbf{x}}_{dc} = \mathbf{f}_{dc}(\mathbf{x}_{dc}, \mathbf{u}_b), \tag{2.49}$$

$$\mathbf{y}_b = \mathbf{h}_{dc}(\mathbf{x}_{dc}, \mathbf{u}_b) \tag{2.50}$$

where

$$\mathbf{x}_{dc} = \begin{bmatrix} \mathbf{x}_{1_{dc}}^T & \mathbf{x}_{2_{dc}}^T & \dots & \mathbf{x}_{n_{dcdc}}^T \end{bmatrix}^T, \tag{2.51}$$

$$\mathbf{x}_{i_{dc}} = \begin{bmatrix} V_{ci} & I_{d_{reci}} & I_{d_{invi}} & I_{coni} & V_{coni} \end{bmatrix}^T, \tag{2.52}$$

$$\mathbf{u}_b = \begin{bmatrix} \mathbf{u}_{b1}^T & \mathbf{u}_{b2}^T \dots & \mathbf{u}_{bn_{dc}}^T \end{bmatrix}^T, \tag{2.53}$$

$$\mathbf{u}_{bi} = \begin{bmatrix} \theta_{ac_{reci}} & \theta_{ac_{invi}} & V_{ac_{reci}} & V_{ac_{invi}} & V_{d_{refi}} & I_{d_{refi}} \end{bmatrix}^T, \tag{2.54}$$

$$\mathbf{y}_b = \begin{bmatrix} \mathbf{y}_{b1}^T & \mathbf{y}_{b2}^T & \dots & \mathbf{y}_{bn_{dc}}^T \end{bmatrix}^T, \tag{2.55}$$

$$\mathbf{y}_{bi} = \begin{bmatrix} \gamma_{reci} & \gamma_{invi} & E_{reci} & E_{invi} \end{bmatrix}^T. \tag{2.56}$$

I_{con} and V_{con} are the states for the PI controllers used to regulate the current and voltage. The DAEs of the DC system are

$$\dot{\mathbf{x}}_{dc} = \mathbf{f}_{dc}(\mathbf{x}_{dc}, \mathbf{u}_{dc}, \mathbf{y}_{dc}), \tag{2.57}$$

$$\mathbf{g}_{dc}(\mathbf{x}_{dc}, \mathbf{y}_{dc}) = \mathbf{0}, \tag{2.58}$$

where

$$\mathbf{u}_{dc} = \begin{bmatrix} \mathbf{u}_{1_{dc}}^T & \mathbf{u}_{2_{dc}}^T & \dots & \mathbf{u}_{n_{dcdc}}^T \end{bmatrix}^T, \tag{2.59}$$

$$\mathbf{u}_{i_{dc}} = \begin{bmatrix} V_{d_{refi}} & I_{d_{refi}} \end{bmatrix}^T, \tag{2.60}$$

$$\mathbf{y}_{dc} = \begin{bmatrix} \mathbf{y}_{1_{dc}}^T & \mathbf{y}_{2_{dc}}^T & \dots & \mathbf{y}_{n_{dcdc}}^T \end{bmatrix}^T, \tag{2.61}$$

$$\mathbf{y}_{i_{dc}} = [V_{di_{inv}}\, V_{di_{rec}}\, \alpha_{ord_i}\, \beta_{ord_i}\, \gamma_{reci}\, \gamma_{invi}\, E_{reci}\, E_{invi}\, P_{invi}\, P_{reci}\, Q_{invi}\, Q_{reci}]^T, \tag{2.62}$$

$$f_{dc} = \begin{bmatrix} f_{1_{dc}}^T & f_{2_{dc}}^T & \dots & f_{n_{dcdc}}^T \end{bmatrix}^T, \tag{2.63}$$

$$\mathbf{f}_{dc_i} = \begin{bmatrix} \frac{1}{C_{dc_i}}(I_{d_{reci}} - I_{d_{invi}}) \\ \frac{1}{L_{dc_i}}(V_{d_{reci}} - V_{ci} - R_{dc_i} I_{d_{reci}}) \\ \frac{1}{L_{dc_i}}(-V_{d_{invi}} + V_{ci} - R_{dc_i} I_{d_{invi}}) \\ K_{I_{Icon}}(I_{d_{reci}} - I_{d_{refi}}) \\ K_{I_{Vcon}}(V_{d_{invi}} - V_{d_{refi}}) \end{bmatrix}. \tag{2.64}$$

In (2.58), $\mathbf{g}_{dc}(\mathbf{x}_{dc}, \mathbf{y}_{dc}) = \mathbf{0}$ represents the algebraic equations of the AC to DC conversion block ($\mathbf{g}_{CV_{dc}}$), (2.66)-(2.67), network nodal equations ($\mathbf{g}_{NE_{dc}}$), and converter model equations ($\mathbf{g}_{CO_{dc}}$). Converter model equations, $\mathbf{g}_{CO_{dc}}$, include (2.39)-(2.40), (2.45),(2.47) for all the converter stations.

$$\mathbf{g}_{dc} = \begin{bmatrix} \mathbf{g}_{CV_{dc}}^T & \mathbf{g}_{NE_{dc}}^T & \mathbf{g}_{CO_{dc}}^T \end{bmatrix}^T, \tag{2.65}$$

$$\mathbf{g}_{CV_{dc}} = \begin{bmatrix} \mathbf{g}_{1_{dc}}^T & \mathbf{g}_{2_{dc}}^T & \cdots & \mathbf{g}_{n_{dcdc}}^T \end{bmatrix}^T, \tag{2.66}$$

$$\mathbf{g}_{i_{dc}} = \begin{bmatrix} -V_{d_{reci}} + \frac{3\sqrt{2}}{\pi} n V_{ac_{reci}} \cos\alpha_{ord_i} - \frac{3X_{c_i}}{\pi} I_{d_{reci}} \\ -V_{d_{invi}} + \frac{3\sqrt{2}}{\pi} n V_{ac_{invi}} \cos\beta_{ord_i} + \frac{3X_{c_i}}{\pi} I_{d_{invi}} \\ -\alpha_{ord_i} + K_{P_{Icon}}(I_{d_{reci}} - I_{d_{refi}}) + I_{coni} \\ -\beta_{ord_i} + K_{P_{Vcon}}(V_{d_{invi}} - V_{d_{refi}}) + V_{coni} \end{bmatrix}. \tag{2.67}$$

2.4 Overall Model of the Multi-Machine AC-DC System

The overall model of the multi-machine AC-DC system is constructed from (2.17)-(2.18) and (2.57)-(2.58) as a set of DAEs:

$$\begin{bmatrix} \dot{\mathbf{x}}_{ac} \\ \dot{\mathbf{x}}_{dc} \end{bmatrix} = \mathbf{f}(\mathbf{x}_{ac}, \mathbf{x}_{dc}, \mathbf{y}_{dc}, \mathbf{y}_{ac}, \mathbf{u}_{dc}, \mathbf{u}_{ac}), \tag{2.68}$$

$$\mathbf{0} = \begin{bmatrix} g_{SM_{ac}} \\ g_{CO_{ac}} \\ g_{CV_{dc}} \\ g_{CO_{dc}} \\ \bar{\mathbf{I}}_{inj} - \mathbf{Y}_{red} \bar{\mathbf{V}}_{inj} \end{bmatrix}, \tag{2.69}$$

where

$$\bar{\mathbf{V}}_{inj} = \begin{bmatrix} \bar{\mathbf{V}}_{gen} & E_{rec}\angle\gamma_{rec} & E_{inv}\angle\gamma_{inv} \end{bmatrix}^T. \tag{2.70}$$

To calculate $\mathbf{Y}_{red}$, the network admittance matrix $\mathbf{Y}_N$ is partitioned into four matrices as

$$\begin{matrix} n_{inj} \\ n_{pas} \end{matrix} \begin{pmatrix} \bar{\mathbf{I}}_{inj} \\ 0 \end{pmatrix} = \begin{matrix} \\ n_{inj} \\ n_{pas} \end{matrix} \overset{\begin{matrix} n_{inj} & n_{pas} \end{matrix}}{\begin{pmatrix} \mathbf{Y}_A & \mathbf{Y}_B \\ \mathbf{Y}_C & \mathbf{Y}_D \end{pmatrix}} \begin{pmatrix} \bar{\mathbf{V}}_{inj} \\ \bar{\mathbf{V}}_{pas} \end{pmatrix}, \tag{2.71}$$

where $\bar{\mathbf{V}}_{pas}$ is the vector of voltage phasor at the buses without current injection. Injection buses include the generator and HVDC buses. Since there are no current injections at the n_{pas} network buses, these buses can be eliminated from (2.71). Thus

$$\bar{\mathbf{I}}_{inj} = \left(\mathbf{Y}_A - \mathbf{Y}_B\mathbf{Y}_D^{-1}\mathbf{Y}_C\right)\bar{\mathbf{V}}_{inj} = \mathbf{Y}_{red}\bar{\mathbf{V}}_{inj}. \tag{2.72}$$

At a given operating point, linearization of the model and elimination of the algebraic variables results in the following linearized model of the AC-DC system:

$$\triangle\dot{\mathbf{x}} = \mathbf{A}\triangle\mathbf{x} + \mathbf{B}\triangle\mathbf{u}, \tag{2.73}$$

where $\mathbf{A}$ and $\mathbf{B}$ are block structured matrices, with n_{TG} blocks associated with the T-G units and n_{dc} blocks associated with the HVDC links.

2.5 Implementation of the AC-DC System Model in MATLAB/Simulink

This section describes an implementation of the AC-DC system model, equations (2.68)-(2.69), in the MATLAB/Simulink environment for time-domain simulation and automatic generation of the linearized system state-space model.

The general signal flow of the AC-DC system model, including a DC-link supplementary controller, is shown in Fig. 2.6. Details of the HVDC supplementary controller will be discussed in chapter 3. Each block is constructed in the Simulink package. A challenge in the implementation of the system model within the MATLAB/Simulink environment is handling algebraic loops. An algebraic loop is formed when a signal loop with only direct feedthrough blocks exists, i.e., the output of the block is directly controlled by the input and no state variable exists in the block [35]. To overcome this problem, the outputs of the Network Equations block can be supplied to other blocks through Delay

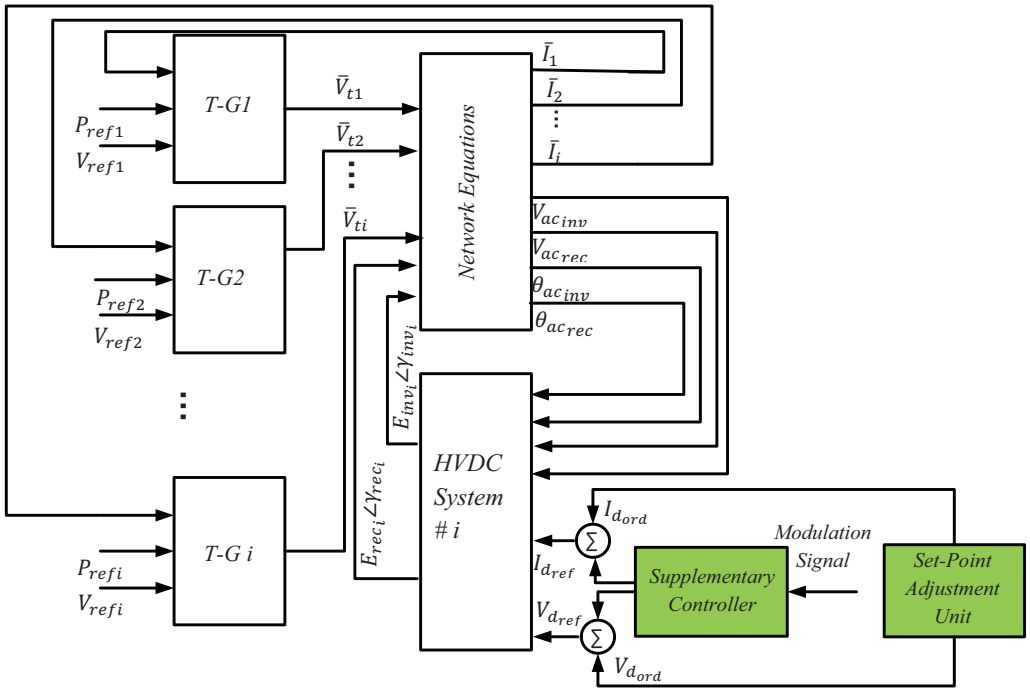

Figure 2.6: Signal flow of the AC-DC system with supplementary controllers and set-point adjustment unit

Blocks or first-order filters. By choosing a sufficiently small time-constant for the filter (e.g., 0.0005 s), the algebraic loop can be avoided without affecting the dynamics of interest.

Simulation of the AC-DC system dynamic behaviour requires the coordinated solution of the system's DAEs. At every integration step of the differential equations, the DC system, with respect to each converter station, is represented by a Thevenin equivalent [37] and the AC system is solved. Next, the terminal voltages of the generators and the equivalent generators are substituted in the network equations and the generator terminal currents are calculated. The voltage phasor of the converter buses are then used to calculate the voltage phasors of the equivalent generators at the converters' internal buses (buses connected to the equivalent generators). Each phasor voltage and the corresponding converters transformer reactance form the DC side Thevenin equivalent in the subsequent iteration.

One major advantage of implementing the AC-DC system model in the MATLAB/ Simulink environment is the capability to automatically extract the linear state-space model of Simulink-implemented systems given an operating point, system states and

inputs. The automated linearization process enables a control design that takes into account a wide range of parameters and system conditions. The "linmod" command of the MATLAB environment is used to extract the continuous linear state-space model of the system around a given operating point. To linearize the system model, the inputs and outputs of the system are specified in the Simulink block diagram and are used to compute the system linear model by linearizing each block individually. The default algorithm uses the Padé approximation to linearize the delay blocks and preprogrammed, analytic Jacobians for linearizing the remaining blocks. This approach results in a more accurate linearized model compared to those obtained from numerical perturbation of the inputs and states [35].

The operating point at which the system is linearized is determined by solving the DC and AC system power flow equations using the parameters specified in the Simulink model. A standard iterative solver of the AC and DC power flow equations can be used, e.g., as detailed in [1].

2.6 Validation of the MATLAB/Simulink-Based AC-DC Model

In this section, validation of the accuracy of the nonlinear and linearized AC-DC system models is investigated. The IEEE 14-bus 1-segment system is developed for this investigation. In the plots shown, per unit quantities are based on the corresponding machine ratings.

2.6.1 IEEE 14-Bus 1-Segment System

Fig. 2.7 shows a schematic diagram of the IEEE 14-bus system [38] which includes five T-G units and twenty AC transmission lines. Based on the system of Fig. 2.7, the IEEE 14-bus 1-segment system is constructed. Fig. 2.8 shows the schematic one-line diagram of the 1-segment system which is the same as Fig. 2.7, except an LCC HVDC link is connected between bus 2 (rectifier station) and bus 4 (inverter station). The HVDC link and control parameters are given in [37]. The governor parameters of the T-G units are given in Table 2.1.

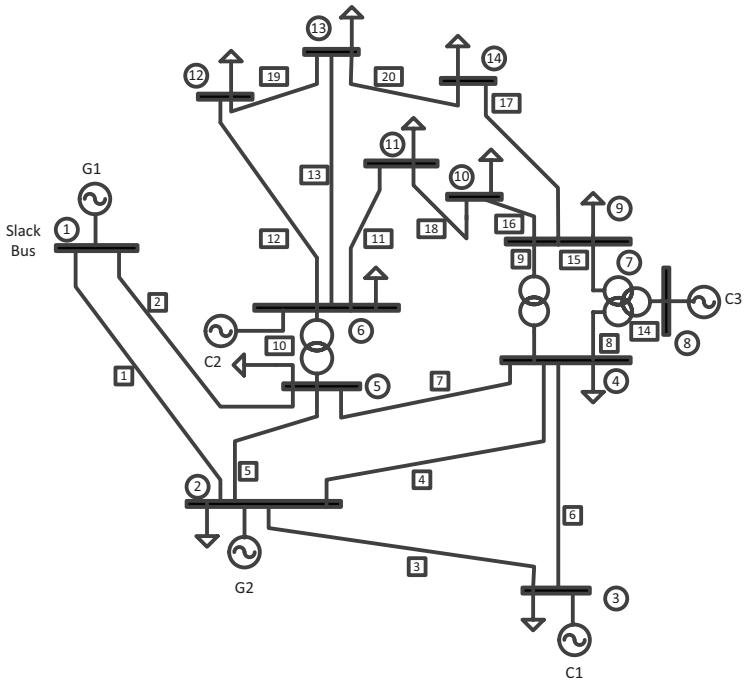

Figure 2.7: Schematic one-line diagram of the IEEE 14-bus system

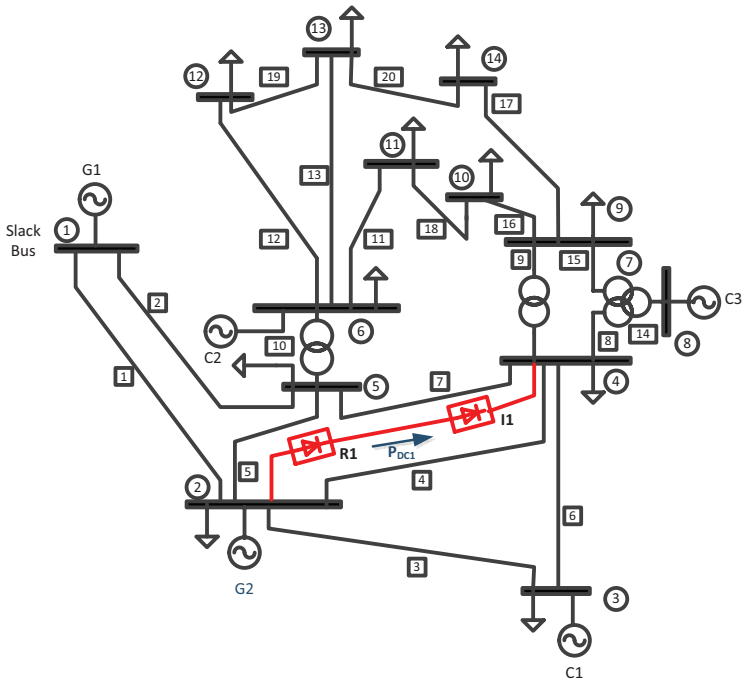

Figure 2.8: Schematic one-line diagram of the IEEE 14-bus 1-segment system

Table 2.1: Governor parameters of the T-G units

i	T_1^i	T_2^i	T_3^i	R^i
1	0.02	0	0.5	0.05
2	0.02	0	0.5	0.05
3	0.2	0	5.0	0.5
4	0.2	0	5.0	0.5
5	0.2	0	5.0	0.5

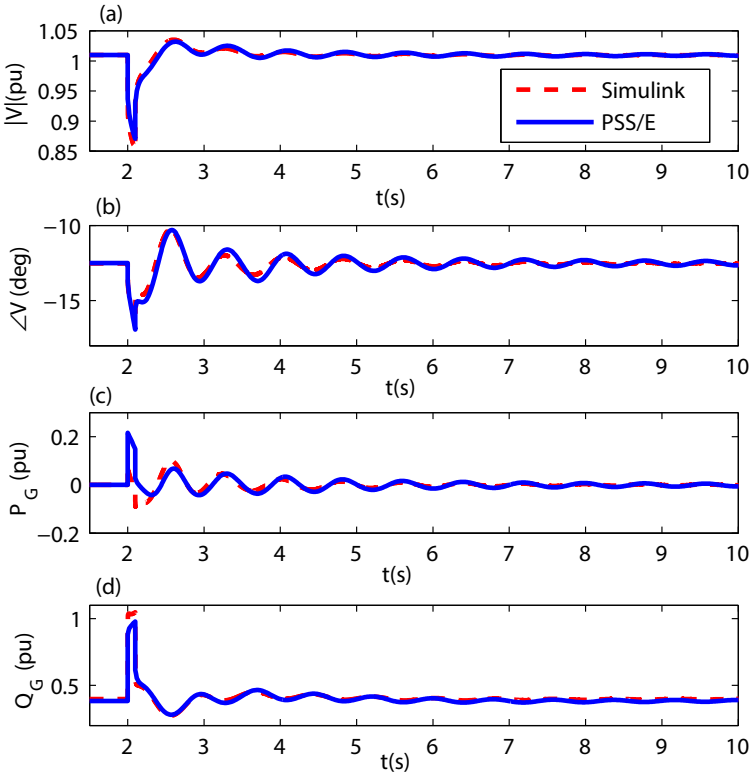

Figure 2.9: Voltage magnitude, angle, active and reactive power of machine C1 on bus 3 due to the L-L-L-G fault

2.6.2 Validation of the Nonlinear AC-DC Model

To demonstrate the accuracy of the time-domain simulation studies based on the developed MATLAB/Simulink nonlinear dynamic model, the dynamic behaviour of the IEEE 14-bus 1-segment test system, Fig. 2.8, is investigated and compared against simulation

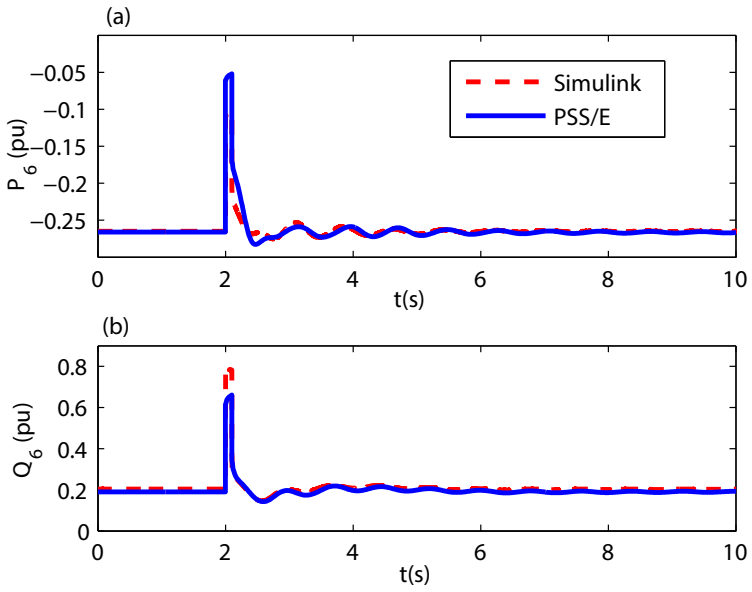

Figure 2.10: Active and reactive power flow changes of line 6 between buses 3 and 4 due to the L-L-L-G fault

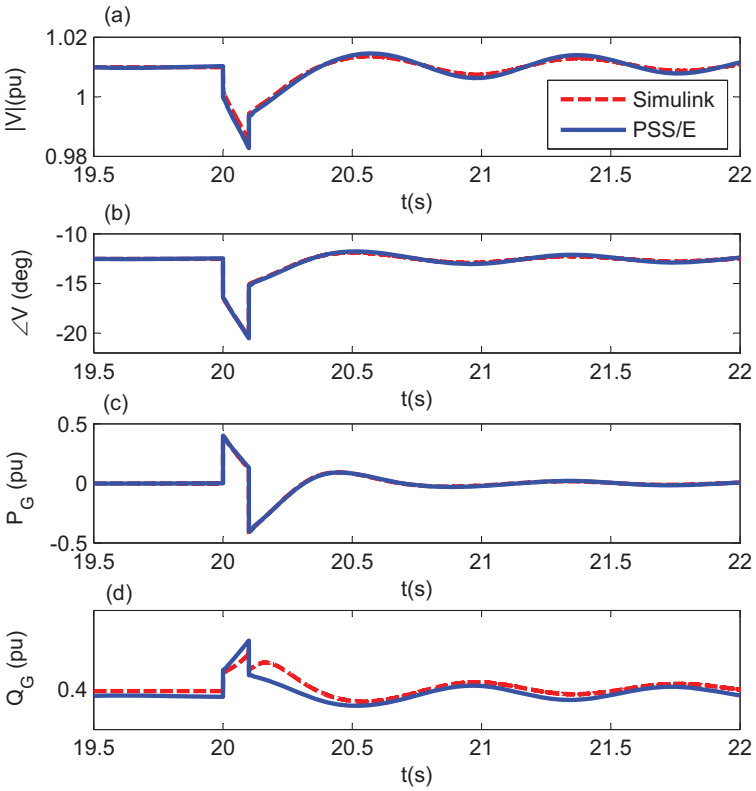

Figure 2.11: Voltage magnitude, angle, active and reactive power of machine C3 on bus 8 due to line 3 tripping and reclosure

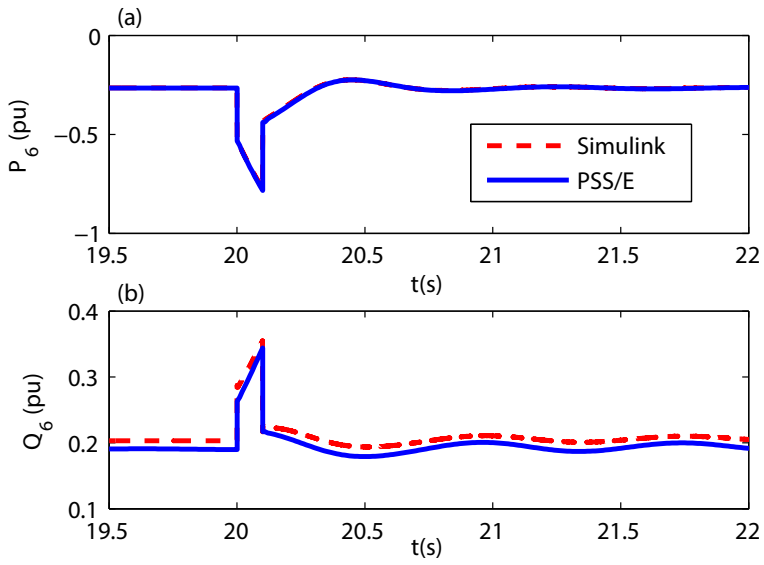

Figure 2.12: Active and reactive power flow changes of line 6 due to line 3 tripping and reclosure

results obtained from PSS/E. The generators, exciters, and DC line models used in the PSS/E simulations are GENROU, IEEET1 and CDC4T, respectively. In the first case study, the test system is subjected to an L-L-L-G fault on bus 13 at time $t = 2$ s that self-clears after 5 cycles. Figs. 2.9-2.10 show the system's dynamic response to this fault. In the second case study, line 3 between buses 2 and 3 is opened by the line circuit breakers at time $t = 20$ s and successfully reclosed after 5 cycles. Figs. 2.11-2.12 show the system's dynamic response to this disturbance.

Figs. 2.9-2.10 and Figs. 2.11-2.12 show close agreements between the corresponding systems dynamic responses using MATLAB/Simulink and PSS/E. The small discrepancies are likely due to a difference in the DC link model (the CDC4T model used in the PSS/E simulations does not represent the DC line and DC controller dynamics [39]).

2.6.3 Validation of the Linearized Dynamic Model

To validate the automatically generated linearized model, the dynamic behaviour of the IEEE 14-bus 1-segment test system due to a 5% step increase in the reference voltage of generator 2 (V_{ref2}) is simulated using nonlinear and linearized models. The simulation results from both models are compared in Figs. 2.13-2.14. Close agreement between the corresponding results of the linearized and nonlinear models verify the accuracy of the linearized model.

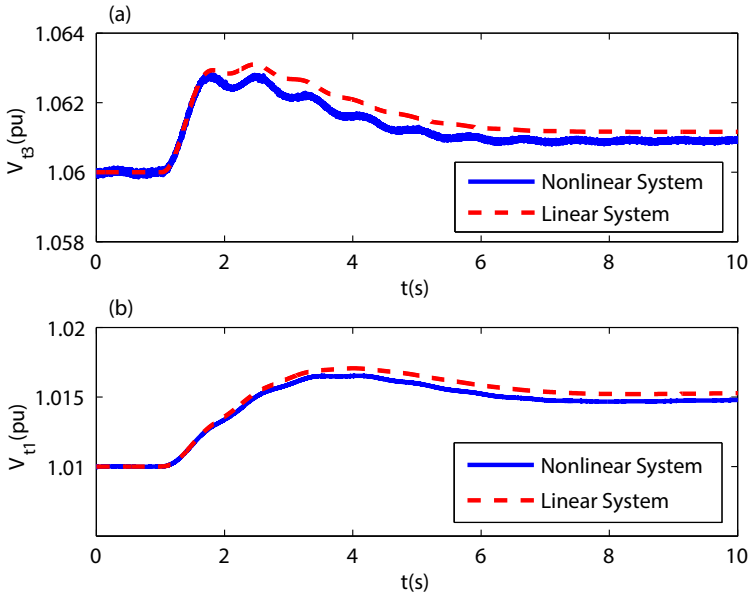

Figure 2.13: Voltages of buses 1 and 3 due to 5% step change in the voltage reference of G2

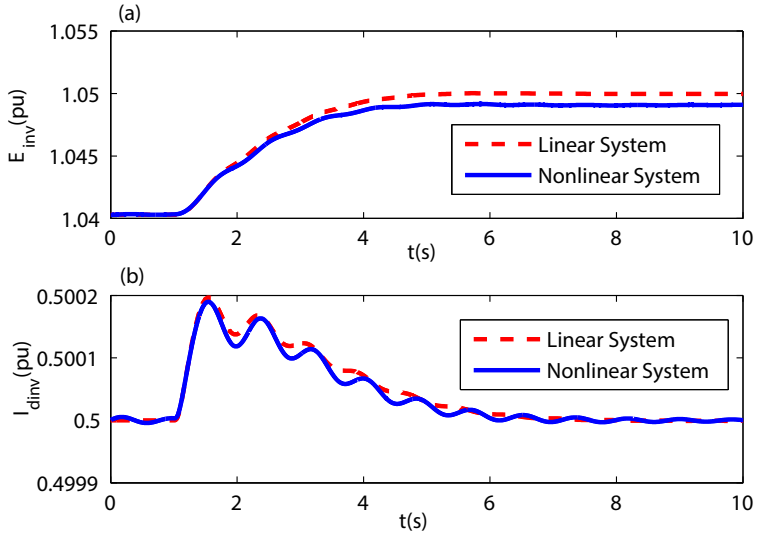

Figure 2.14: DC current and inverter bus voltage dynamics due to 5% step change in the voltage reference of G2

2.7 Conclusions

This chapter presents a MATLAB/Simulink-based framework which can be used for controller design in interconnected AC-DC power systems (This framework will be used in the following chapters to design controllers). The key feature of this platform, i.e., modeling flexibility, accuracy of time-domain simulation, and automatic derivation of linear models, make it a feasible analytical tool for the linear controller design. The developed platform also enables for easy inclusion of additional component models, e.g., those of FACTS controllers and custom-specified apparatus, and automatic linearization of the models for controller design.

The MATLAB/Simulink-based AC-DC power system model can also be used as an independent platform for the time-domain simulation of AC-DC power system transient phenomena. The accuracy of the simulation results based on the developed model was validated by comparison to the corresponding simulation results obtained from PSS/E. The capability to automatically extract an accurate linear model of an AC-DC power system from the complete differential-algebraic nonlinear model and the accuracy of the nonlinear model were also demonstrated by comparison of the linear and nonlinear model responses to small-signal dynamics. Automatic extraction of the linear state space model enables (i) linear control design and (ii) ease of adjusting the designed controller due to changes in the system operating point, configuration and parameter values.

Chapter 3

HVDC Local Supplementary Control (LSC)

3.1 Introduction

Supplementary control of the classical HVDC rectifier station, which provides modulation to the rectifier current controller, has been long recognized as an effective means for the mitigation of oscillations of interconnected power systems [33]. The technical literature reports the following approaches for the design of the HVDC supplementary controller:

- Nonlinear feedback linearization method [16]: In this method, system dynamics are transformed into a linear form using a nonlinear pre-feedback loop, and then, for the linearized system, another feedback loop is designed. The main advantage of this approach is that the proposed state feedback linearization does not rely on the assumption that there is only a small deviation of the states from the equilibrium. However, it relies on finding the nonlinear pre-feedback loop, which is not always possible.

- Numerical optimization methods: The optimization based methods search in the parameter space to identify the set of control parameters for the desired performance and can utilize nonlinear programming [40, 41], and heuristic methods, e.g., neural networks and genetic algorithms [42]. One of the drawbacks of these methods is that the search in the parameter space is time-consuming.

- LQG controller: The linear quadratic regulator (LQR), in which the objective function is a quadratic function of the state vector and control inputs, has been widely used in the design of power system controllers [43]. In the LQR design, if all

system states are not measured, an observer is required to estimate the states. The LQ regulators and the state estimators together form the LQG controller. While LQG control has been widely studied in the context of power systems [44, 45], it is not able to incorporate all system constraints, e.g., hard limits on the control signal.

To overcome the drawbacks of these methods and enhance the damping of inter-area oscillations in power systems, this thesis proposes an HVDC supplementary controller based on the MPC methodology. MPC combines a prediction strategy and a control strategy to hold the system output at a reference value by adjusting the control signal. The advantage of the MPC compared with other optimal control strategies, e.g., LQG, is that it adjusts the control signal to achieve the objectives while explicitly respecting the plant constraints [46, 47].

This chapter describes the MPC-based and LQG-based supplementary controller design procedures and evaluates the performance of a discrete-time MPC-based HVDC supplementary controller for mitigating oscillatory modes of two study systems. This chapter also compares the damping effect of the designed MPC-based controller with that of an LQG controller for the same test systems. While the proposed MPC-based controller can be applied to both LCC- and VSC-HVDC systems, this thesis only considers the LCC-HVDC system.

3.2 MPC and LQG Controllers

Optimal control theory determines the control signal of a dynamic system over a time horizon to minimize a performance index (cost function). This section summarizes two optimal controllers, the MPC-based and LQG controllers, which are designed and evaluated in the reported studies.

3.2.1 Linear Quadratic Gaussian (LQG) Control

A linear dynamic system can be described by

$$\dot{\mathbf{x}}(t) = \mathbf{A}\mathbf{x}(t) + \mathbf{B}\mathbf{u}(t) + \boldsymbol{\epsilon}(t), \tag{3.1}$$

$$\mathbf{y}(t) = \mathbf{C}\mathbf{x}(t) + \mathbf{D}\mathbf{u}(t) + \boldsymbol{\nu}(t), \tag{3.2}$$

where $\mathbf{x}(t)$, $\mathbf{y}(t)$, $\mathbf{u}(t)$, $\boldsymbol{\epsilon}(t)$ and $\boldsymbol{\nu}(t)$ are the state, output, input, process noise and measurement noise vectors, respectively. The goal of an LQR is to identify a state-feedback

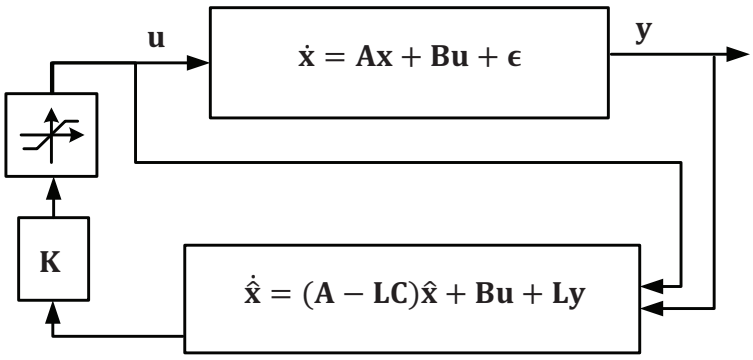

Figure 3.1: Block diagram of the LQG controller with a limiter

law $\mathbf{u}(t) = \mathbf{K}\mathbf{x}(t)$ for the system of (3.1)-(3.2), subject to additive white Gaussian noises, that minimizes the quadratic cost function

$$J(\mathbf{u}) = \lim_{\tau \to +\infty} \int_0^{\tau} \left\{ \mathbf{x}^T(t)\mathbf{Q}\mathbf{x}(t) + \mathbf{u}^T(t)\mathbf{R}\mathbf{u}(t) \right\} dt, \tag{3.3}$$

where $\mathbf{Q}$ and $\mathbf{R}$ are weighting matrices and commonly constructed as diagonal matrices [43]. Entries of $\mathbf{Q}$ and $\mathbf{R}$ penalize the deviations of the corresponding state variables from zero and variations of the controller output, respectively. $\mathbf{Q}$ and $\mathbf{R}$ determine the trade-off between tracking performance and control effort. The optimal feedback gain, $\mathbf{K}$, is given by

$$\mathbf{K} = \mathbf{R}^{-1}\mathbf{B}^T\mathbf{S}, \tag{3.4}$$

where $\mathbf{S}$ is the solution of the Riccati equation

$$\mathbf{A}^T\mathbf{S} + \mathbf{S}\mathbf{A} - (\mathbf{S}\mathbf{B})\mathbf{R}^{-1}(\mathbf{B}^T\mathbf{S}) + \mathbf{Q} = 0. \tag{3.5}$$

LQ-optimal state feedback requires full state measurement. If all the states are not measured, an observer, e.g., a Kalman filter [48], is required. The combination of the LQR with a Kalman filter forms the LQG controller as shown in Fig. 3.1.

3.2.2 Model Predictive Controller [49]

The objective of an MPC is to hold the system output at a reference value by adjusting the control signal. Fig. 3.2 represents the block diagram of the MPC, where, $\mathbf{r}$, $\mathbf{u}$, $\boldsymbol{\epsilon}$, $\boldsymbol{\nu}$, $\mathbf{y}$ and $\bar{\mathbf{y}}$ represent the reference, control, process noise, measurement noise, measured output, and true value of the output signals, respectively.

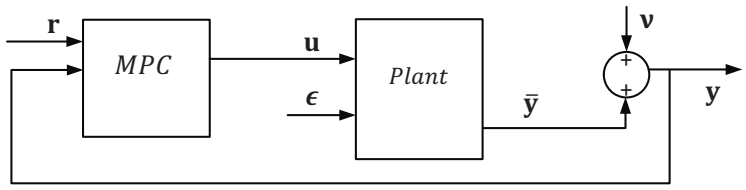

Figure 3.2: Block diagram of the MPC

An MPC combines a prediction strategy and a control strategy. The main difference between the MPC and other optimal control strategies, e.g., the LQG approach, is that it adjusts the control signal to achieve the objectives while respecting the control constraints. Moreover, the MPC optimization horizon is always finite (versus LQG optimization, which often has an infinite time horizon). The additional constraints are typically upper or lower bounds of the control signals or their derivatives. This chapter adopts discrete-time MPC since it is computationally less demanding as compared with the continuous-time MPC.

The controller operates in two phases: estimation and optimization. In the former, the current true outputs (i.e., outputs without measurement noise), $\bar{\mathbf{y}}(k)$, and states of the system, $\mathbf{x}(k)$, are estimated. In the latter, first, the future outputs, $\mathbf{y}(k+1), \ldots, \mathbf{y}(k+p)$, where p is the prediction horizon, are estimated as a function of the control moves using the past and current measurements. Then, based on the values of the reference signals and constraints over the prediction horizon, M control moves, $\mathbf{u}(k), \mathbf{u}(k+1), \ldots, \mathbf{u}(k+M)$, where M $(1 <= M <= p)$ is the control horizon, are calculated. p and M are basic tuning parameters for MPC. p is generally set long enough to capture the steady-state effects of all calculated future control moves [47]. A larger M improves the performance of the MPC at the expense of additional computations [47]. Finally, the controller move at the current sampling time $\mathbf{u}(k)$ is applied to the system. At the next sampling time, new measurements are obtained and the control signal is revised. This procedure is repeated at each sampling instant.

At each sampling instant, the MPC estimates the current states $\mathbf{x}(k)$ from the available measurements. If all the states are measured, the state estimation only considers the effect of noise on the measurements. The discretized model of the system, (3.1)-(3.2), is

$$\mathbf{x}(k+1) = \mathbf{A}\mathbf{x}(k) + \mathbf{B}\mathbf{u}(k) + \boldsymbol{\epsilon}(k), \tag{3.6}$$

$$\mathbf{y}(k) = \mathbf{C}\mathbf{x}(k) + \boldsymbol{\nu}(k), \tag{3.7}$$

where $\boldsymbol{\nu}(k)$ and $\boldsymbol{\epsilon}(k)$ are the measurement and process noise assumed to be independent

(of each other), white, and with normal probability distributions. The current outputs and states of the system are estimated as

$$\hat{\mathbf{x}}(k|k) = \hat{\mathbf{x}}(k|k-1) + \mathbf{L}(\mathbf{y}(k) - \hat{\mathbf{y}}(k)), \tag{3.8}$$

$$\hat{\mathbf{y}}(k) = \mathbf{C}\hat{\mathbf{x}}(k|k-1), \tag{3.9}$$

where $\mathbf{L}$ is the Kalman gain [48]. The main difference between the LQG and MPC optimization is that the MPC optimization is over a finite horizon and constrained. The MPC action at time k is obtained by solving the optimization problem

$$\min_{\Delta\mathbf{u}(k|k),\ldots,\Delta\mathbf{u}(k+M-1|k)} \sum_{i=0}^{p-1} \left\{ \sum_{j=1}^{n_y} w_{i+1,j}^{y} (y_j(k+i+1|k) \right. \tag{3.10}$$
$$\left. -r_j(k+i+1))^2 + \sum_{j=1}^{n_u} w_{i,j}^{\Delta u} \Delta u_j(k+i|k)^2 \right\},$$

$$\overbrace{\begin{array}{c} u_{jmin}(i) \le u_j(k+i|k) \le u_{jmax}(i), \\ \Delta u_{jmin}(i) \le \Delta u_j(k+i|k) \le \Delta u_{jmax}(i), \\ u_j(i+k) = \mathbf{u}_j(i+k-1) + \Delta u_j(i+k|k), \end{array}}^{\forall i=0,\ldots,p-1, \forall j=1,\ldots,n_u} \tag{3.11}$$

$$\Delta\mathbf{u}(k+h|k) = 0, \forall h = M, \ldots, p-1. \tag{3.12}$$

where $w_{i,j}^{y}$ is the weight for output j, $w_{i,j}^{\Delta_u}$ is the rate weight for control signal j at i step ahead from the current step, $r_j(i)$ is the set-point at time step i, k is the current step, n_y is the number of outputs, $\Delta u_j(k+i|k)$ is the adjustment of control signal j at time step $k+i$ based on the measurements at time step k, and n_u is the number of control signals. $u_{j,min}$, $u_{j,max}$, $\Delta u_{j,min}$ and $\Delta u_{j,max}$, are the lower and upper bounds on the control signal and control signal variation, respectively. The control signal applied to the plant is $\mathbf{u}(k) = \mathbf{u}(k-1) + \Delta\mathbf{u}(k|k)$. Complete details of the MPC optimization are provided in Appendix A.

For set-point tracking purposes, the cost function only consists of the weighted sum of the deviation of the outputs from their reference values and a weighted sum of the controller adjustments over the prediction horizon. The weights specify the trade-offs in the controller design and reflect the importance of the corresponding variables to the overall performance of the system. If a particular output weight is large, deviations of the corresponding output dominate the cost function. Increasing the rate weights forces the controller to make smaller adjustments and degrades set-point tracking. In the reported

studies, the constraints are assumed to be hard constraints and thus must not be violated. A quadratic optimization solver, based on the KWIK algorithm [50], is used to solve the optimization problem.

The communication delay T_d associated with the measured signal y_m can be considered in the system by adding one state equation to the plant model based on the time delay Padé approximation [28, 51] as

$$\frac{dy_d}{dt} = \frac{2}{T_d}(-y_d + y_m - \frac{T_d}{2}y_m), \tag{3.13}$$

where y_d is the delayed signal associated with y_m.

While the LQR requires full state feedback, neither LQG nor MPC requires full state feedback. These controllers are equipped with observers which provide the state estimates. A brief description of the prediction process is provided in Appendix A. The models used for online dynamic security assessment (DSA), [52–54], can be used for the MPC and LQR design as well.

The study results reported in this chapter and also the performance comparison of the LQG-based and MPC-based controllers are based on the assumption that the system model is available. This model can be derived using the same methods applied in the online DSA. Since the robustness of a generic controller for nonlinear systems, e.g., LQG or MPC, cannot be guaranteed, further action are required to ensure the desired controller performance in case of uncertainties in the system parameters, topology, operating point and load conditions [46, 55–57].

3.3 HVDC LSC Based on Optimal Control Theory

In this section, to investigate the performance of the designed controllers which are used to damp oscillations within a segment, two study systems (WSCC and IEEE 14-bus 1-segment) with different characteristics in terms of the integration of the DC system in the AC system are selected. The former has an HVDC link in parallel with an AC path, and the latter has an HVDC link embedded in the AC system. Designing a controller to damp the oscillations for the IEEE 14-bus 1-segment system compared to the WSCC system is more challenging; since control of the HVDC link in the former configuration affects more than one AC path. The details of the IEEE 14-bus 1-segment system are provided in chapter 2.

In this study, the WSCC 9-bus system [58] is augmented with a classical HVDC link as shown in Fig. 3.3. The WSCC system includes three T-G units and nine AC

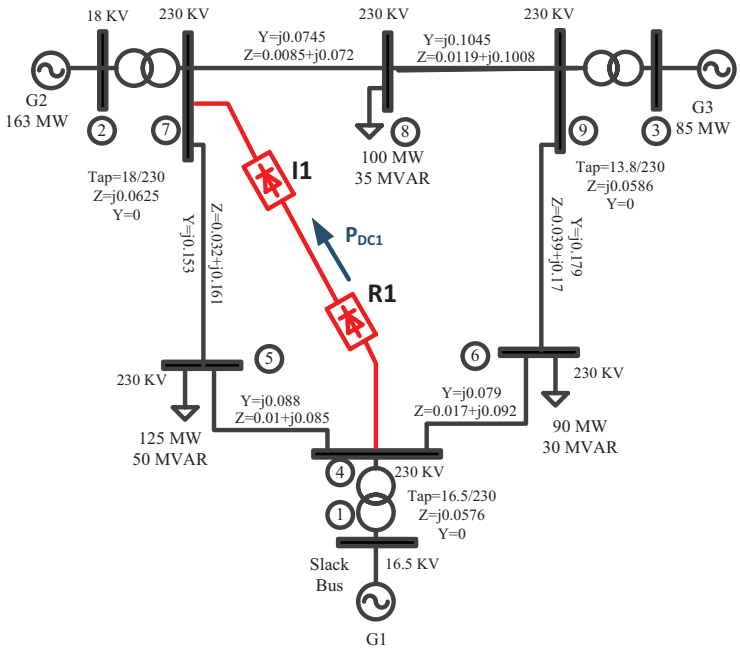

Figure 3.3: Schematic one-line diagram of the WSCC system

transmission lines. The rectifier and inverter stations are connected to buses 4 and 7, respectively. The parameters of the WSCC system, including those of the T-G units and their IEEE Type-1 exciter systems, are given in [58]. The HVDC link and control parameters are given in [37].

To mitigate the inter-area oscillatory modes of the WSCC system and the IEEE 14-bus 1-segment system, the HVDC supplementary controller modulates the reference (set-point) of the corresponding HVDC rectifier current controller, Fig. 3.4. The operating point of each study system, prior to each case study, is obtained from an AC-DC power flow solution when the HVDC link transfers 50 MW (WSCC system) and 25 MW (IEEE 14-bus 1-segment system). The LQG controller and the MPC-based controller, for each study system, are designed based on the linearization of the system model about the steady-state operating point. The linearized model of each study system is determined using the method discussed in chapter 2. The inter-area modes of the linearized WSCC and IEEE 14-bus 1-segment systems, with frequencies less than 2 Hz and damping ratios less than 0.5, are presented in Tables 3.1 and 3.2, respectively. The states with participation factors [1] greater than 0.06 in each mode and their corresponding participation factors are also given in Tables 3.1 and 3.2. For a complex pair of eigenvalues $\kappa_i = \sigma_i \pm j\omega_i$, the damping ratio ζ_i and frequency f_i are defined as $\frac{-\sigma_i}{\sqrt{\sigma_i^2+\omega_i^2}}$ and $\frac{\omega_i}{2\pi}$, respectively [1].

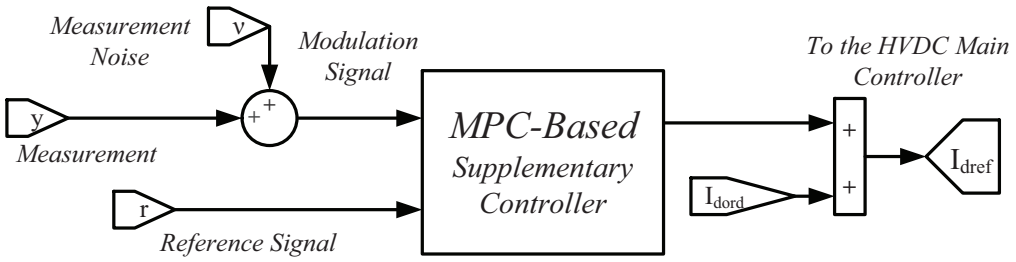

Figure 3.4: Block diagram of the MPC-based HVDC supplementary controller

Table 3.1: Eigenvalues of the linearized WSCC system

Inter-Area Mode	Frequency (Hz)	Damping Ratio	Associated States (Participation Factors)
1	1.385	0.04	$\delta_2(0.4)$, $\omega_2(0.3)$, $\omega_1(0.14)$, $\delta_3(0.07)$
2	0.142	0.29	$E_{fd2}(0.24)$, $E'_{q2}(0.17)$, $E'_{q1}(0.11)$, $E_{fd1}(0.1)$, $\Psi_{1d_2}(0.07)$

3.3.1 LSC Based on LQG Method

To prevent ill-conditioning when solving the Riccati equation, it is necessary to adopt a reduced-order system model to design the LQG controller. The Kalman decomposition [59] technique is used to perform model order reduction by removing the uncontrollable and unobservable states. The reduced orders of the IEEE 14-bus 1-segment and WSCC systems are 63 and 41, respectively.

Choosing the weighting matrices is a critical step in designing the LQG controller. In this chapter, a systematic approach to set the weighting matrices is proposed. In this

Table 3.2: Eigenvalues of the linearized IEEE 14-bus 1-segment system

Inter-Area Mode	Frequency (Hz)	Damping Ratio	Associated States (Participation Factors)
1	1.26	0.05	$\omega_{C2}(0.2)$, $\delta_{C2}(0.16)$, $\omega_{C3}(0.13)$, $\delta_{C3}(0.11)$, $\Psi_{2q_{C2}}(0.08)$, $\omega_{C1}(0.08)$, $\delta_{C1}(0.07)$
2	1.37	0.26	$\delta_{C3}(0.27)$, $\delta_{C1}(0.23)$, $\omega_{C3}(0.09)$, $\delta_2(0.07)$
3	1.47	0.32	$\delta_{C1}(0.24)$, $\delta_{C2}(0.17)$, $\omega_{C1}(0.14)$, $\omega_{C3}(0.11)$

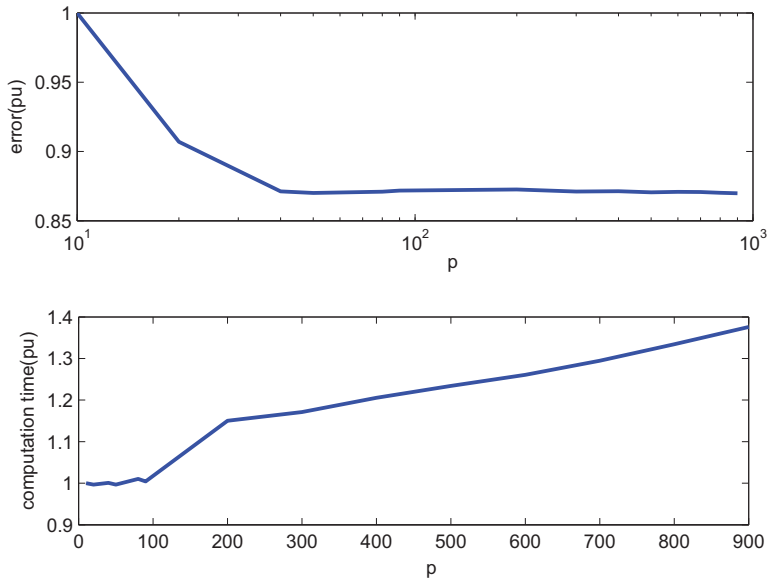

Figure 3.5: The control performance and computation time for different values of p (WSCC system)

approach, to damp the mode of interest, the weights corresponding to this mode in the **Q** matrix are set to non-zero values and the weights corresponding to the rest of the modes are set to zero. To specify the **Q** matrix, the participation factors of the states of the system in the mode of interest are calculated and those with participation factor greater than 0.06 are given non-zero weights. The weight assigned to each of these states corresponds to the participation factor of each of the states in the mode which should be damped.

The inter-area oscillatory modes of interest in the WSCC and the IEEE 14-bus 1-segment systems are at frequencies of 1.38 Hz and 1.26 Hz, respectively. These modes have the least damping compared to the rest of the modes. The inputs to the controller are determined through a modal observability analysis of the network [1]. For the WSCC system, the voltage angles of buses 2, 4, 5, 6, 7, 8 and the active power flows of lines 1 and 9 exhibit the highest observability of the critical mode and are selected as the input signals of the controller. For the IEEE 14-bus 1-segment system, voltage angles of buses 2, 4, 5, 6, 7, 9, 14 and the active power flow of lines 1 and 3 are selected as the controller inputs, based on the same method used for the WSCC system. To maintain the robustness feature of the LQR in the LQG design, the weighting matrices of the Kalman filter are tuned such that the loop transfer function of the system with the LQG controller approaches the loop transfer function of the system with the LQR controller [60].

To limit the impact of modulation on the network flows, limit transients and avoid

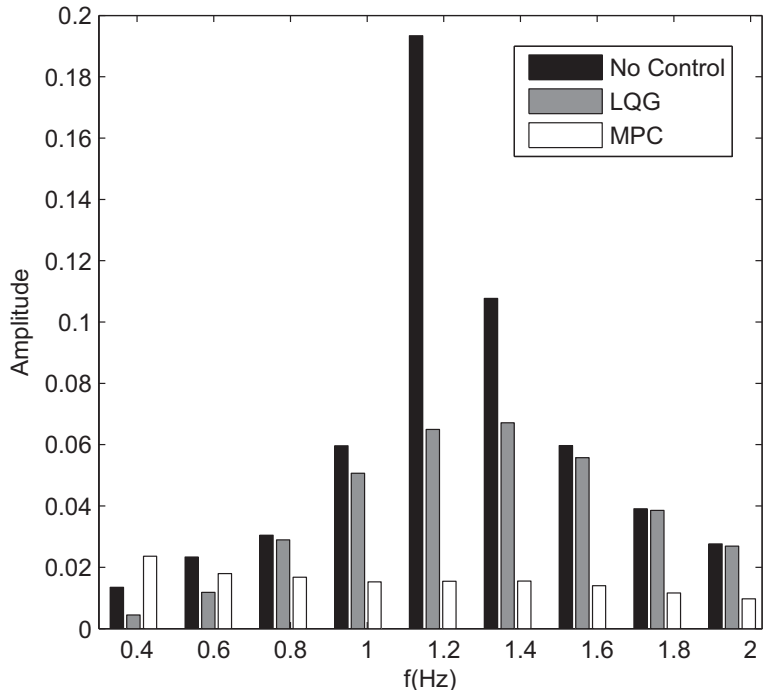

Figure 3.6: The single-sided amplitude spectrum of bus 4 voltage angle (IEEE 14-bus 1-segment system)

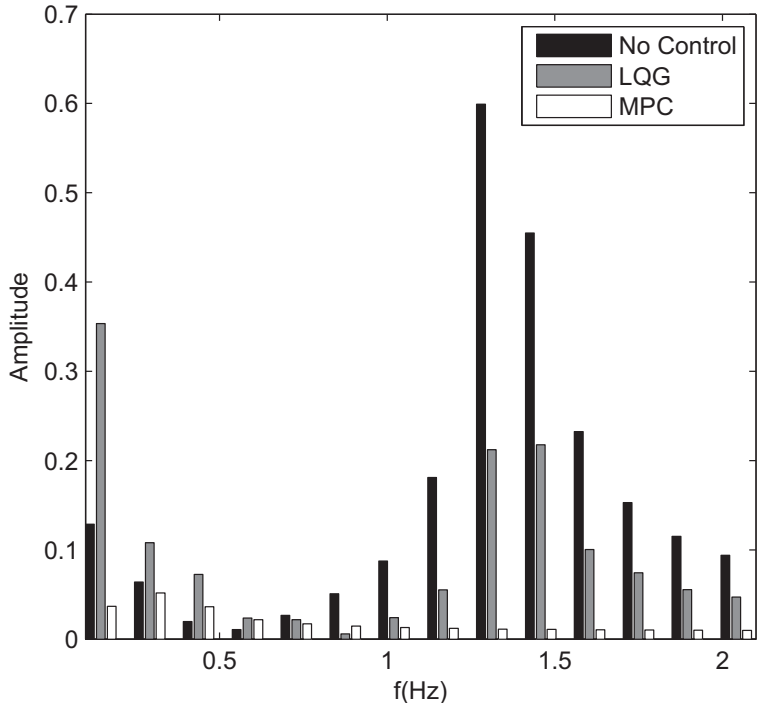

Figure 3.7: The single-sided amplitude spectrum of bus 7 voltage angle (WSCC system)

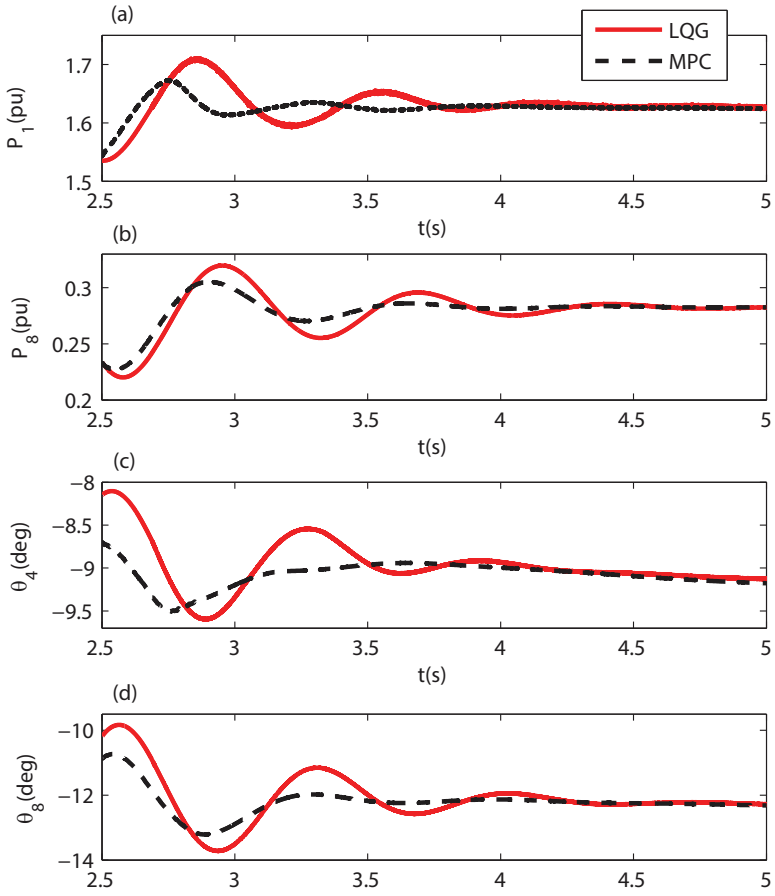

Figure 3.8: IEEE 14-bus 1-segment system dominant inter-area mode: (a) active power flow of line 1, (b) active power flow of line 8, (c) bus 4 voltage angle and (d) bus 8 voltage angle

potential voltage fluctuations in other areas, the DC power modulation must be bounded. The bound on the DC power modulation limits the deviation of the operating point from the optimal system operating point. A representative value of 10% was chosen to be the permissible value in this system. This limit would ultimately be decided by the system operator based on system voltage and security limits. Since the LQG controller does not take into account the constraints on the inputs and outputs of the system, the control signal may exceed the limits. Therefore, a limiter is imposed on the controller output.

3.3.2 LSC Based on MPC Method

The MPC-based controller output (modulation signal) is added to the HVDC link reference current signal and its inputs are the same as those of the LQG controller. If oscillations in the measurement signals which display the most observability of the critical mode are damped out, then adequate damping for those modes in the entire system

is achieved. In this study, the measurement noise is modeled as a white noise with unity amplitude.

To choose the design parameters, a performance index $error = \int_0^t \Delta\mathbf{p}(t)^T \Delta\mathbf{p}$ is defined in which $\Delta\mathbf{p}$ is the power deviation vector of all the AC transmission lines from their steady-state values and t is the simulation time. This performance index represents the power deviation of all the AC transmission lines from their steady-state values during the simulation time. The most important design parameter with respect to the control performance and computation time is the prediction horizon p. Fig. 3.5 shows the trade-off between the computation time and control performance for different values obtained with p for the WSCC system (by increasing p the control performance improves and the computation time increase). In Fig. 3.5, the computation time and the error at different values of p are divided by those of p=10. To have a fair balance between the computation time and the performance, for the WSCC system, p, control horizon M, and control interval (sampling time) are selected to be 50, 5, and 0.02 s, respectively. In Fig. 3.5, for p greater than 40, the error index becomes almost flat and for the minimum error index, at p=50 the computation time is at its minimum. The same parameters for the IEEE 14-bus 1-segment system are 500, 5, and 0.02 s, respectively.

3.4 Application of the LSC for Small-Signal Dynamic Stability Enhancement

The proposed LSC is applied to two study systems, WSCC and IEEE 14-bus 1-segment. The objectives of this section are to (i) demonstrate the MPC and LQG application procedures, (ii) illustrate and verify the effectiveness of the LSC for mitigating inter-area oscillations and (iii) highlight the superior performance of the MPC-based LSC as compared with the widely used LQG-based LSC. The reported studies of this section consider three scenarios: (i) no supplementary controller in service (no control), (ii) LQG controller operational (LQG), and (iii) MPC operational (MPC). For each case study, the system under consideration is subject to a 5-cycle, temporary, L-L-L-G fault at the inverter AC bus (bus 4 of the IEEE 14-bus 1-segment system and bus 7 of the WSCC system).

Figs. 3.6-3.7 show the frequency spectrum of the voltage angle of the inverter bus (with respect to the voltage angle of bus 1) obtained from the discrete Fourier transform. Fig. 3.6 shows that the 1.26 Hz low-frequency oscillatory mode (inter-area mode) of the IEEE 14-bus 1-segment system is excited by the disturbance. Fig. 3.6 illustrates that the MPC effectively reduces the amplitude of the dominant mode by a factor of 9 while the

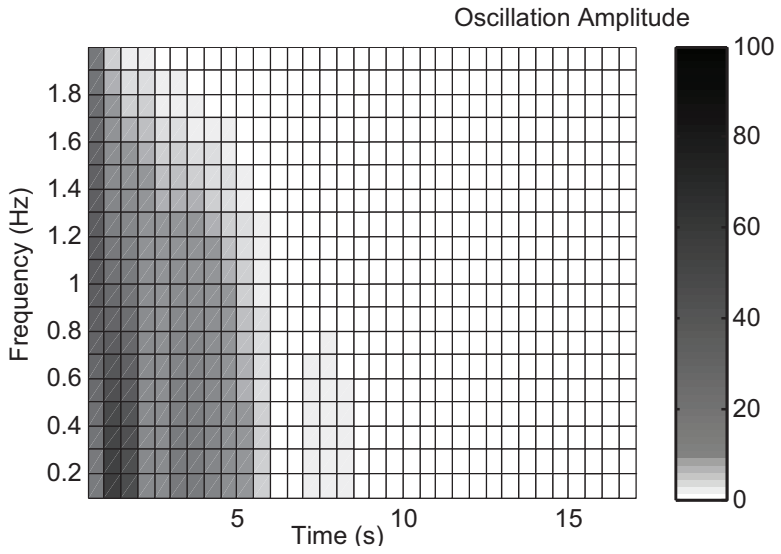

Figure 3.9: The spectrogram of bus 4 voltage angle deviations from the steady-state value for the IEEE 14-bus 1-segment system (MPC in service)

LQG controller reduces the amplitude by a factor of 3.

Fig. 3.7 shows that the MPC reduces the amplitude of the 1.38 Hz dominant inter-area mode of the WSCC system to one fourth of the amplitude observed with the LQG controller in service. Both the MPC-based and LQG controller are designed to damp the dominant oscillatory modes of the system. In doing so, these controllers may slightly reduce the damping ratios of the other modes. However, the damping impact of the controllers on the non-dominant modes is insignificant as compared to the impact on the dominant mode. The time-domain behavior of the IEEE 14-bus 1-segment system, subject to the fault at t=2 s, is shown in Fig. 3.8. The faster reduction in oscillations shows the MPC is more effective in damping the dominant inter-area mode as compared with the LQG controller.

Traditional analyses such as eigenvalue analysis are commonly used to evaluate the performance of linear systems. Since the closed-loop system of this study is nonlinear, the transfer function of the closed-loop system does not exist (the transfer function of the linearized system changes at each operating point) and eigenvalue analysis is not possible. To address this issue, spectrograms are used to show how all the frequency components of the system change during the time. Spectrograms simultaneously capture the time-domain and frequency-domain information of the system signals.

The spectrograms of the voltage angle deviations on bus 4 of the IEEE 14-bus 1-segment system are depicted in Figs. 3.9-3.10. The spectrogram shows the amplitude of the time-dependent Fourier transform of the bus 4 voltage angle deviations versus

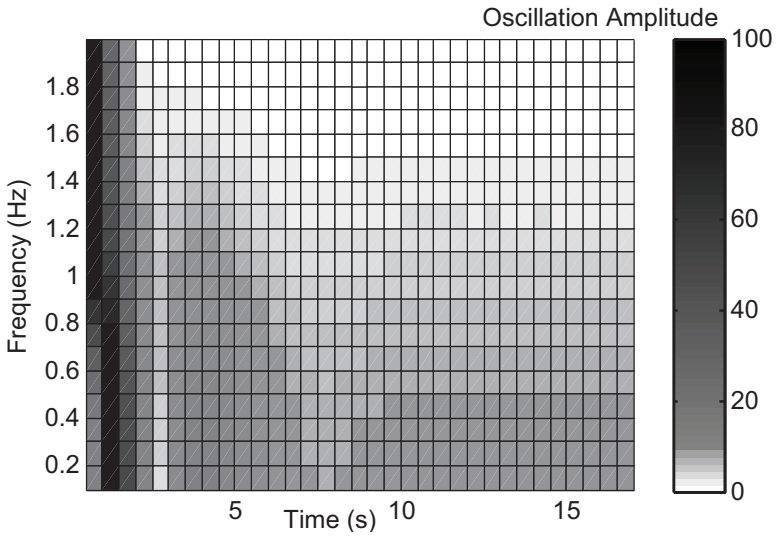

Figure 3.10: The spectrogram of bus 4 voltage angle deviations from the steady-state value for the IEEE 14-bus 1-segment system (LQG controller in service)

time. The time-dependent Fourier transform is the discrete-time Fourier transform for a sequence computed by a sliding time window of 1000 points and 50% overlap between the segments. Figs. 3.9-3.10 show that the MPC-based controller damps the oscillations faster than the LQG controller. Furthermore, with reference to the modes of interest specified in Table 3.2, the amplitudes of the frequency components of the selected signal when the MPC is in service is smaller compared to the case when the LQG controller is in service, even at early times. For a fault of the same duration applied to every other bus on the system, with the MPC-based supplementary controller in service, faster damping is achieved as compared to when the LQG-based supplementary controller is in service.

The reason for the superior performance and fast damping of the MPC-based controller as compared with those of the LQG controller is its ability to optimize the objective function while respecting the system constraints. The control signals of the MPC-based and LQG controllers are shown in Fig. 3.11. The L-L-L-G fault at the inverter station requires a large control signal to achieve a short settling time. In the case of the LQG controller, since the control signal must be bounded and this constraint is not considered in the LQG controller optimization, the controller provides a large control signal which is then constrained to its limits. Therefore, the controller performance deteriorates. If the parameters are tuned such that the control signal remains between its bounds, the damping effect diminishes.

In general, in the design of the LQG controller, the weighting matrices should be selected to retain the control signal between its lower and upper bounds. If the control

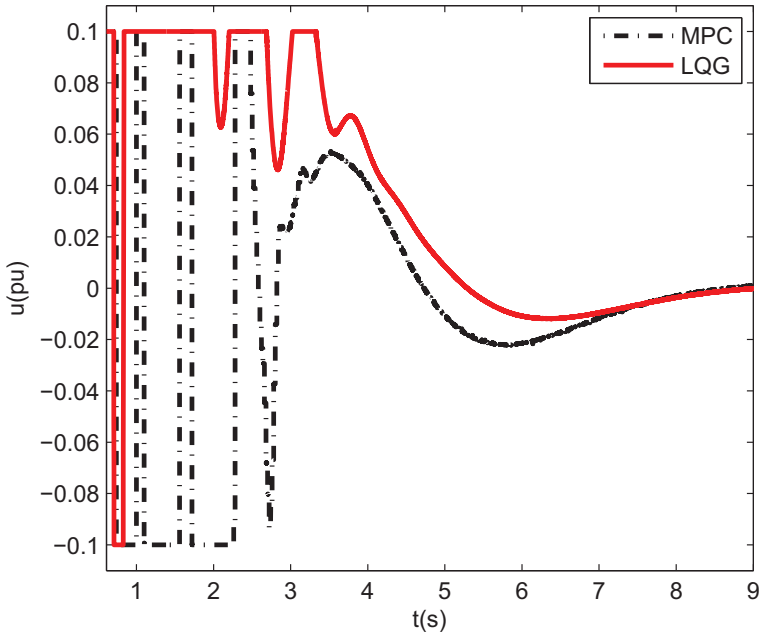

Figure 3.11: Control signal for the cases with LQG and MPC after an L-L-L-G fault on bus 4 (IEEE 14-bus 1-segment system)

signal exceeds its limits repeatedly, the actuator will be saturated and the controller will not be effective. If the gains are modified by adjusting the control weighting matrix such that the control signal remains between its bounds, the controller response time increases. In order to keep the control signal bounded, a small gain should be selected for the LQG controller and, since this gain does not change with time, the controller will have less influence on the system response. However, in the case of MPC, the "gain" is allowed to vary with time and, when feasible, a larger gain can be applied to damp out the oscillations faster.

Fig. 3.12 highlights the effect of communication time delay of the remote signals on the damping effect of the MPC-based supplementary controller. It is assumed that all signals are delayed 200 ms [51]. Fig. 3.12 indicates that the MPC-based supplementary controller performance remains satisfactory despite the introduction of delay.

3.5 Conclusions

In this chapter, a supplementary classical HVDC controller based on the model predictive control (MPC) methodology and linear quadratic Gaussian (LQG) control is proposed, designed and applied to two study systems, WSCC and IEEE 14-bus 1-segment, to mitigate the dominant inter-area oscillatory modes. The small-signal dynamic modeling approach is used to determine the critical inter-area modes of the study systems and a

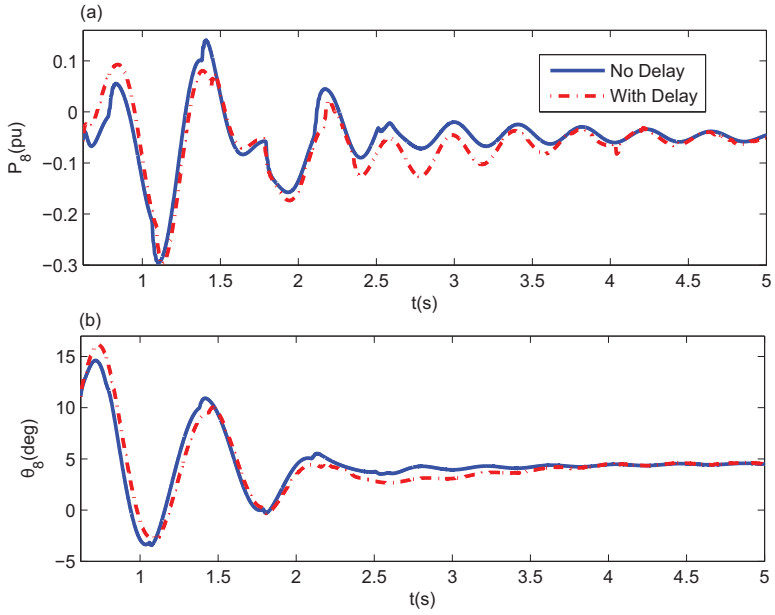

Figure 3.12: WSCC system dominant inter-area mode: (a) active power flow of line 8 and (b) bus 8 voltage angle

systematic approach to design the MPC-based and LQG controllers is proposed. The main feature of the MPC control is its ability to cope with hard constraints on inputs, outputs, and states. Since these constraints are directly included in the optimization problem formulation, future constraint violations are prevented. The MPC can address actuator limitations and enables operation closer to the system constraints which results in faster system response. Furthermore, while the LQG controller has a static gain, the online optimization of the MPC permits the gain of the controller to vary with time, resulting in faster damping. This chapter also reports the simulation results of the designed MPC-based and LQG-based HVDC supplementary controllers for the mitigation of inter-area oscillations. Simulation results show that both are beneficial to overall system dynamic performance and lead to damped low-frequency oscillations under small-signal disturbances; however, the MPC methodology provides faster recovery times after faults. The proposed supplementary controller has satisfactory performance even if the communication delay is accounted for.

Chapter 4

Mitigation of Oscillations by Control of the Propagation of Oscillatory Modes Using an HVDC Supplementary Control Scheme

This chapter presents and investigates a new LCC-HVDC global supplementary control (GSC) strategy for stabilizing and enhancing the dynamic performance of a large AC system that is segmented by LCC-HVDC links. The GSC can stabilize the AC system while either minimizing the propagation of oscillatory dynamics from one segment to other segments (GSC1) or enabling their controlled transfer from a disturbed segment to other segments (GSC2).

In a DC-segmented AC grid, the impact of the LCC-HVDC links on the propagation of oscillatory dynamics initiated within a segment can be manifested through the following mechanisms:

1. Partial "buffering" of the HVDC links through their main (constant current (CC) and constant voltage (CV)) controllers [1], which inherently limit the transfer of dynamics between the AC segments.

2. The use of HVDC supplementary controllers to selectively control the transfer of oscillatory dynamics among the segments.

The main idea of this chapter is to deploy coordinated supplementary controls of inter-segment HVDC links to (i) stabilize the system and (ii) achieve one of the following objectives, based on the system requirements:

(ii-a) Confine the oscillatory dynamics within the initiating segment

(ii-b) Selectively permit the controlled transfer of oscillatory dynamics from the perturbed segment to other segments in order to enhance the overall system damping

The controllers used to achieve these two objectives are referred to throughout the remainder of the chapter as the global supplementary controllers GSC1 and GSC2, respectively. To the best of our knowledge, neither scheme has been explored in the technical literature in the context of DC-segmented systems. Since the measurements (inputs to the controllers) are received from all the segments, the proposed control schemes are referred as "global" supplementary control schemes.

Because maintaining system stability is a goal for both of the GSCs, and the weighting matrices of an LQG controller can be selected such that the closed-loop stability of the (linearized) system is guaranteed [61], both GSC1 and GSC2 are implemented as LQG controllers. Both GSC1 and GSC2 provide simultaneous modulation of the current order and voltage reference of the corresponding rectifier and inverter stations.

4.1 GSC Based on Optimal Control Theory

Fig. 2.3 depicts the CC and CV modes of the main HVDC controller and the supplementary controllers. The supplementary controllers modulate the current order and voltage reference. The HVDC main controller, in comparison to an AC link, provides a high degree of buffering of the two AC sides. However, during a disturbance in the AC segments, the DC power transfer does not remain absolutely constant and is subject to dynamics. HVDC supplementary control can be used to either mitigate the dynamics or to facilitate their transfer between AC segments in a controlled manner.

Modulation of the HVDC link power transfer by a supplementary controller has been used to mitigate the oscillatory modes of AC systems with embedded HVDC links, e.g., in the WECC system [32]. The conventional strategy for HVDC supplementary control is to modulate the rectifier current order and not use the inverter voltage reference modulation in the supplementary control process. However, coordinated DC line power flow modulation through both the rectifier and inverter stations can (i) enhance the modulation effect and (ii) extend its application to cases where contribution from either or both stations is required.

This chapter evaluates the performance of the HVDC supplementary controller to: (1) stabilize the system and (2) minimize the propagation of oscillations from the perturbed segment to other segments or, in a controlled manner, deliberately transfer the

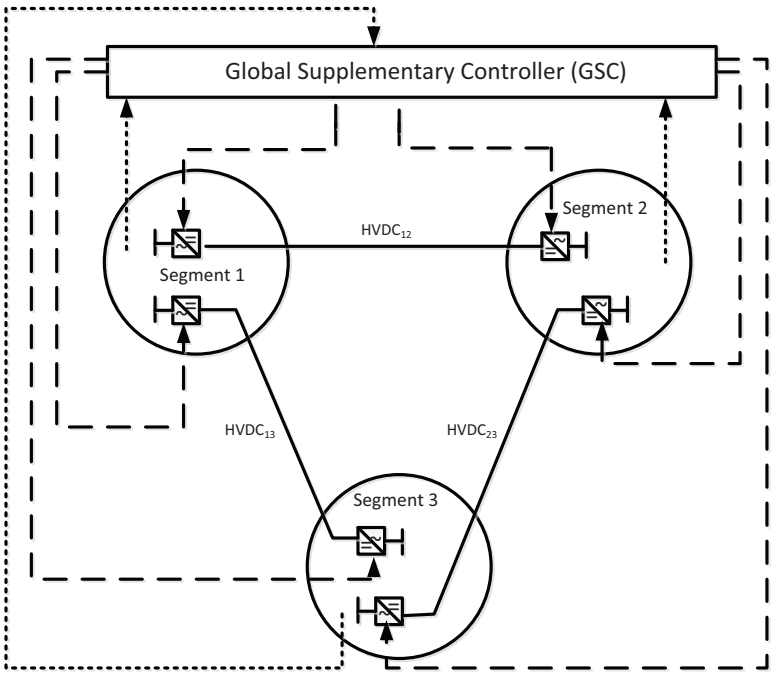

Figure 4.1: Structure of the global supplementary control (GSC)

oscillations, from the perturbed segment to other segments based on (i) rectifier current order modulation, (ii) inverter voltage reference modulation, and (iii) simultaneous rectifier current order and inverter voltage reference modulation. The inverter voltage is usually not modulated to minimize the possibility of commutation failures. To avoid commutation failure, the reported studies in this chapter limit the voltage reference modulation to 3% of its rated value. Provisions are made for the inverter constant extinction angle control to override the voltage control whenever the minimum extinction angle is reached.

Fig. 4.1 illustrates the general structure of the GSC. The coordination center receives signals from all converter stations and converter buses as inputs and uses this information to coordinate the supplementary control of all HVDC links. Two supplementary controllers, which can be applied to the main controllers of the rectifier and/or inverter stations, are considered in this chapter. The main difference between the two controllers is in how perturbations in the inter-segment DC line flows are penalized relative to oscillations in the other system states. The first controller, GSC1, attempts to reduce perturbations in the HVDC line flows by penalizing oscillations in the DC line states. The second controller, GSC2, does not specifically target the HVDC line states; instead, it focuses on limiting the variation in a more complete set of system states. Which controller is more appropriate for use on a given system depends on the overall operating

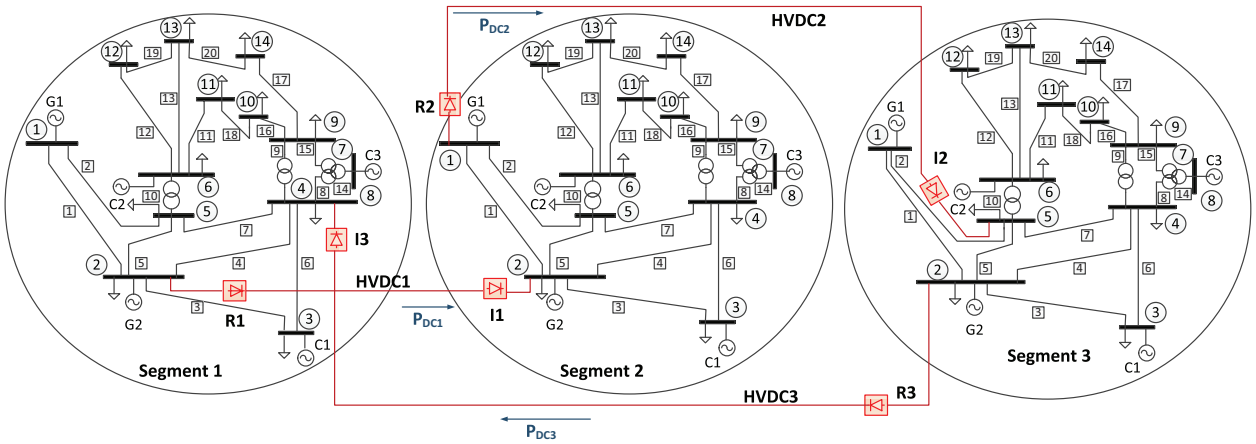

Figure 4.2: Schematic one-line diagram of the fully-DC-segmented test system

goals. If limiting DC line flow variation is of paramount importance—e.g., to ensure that segments remain isolated as much as possible during disturbances—then GSC1 is the appropriate controller to use. On the other hand, GSC2 will tend to use the full range of control capabilities—including intentional modulation of the inter-segment line flows—to stabilize the entire system as quickly as possible. For systems where the fast damping of all AC segments, rather than the isolation of all segments, is of paramount importance, GSC2 will tend to be a better choice than GSC1.

4.2 Study Systems

To study the DC segmentation concept and validate the accuracy of the proposed control schemes for the inter-area HVDC links, the IEEE 14-bus 3-segment system (fully-DC-segmented and partially-DC-segmented configurations) is developed.

The fully-DC-segmented configuration, Fig. 4.2, is composed of three identical segments where each one is a copy of the IEEE 14-bus system. In the 3-segment system, the three segments are connected by three LCC-HVDC links, i.e., HVDC1, HVDC2, and HVDC3. The parameters of the HVDC system are given in [37]. The coefficients of the cost functions for the T-G units of the 3-segment system are given in Table 4.1. The difference between the cost function of the corresponding T-G units from the three segments introduces an imbalance between the conventional optimal power flow (OPF) solution of the segments to include HVDC transactions in the 3-segment study case.

For the sake of comparison, a partially-DC-segmented configuration is also investigated, in which HVDC2 and HVDC3 of the fully-DC-segmented system are replaced by AC lines that result in the same inter-segment power transfers under the equivalent sys-

Table 4.1: Cost function coefficients of the T-G units of the 3-segment system

Segment 1				**Segment 2**				**Segment 3**			
i	c_2^i	c_1^i	c_0^i	i	c_2^i	c_1^i	c_0^i	i	c_2^i	c_1^i	c_0^i
1	0.046	21.6	0	1	0.043	20	0	1	0.043	20	0
2	0.270	21.6	0	2	0.25	20	0	2	0.25	20	0
3	0.011	43.2	0	3	0.01	40	0	3	0.01	40	0
4	0.011	43.2	0	4	0.01	40	0	4	0.01	40	0
5	0.011	43.2	0	5	0.01	40	0	5	0.01	40	0

tem loading conditions (using a standard π transmission line model, this corresponds to setting $R = G = B = 0$ pu and $X = 0.2$ pu).

4.3 Study Results

The reported studies: 1) compare the dynamics of the fully-DC-segmented and partially-DC-segmented configurations, 2) evaluate the performances of GSC1 and GSC2 in the fully-DC-segmented configuration, and 3) investigate the sensitivity of GSC1 and GSC2 in the fully-DC-segmented configuration with respect to variations in the system operating condition and disturbance location. For each case study, prior to a disturbance, the system steady-state operating point is obtained from an AC-DC power flow analysis. A steady-state solution of the fully-DC-segmented configuration is obtained based on the following conditions:

1. HVDC1, HVDC2, and HVDC3 transfer 85%, 53%, and 35.1% of their rated powers.
2. Bus number 1 is the slack bus within each AC segment.
3. The active power and voltage regulation setpoints of all the generators (aside from the slack bus generators) are as specified in the IEEE 14-bus system description.

In all of the reported case studies, the system oscillatory dynamics are excited by a 5-cycle, self-cleared, L-L-L-G fault.

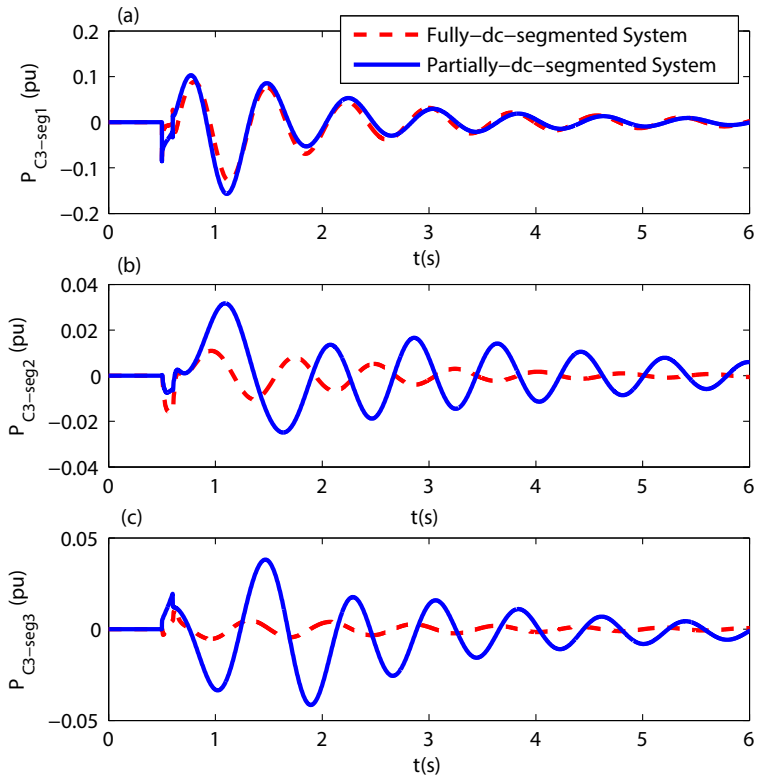

Figure 4.3: Active power deviations of T-G unit C3 in each segment, due to an L-L-L-G fault on bus 10 of segment 1, for the partially- and fully-DC-segmented systems (with no supplementary controller).

4.3.1 Dynamics of the Fully-DC-Segmented and Partially-DC-Segmented Configurations

Fig. 4.3 shows the active power deviations (from the steady-state pre-fault value) of T-G unit C3 in each of the three segments due to a fault. The fault occurs at bus 10 of segment 1 and no HVDC supplementary controller is in service. Figs. 4.3 (b)-(c) show that the impact of the segment 1 disturbance on the other two segments is significantly reduced when the segments are only connected via HVDC links. However, the presence of oscillatory dynamics in segments 2 and 3, even for the fully-DC-segmented case, illustrates that the operation of the HVDC links, based on the primary (CC and CV) controllers, does not provide complete isolation of the segments and segments 2 and 3 experience the impact of the fault in segment 1.

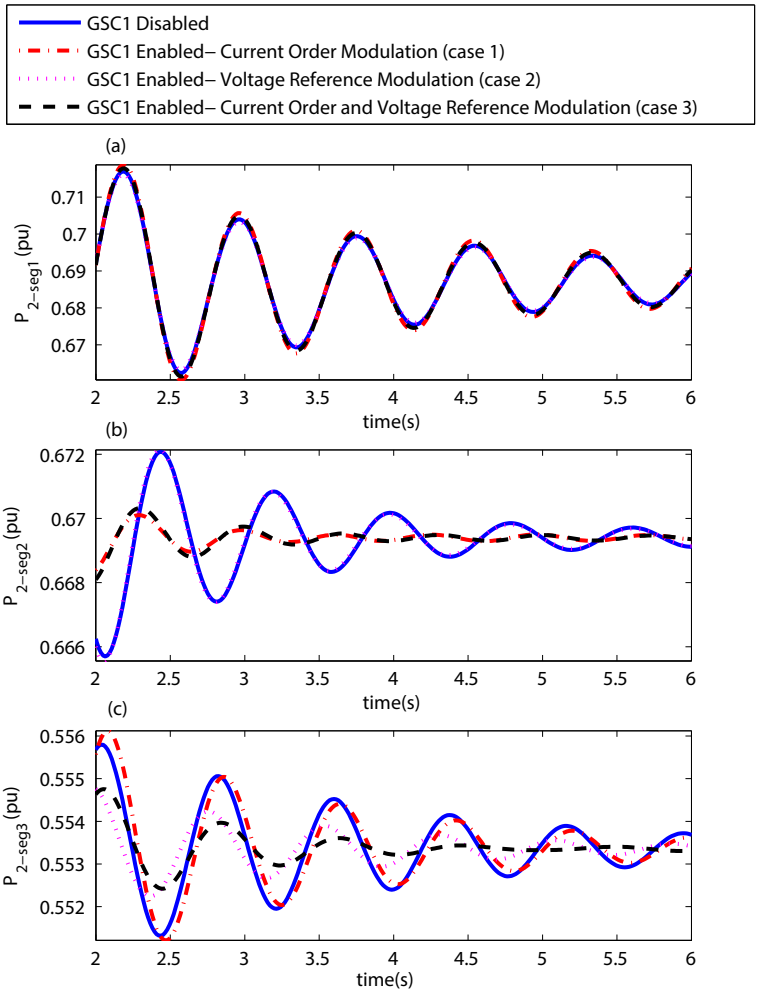

Figure 4.4: Active power deviations of AC transmission line 2 in each segment, due to an L-L-L-G fault on bus 10 of segment 1, with and without GSC1 in service.

4.3.2 GSC1 in the Fully-DC-Segmented System

An often-cited benefit of DC segmentation [11] is that it can partially impede the transfer of disturbances between segments. However, preventing the transfer of oscillatory dynamics of the perturbed segment to the unperturbed segments can have detrimental effects on the system stability. One potential goal of an HVDC supplementary controller is achieving the desired isolation between segments while, at the same time, improving the overall system damping.

GSC1 is intended to (i) ensure system stability and (ii) reduce power oscillatory dynamics in the DC ties, and, as a result, minimize the transfer of oscillatory dynamics from the perturbed segment to the other segments. This is achieved based on one important feature of the LQG-based supplementary controller which enables the control of

targeted states by selecting relatively large weights for those states in the **Q** matrix of (3.3). Based on the selected states, different performance objectives can be achieved. To enable GSC1 to reduce the oscillatory dynamics in the inter-segment HVDC lines, the weights corresponding to the DC line states (rectifier and inverter currents, DC line midpoint voltages, and inverter voltages) are set to unity in the **Q** matrix of (3.3) and the weights corresponding to the rest of the states are set to zero.

Fig. 4.4 shows the active power deviation of AC transmission line 2 within each segment due to the fault on bus 10 of segment 1, with and without GSC1 in service. When GSC1 is in service, the following three HVDC power modulation strategies are examined:

Case 1: Only the rectifier current orders of the three HVDC links are modulated.

Case 2: Only the inverter voltage references of the three HVDC links are modulated.

Case 3: Both the current orders and voltage references of the three HVDC links are modulated.

Fig. 4.4 (a) indicates that the choice of modulation strategy has no noticeable impact on segment 1 (where the fault is initiated); however, Figs. 4.4 (b)-(c) show that the modulation strategy can impact the amplitude of oscillations in segments 2 and 3 and consequently the ability of GSC1 to isolate those segments.

4.3.2.1 Case 1: GSC1 with Current Order Modulation

Figs. 4.4 (b)-(c) show that modulating the rectifier current order, under GSC1, significantly reduces the propagation of the oscillatory dynamics to segment 2 but does not reduce the oscillatory dynamics in segment 3. The reason is that rectifier current modulation can compensate for the AC-side oscillations if the rectifier station of the HVDC link is located in the perturbed segment. Thus, the oscillations excited in segment 1 are prevented from being transferred to the other segment connected to HVDC1 (segment 2), but the oscillations are not prevented in HVDC3 since its rectifier station is in segment 3, not segment 1.

4.3.2.2 Case 2: GSC1 with Voltage Reference Modulation

Fig. 4.4 (c) shows that voltage modulation of the three inverters prevents the propagation of the oscillations to segment 3. The reason is that voltage modulation can compensate for the AC-side oscillations only if the inverter station of the DC link is located in the perturbed segment. Thus, the oscillatory dynamics excited in segment 1 are not

transferred to segment 3. Fig. 4.4 (b) shows the transfer of oscillations is not prevented in HVDC1 since its inverter station is in segment 2, not segment 1.

4.3.2.3 Case 3: GSC1 with Current Order and Voltage Reference Modulation

Figs. 4.4 (b)-(c) show that modulating both the rectifier current orders and inverter voltage references prevents the transfer of oscillations to both adjacent segments, regardless of the rectifier or inverter location. Since the best performance is achieved when modulation is applied to both the current order and voltage reference signals, the remainder of the chapter focuses on this mode of operation for the supplementary controllers.

4.3.3 GSC2 in the Fully-DC-Segmented System

GSC1 improves the isolation between the AC segments, but this may not always be the desired behavior. For example, to take advantage of other segments' damping capabilities, it may be advantageous to deliberately transfer oscillations from one segment to another. Thus, an alternative global supplementary controller (GSC2) is introduced which allows for the transfer of oscillatory dynamics between segments if this can help to improve the overall system response to a disturbance.

To design GSC2, first, the states corresponding to the T-G units with participation factors [1] greater than 0.01 for the significant oscillatory modes (i.e., modes with frequencies less than 2 Hz and damping ratios less than 0.5) are identified. Second, these states are filtered based on how quickly they return to their pre-disturbance steady state values (this is to ensure that states with slower dynamics do not have an undue influence on the feedback gain). The weights corresponding to the states which have not been filtered out are set to unity in the $\mathbf{Q}$ matrix of (3.3), and the weights corresponding to the rest of the states are set to zero.

Fig. 4.5 shows the active power deviation of AC transmission line 2 within each segment due to the fault on bus 10 of segment 1, with GSC2 either in service or disabled. Based on the above analysis for GSC1, only simultaneous modulation of current order and voltage reference is considered. Fig. 4.5 shows that GSC2 does result in the transfer of oscillatory dynamics from segment 1 to segments 2 and 3. This effectively increases the damping in the perturbed segment 1 and decreases the damping in the other segments.

GSC2 can be particularly beneficial if at least one of the segments is able to provide high damping for the oscillations initiated within the faulted segment (e.g., if one of the unperturbed segments is substantially larger than the others). In such a system, the

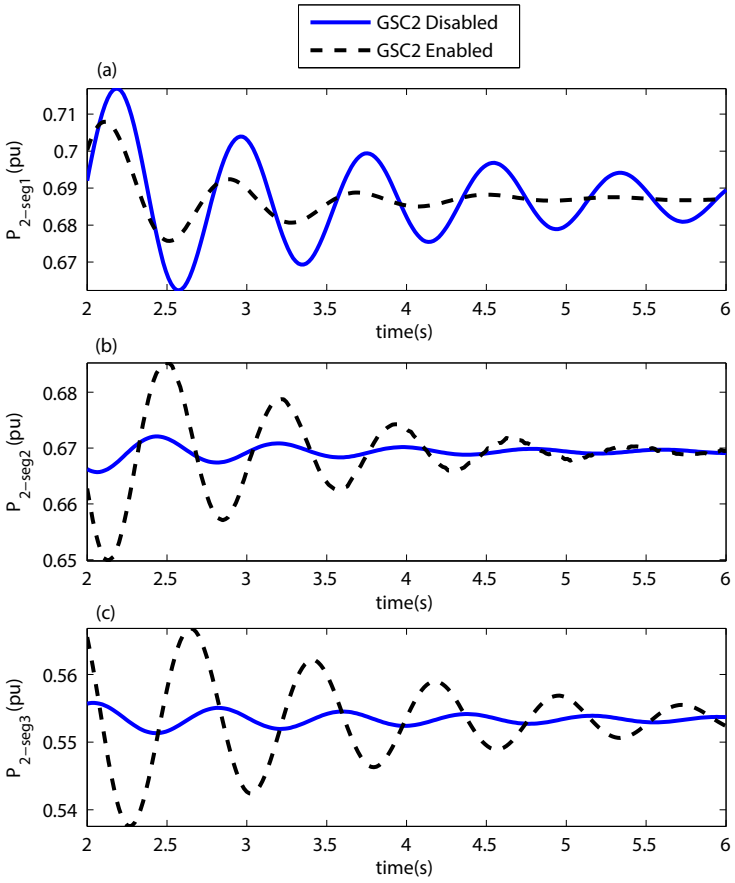

Figure 4.5: Active power deviations of AC transmission line 2, due to an L-L-L-G fault on bus 10 of segment 1, with GSC2 either enabled or disabled

oscillations can be deliberately transferred from the faulted segment to the segment with higher damping, if the goal is to enhance the overall system stability.

An example of such a system can be obtained by modifying the original fully-DC-segmented system, as described in section 4.2, by replacing each T-G unit in segment 2 with two identical T-G units in parallel, each of which delivers half the power of the original T-G unit. In this system (referred to below as the "high inertia" case), the inertia of each equivalent T-G unit in segment 2 is twice that of the corresponding T-G units in segments 1 and 3.

For the high inertia case, the dynamic response to a fault on bus 10 of segment 3 demonstrates how GSC2 can improve the overall system stability. Fig. 4.6 shows the active power deviation of T-G unit G1 in all three segments due to a fault on bus 10 of segment 3 of the high inertia case, with GSC1, GSC2 and no GSC enabled. Fig. 4.6 (c) shows that when GSC2 is not in service, segment 3 becomes unstable. By distributing

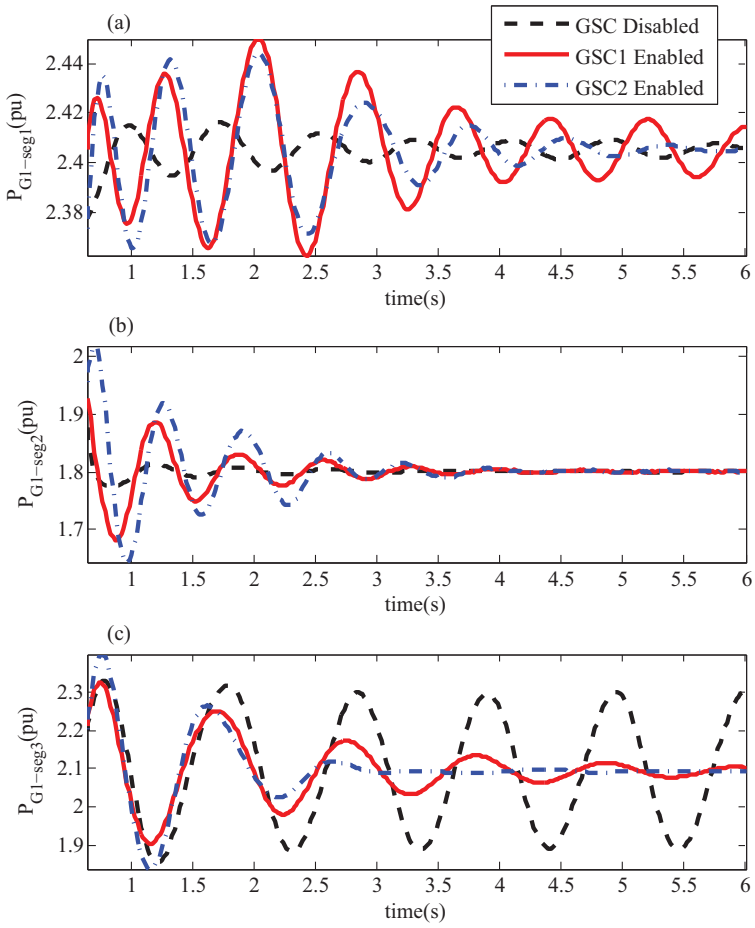

Figure 4.6: Active power deviation of T-G unit G1, due to an L-L-L-G fault on bus 10 of segment 3 of the *high inertia case*, with GSC1, GSC2, and no GSC enabled

the disturbance to segments 1 and 2 (as shown in Figs. 4.6 (a)-(b)) and exploiting the damping of the entire system—particularly the high inertia of segment 2—GSC2 is able to prevent the system from becoming unstable.

4.3.4 Performance Indices and Sensitivity Analyses of the GSC1 and GSC2

For a controller to be usable in practice, its performance should not substantively degrade as the system conditions change. To evaluate the sensitivity of GSC1 and GSC2 performance to system changes, the dynamic response of the fully-DC-segmented system with respect to changes in the system operating point and fault location are investigated.

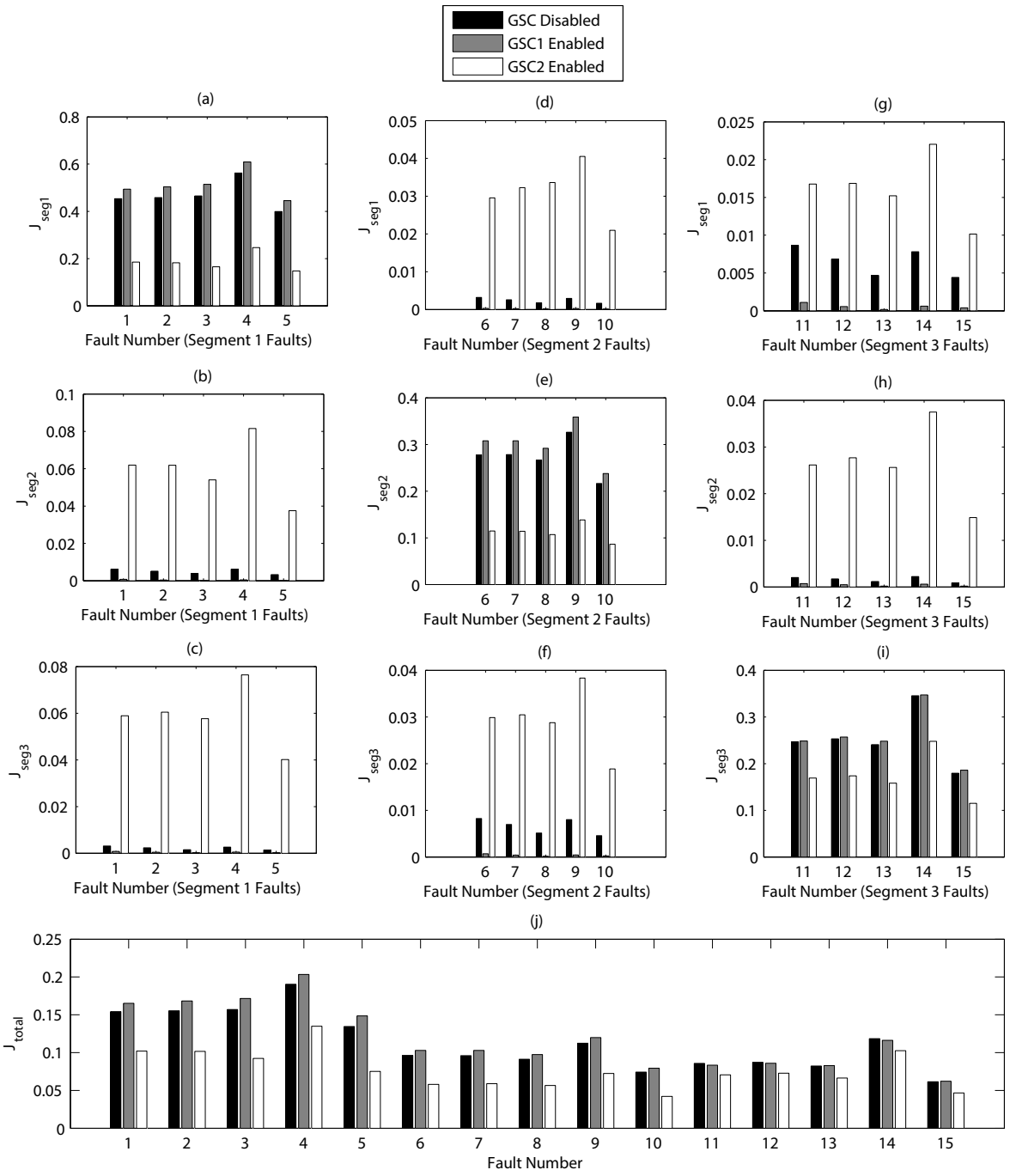

Figure 4.7: Performance of GSC1 and GSC2 as the fault location is varied

This evaluation is based on two performance indices:

$$J_{seg,i} \triangleq \frac{\sum_{l=1}^{k_{seg,i}} \left(\int_{t_1}^{t_2} (y_l(t) - y_{l_{ss}})^2 dt \right)}{k_{seg,i}} \text{ and} \tag{4.1}$$

$$J_{total} \triangleq \frac{\sum_{s=1}^{n_{seg}} k_{seg,s} \times J_{seg,s}}{\sum_{s=1}^{n_{seg}} k_{seg,s}}, \tag{4.2}$$

where $k_{seg,i}$ is the number of AC lines in segment i; y_l and $y_{l_{ss}}$ are, respectively, the per-unit active instantaneous power flow and steady-state power flow of line l; t_1 is one second after the fault inception time instant; and t_2 is the time when the least damped oscillatory power signal reaches 1% of its post-disturbance steady-state value. In (4.1), $y_l(t) - y_{l_{ss}}$ is the deviation of each line power flow from its steady-state value and the integral term is a measure of the energy associated with the oscillations within the line for $t \in [t_1, t_2]$. This energy is summed over all lines and averaged for each segment ($J_{seg,i}$) or the entire system (J_{total}). The net energy associated with the power oscillations of all the lines (J_{total}) or the lines within a particular segment ($J_{seg,i}$) provide a single value that captures how fast the oscillations are damped out in the entire system or within a particular segment. Also, note that this definition is analogous to the state deviation error function used in the LQR design (3.3).

4.3.4.1 Sensitivity to the Fault Location

To evaluate the sensitivity of the GSC to the fault location, the system is subjected to faults 1 to 5, 6 to 10, and 11 to 15, which correspond to faults at buses 10 to 14 of segment 1, 2 and 3, respectively. Fig. 4.7 shows the changes in J_{total} and J_{segi} corresponding to various fault locations for both GSC schemes.

Figs. 4.7 (a)-(c) show that under GSC1 for the faults initiated in segment 1 (faults numbered 1-5), J_{seg1} increases while J_{seg2} and J_{seg3} decrease. This indicates that GSC1 effectively reduces the transfer of the oscillations to the neighboring segments. However, in achieving the improved isolation, the overall system damping does not noticeably improve as indicated by the increase in J_{total} with GSC1 enabled (Fig. 4.7 (j)). For the same fault, GSC2 reduces J_{total}, as shown in Fig. 4.7 (j). The corresponding increases in $J_{seg,2}$ and $J_{seg,3}$ with GSC2 enabled indicate that this improved damping is obtained by distributing the disturbance to the other segments of the system. Faults initiated in segments 2 and 3 follow the same trend as the faults initiated in segment 1 (Figs. 4.7 (d)-(f) and Figs. 4.7 (g)-(i), respectively).

Fig. 4.8 shows the variations of J_{segi} and J_{total} as functions of the fault location for the high inertia case. For the unstable case studies, t_2 of (4.1)-(4.2) is assumed to be the same as the one for the stable case studies. Figs. 4.8 (a), (e) and (i) show that the damping ratio of segment 2 is more than those of segments 1 and 3, since the amplitude of the oscillations caused by a fault in segment 2 is less than those of segments 1 and 3.

For faults in segments 1 and 2, Fig. 4.8 shows similar results as those of Fig. 4.7—GSC1 reduces the oscillations transferred to the unperturbed segments, and GSC2 increases the overall system damping by transferring oscillations to the unperturbed seg-

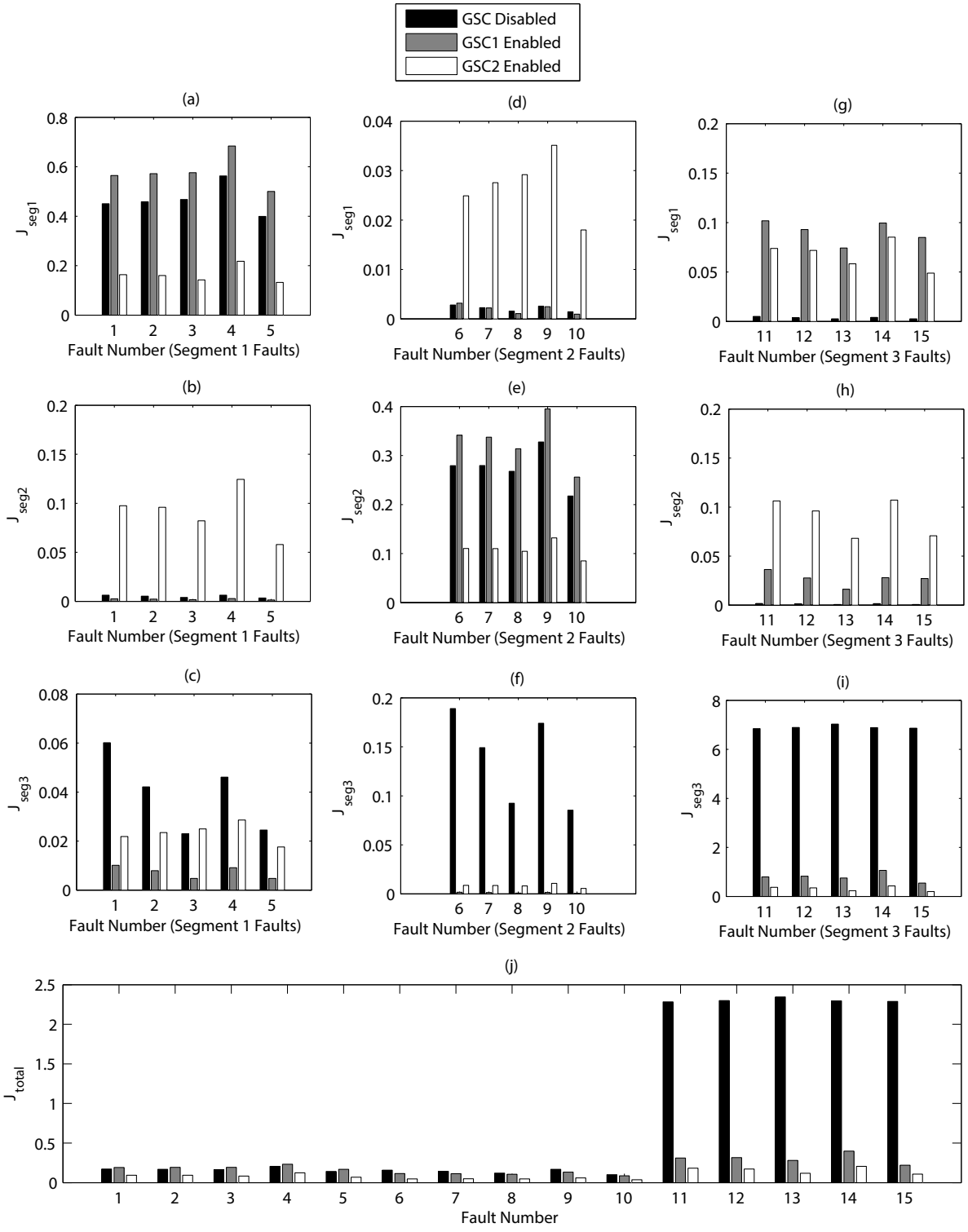

Figure 4.8: Performance of GSC1 and GSC2 as the fault location is varied (high inertia case)

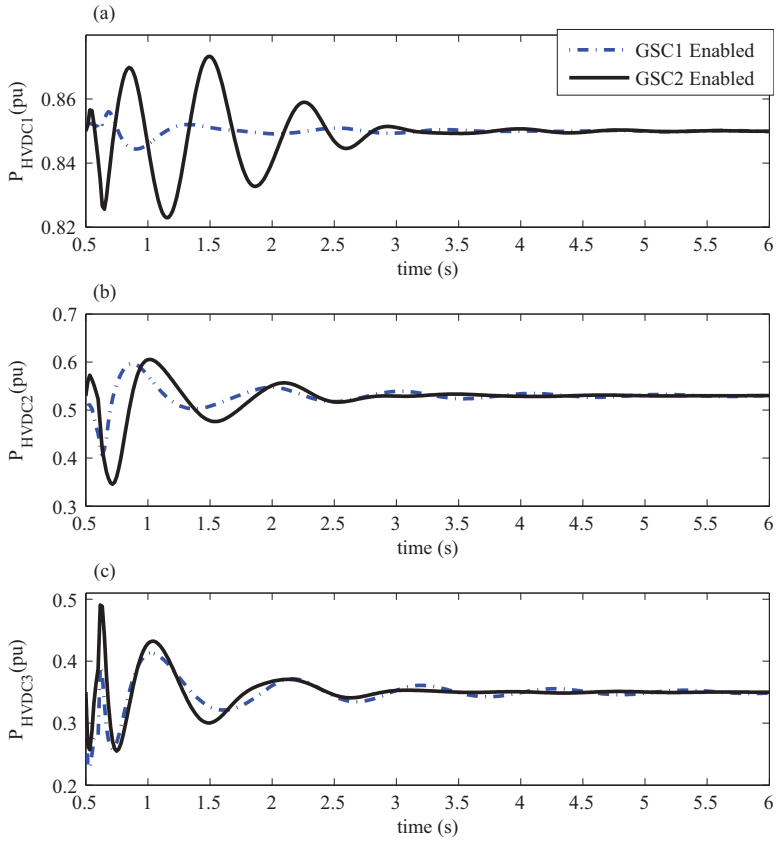

Figure 4.9: Active power transmitted on the HVDC lines due to a fault on bus 10 of segment 3 in the high inertia case, with GSC1 or GSC2 enabled

ments. However, for faults in segment 3, the lack of a supplementary controller results in system instability; this is indicated by the extremely high "GSC Disabled" bars in Figs. 4.8 (h)-(i).

On the other hand, Fig. 4.6 (c) shows that GSC1 and GSC2 both stabilize the system, as designed. Under GSC1, the propagation of oscillatory dynamics to segments 1 and 2 are not fully prevented, since this would result in system instability; instead, deliberate transfer of oscillations occurs to maintain system stability. Under GSC2, oscillations in the system (specifically segment 3 oscillations) are mitigated by transferring the oscillations to the other two segments; as a result, the smallest values of J_{total} are obtained with this operating mode.

To better understand the performance of the controllers for a fault in segment 3, Fig. 4.9 shows the active power transferred through the HVDC lines for a fault on bus 10 of segment 3. This figure shows that, because the system would otherwise be unstable, the first objective of the controllers–to maintain system stability–results in some oscillations being transferred to segments 1 and 2 from segment 3. However, these graphs also show

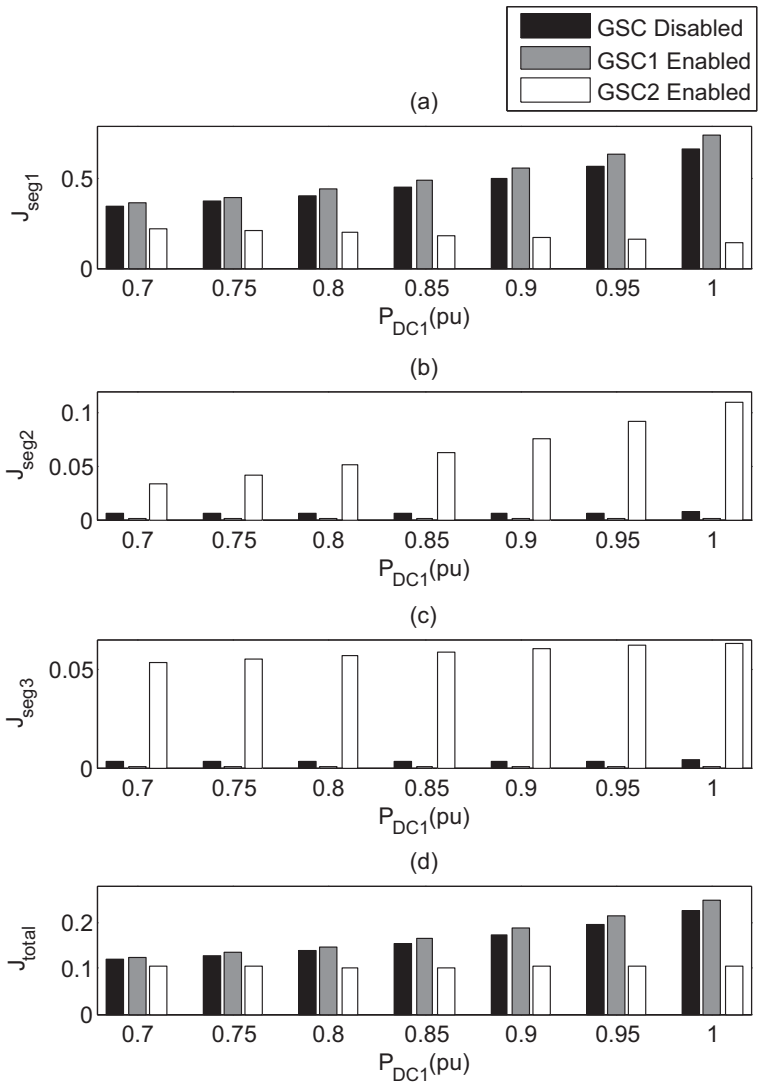

Figure 4.10: Dynamic performance of GSC1 and GSC2 as the HVDC1 operating point is varied from 70% to 100% of its rated value, in steps of 5%.

that, as compared to GSC2, GSC1 does favor control actions that minimize the transfer of oscillations. This behavior is particularly evident in Fig. 4.9 (a), which shows much lower oscillations in HVDC1 when GSC1 is used instead of GSC2.

4.3.4.2 Sensitivity to the Operating Point

To evaluate the sensitivity of GSC1 and GSC2 to changes in the system operating point, the active power flow of HVDC1 is changed from 70% to 100% of the rated value in steps of 5%. Fig. 4.10 shows the sensitivity indices $J_{seg,i}$ and J_{total} for each operating point with the oscillations initiated by an L-L-L-G fault on bus 10 of segment 1. Figs. 4.10 (a)-(c) reveal that under GSC1, for various operating points, $J_{seg,1}$ increases and J_{seg2}

and J_{seg3} decrease, which indicates that isolation among segments improves. Fig. 4.10 (d) shows that, under GSC1, the transfer of oscillatory dynamics to other segments is prevented; as a result, J_{total} does not improve. Fig. 4.10 (d) also shows that under GSC2, for various operating points, J_{total} increases, which indicates that GSC2 is able to improve the overall system damping by the controlled transfer of oscillatory dynamics. Therefore, the desired performance of GSC1 and GSC2 is maintained under the specified range of operating points.

4.4 Conclusions

This chapter presents two HVDC global supplementary control strategies for a DC-segmented AC system—GSC1 and GSC2—designed based on the LQG control method. The controllers are designed to (i) improve the system stability and either

(ii-a) minimize the transfer of oscillations between segments (GSC1) *or*

(ii-b) allow for the controlled transfer of oscillations to further reduce system-wide oscillations (GSC2).

Simulation results obtained by applying these controllers to a 3-segment AC system show that: (i) DC segmentation can effectively minimize the inter-segment transfer of disturbances due to a fault, (ii) both GSC1 and GSC2 are able to initiate stabilizing action, (iii) as compared with GSC1 or the lack of any supplementary controller, GSC2 improves the overall system damping by spreading the disturbance to adjacent segments in a controlled manner, (iv) as compared to GSC2 and the lack of any supplementary controller, GSC1 effectively isolates the segments from one another during a disturbance, and (v) the performances of GSC1 and GSC2 meet the desired objectives under various operating conditions and fault locations.

Chapter 5

Dynamic Stability Enhancement of a DC-Segmented AC Power System via HVDC Operating-Point Adjustment

5.1 Introduction

A number of reported studies discuss various operating point tuning strategies to increase the stability margin and mitigate low frequency oscillations of the power system [62–70]. The studies are based on (i) voltage control of synchronous machines [62], [63], (ii) reactive power control [63–66], (iii) active power control [63, 67, 68, 71], and (iv) imposition of stability constraints associated with the Hopf bifurcation to the conventional optimal power flow (OPF) problem [69, 70]. None of the reported strategies use the HVDC set-points adjustment to achieve stability improvements.

Methods relying on reactive power control require the presence of controllable reactive power loads or FACTS controllers, which may not be available. Methods based on active power control (generation redispatch) impose challenging issues for real-time applications, since most generators are not on automatic generation control and can take up to several minutes to respond to redispatch instructions [72]. Furthermore, the reported methods of [63, 67, 68, 71] require both positive and negative sensitivities, which are not always available, to ensure active and reactive power balance is maintained.

The higher degree of controllability of the HVDC link power flow, as compared with that of an AC line, can be used to adjust the operating point of a DC-segmented AC

system to move the real part of the critical eigenvalues (corresponding to the oscillatory modes with the least damping ratio) further away from the imaginary axis and thus increase the stability margin and damping ratios of the oscillatory modes. The central idea of this chapter is to determine the optimum set-point value of the HVDC links such that a sufficiently large margin to the Hopf point and a high damping ratio is ensured. Hopf bifurcation theory is used to derive a strategy to control the power flow of the HVDC links to change the system operating point.

Changing the DC active power set-points indirectly results in the redispatch of the generators' active and reactive power outputs based on their governor and exciter controllers, respectively. This is in contrast to prior methods [63,67–71], which rely on direct control of the generators. The proposed approach allows for a more rapid response to real-time events such as line outages, since the generators automatically redispatch based on their active and reactive power controllers. The reported studies in this chapter show that the optimal HVDC set-points can be used to (i) temporarily restabilize the system subjected to a fault or (ii) preemptively increase the system robustness to faults and changes in the loading factor.

5.2 Hopf Sensitivity Calculations [71, 73, 74]

The power system model for the envisioned studies is of the form

$$\begin{bmatrix} \dot{\mathbf{x}} \\ \mathbf{0} \end{bmatrix} = \begin{bmatrix} \mathbf{f}(\mathbf{x}, \mathbf{y}, \boldsymbol{\lambda}) \\ \mathbf{g}(\mathbf{x}, \mathbf{y}, \boldsymbol{\lambda}) \end{bmatrix} = \mathbf{F}(\mathbf{z}, \boldsymbol{\lambda}), \tag{5.1}$$

where $\mathbf{x} \in \Re^{n_x}$, $\mathbf{y} \in \Re^{n_y}$, and $\boldsymbol{\lambda} \in \Re^{m}$ are the dynamic state variable, algebraic variable and parameter vectors, respectively. $\dot{\mathbf{x}} = \mathbf{f}(\mathbf{x}, \mathbf{y}, \boldsymbol{\lambda})$ and $\mathbf{0} = \mathbf{g}(\mathbf{x}, \mathbf{y}, \boldsymbol{\lambda})$ ($\mathbf{f} : \Re^{n_x+n_y+m} \rightarrow \Re^{n_x}$ and $\mathbf{g} : \Re^{n_x+n_y+m} \rightarrow \Re^{n_y}$) represent the differential and algebraic equations, respectively. In (5.1), $\mathbf{F} = [\mathbf{f}^T, \mathbf{g}^T]^T, \mathbf{F} : \Re^{n_z+m} \rightarrow \Re^{n_z}, n_z = n_x + n_y$, $\mathbf{z} \triangleq [\mathbf{x}^T, \mathbf{y}^T]^T$ and $\mathbf{F}(\mathbf{z}_0, \boldsymbol{\lambda}_0) = \mathbf{0}$ defines an equilibrium $(\mathbf{z}_0, \boldsymbol{\lambda}_0)$ of the system.

A bifurcation occurs when a small change in a parameter (the bifurcation parameter) causes a sudden change in the behaviour of the system. Based on the system dynamic manifolds and equilibrium points, bifurcations can be local or global. This chapter focuses on the study of local bifurcations, in particular Hopf bifurcations, which can be identified by the eigenvalues of the linearized system DAEs. In a Hopf bifurcation, a complex pair of eigenvalues crosses the imaginary axis of the complex plane as the system parameters gradually change.

The system parameters vector $\boldsymbol{\lambda} = [\mu, \mathbf{p}]$ represents the non-controllable parameter μ, e.g., the system loading, and the set of controllable (design) parameters $\mathbf{p}$, e.g., HVDC set-points. When a non-controllable parameter increases in a direction of stress from μ_0 with the controllable parameters fixed at $\mathbf{p}_0$, the system reaches a Hopf bifurcation point for the non-controllable parameter value μ^*[1] when the real part of a single pair of complex eigenvalues becomes zero (beyond this point, the system is no longer small-signal stable). The stability margin, defined as $M \triangleq \mu^* - \mu_0$, can often be increased by controlling $\mathbf{p}$ using the first order sensitivity of M with respect to $\mathbf{p}$. The sensitivity of M also identifies those parameters that strongly affect the stability margin.

The Hopf bifurcation hypersurface, Σ^{Hopf}, consists of the set $\boldsymbol{\lambda}^*$ for which (5.1) has a Hopf bifurcation at $(\mathbf{z}_0^*, \boldsymbol{\lambda}^*)$ (i.e., where $\mathbf{F}_\mathbf{z}^*$, the Jacobian of $\mathbf{F}$ with respect to $\mathbf{z}$ evaluated at the Hopf point, has a single pair of complex eigenvalues with no real component and all other eigenvalues have strictly negative real parts). To evaluate $\mathbf{F}_\mathbf{z}$ at the Hopf point, first the power flow equations are solved. Second, based on the power flow solution, the equilibrium point of the dynamic model at the Hopf point, $\mathbf{z}_0^*$, is determined and then $\mathbf{F}_\mathbf{z}$ is evaluated at $\mathbf{z}_0^*$.

Since $\mathbf{F}_\mathbf{z}^*$ is invertible [73], the implicit function theorem implies that there is a function $\mathbf{u} : \Re^m \rightarrow \Re^{n_z}$ in the neighborhood of $\boldsymbol{\lambda}^*$ which maps system parameters to the position of the equilibrium and its $n_z \times m$ Jacobian $\mathbf{u}_{\boldsymbol{\lambda}}$ is obtained from the solution of

$$\mathbf{F}_\mathbf{z}\mathbf{u}_{\boldsymbol{\lambda}} = -\mathbf{F}_{\boldsymbol{\lambda}}, \tag{5.2}$$

where $\mathbf{F}_{\boldsymbol{\lambda}}$ is the Jacobian of $\mathbf{F}$ with respect to $\boldsymbol{\lambda}$. The sensitivity of M with respect to $\mathbf{p}$ is a scaled projection of a normal vector to Σ^{Hopf}. The normal vector to Σ^{Hopf} can be determined by the sensitivities of the real parts of the eigenvalues with respect to the parameters by

$$\mathbf{N} = \mathbf{Re}\{\mathbf{d}\,(\mathbf{F}_{\mathbf{zz}}^*\mathbf{u}_{\boldsymbol{\lambda}}^* + \mathbf{F}_{\mathbf{z}\boldsymbol{\lambda}}^*)\,\mathbf{e}\}, \tag{5.3}$$

where $\mathbf{F}_{\mathbf{zz}}$, an $n_z \times n_z \times n_z$ tensor, is the Hessian of $\mathbf{F}$ with respect to $\mathbf{z}$ and $\mathbf{F}_{\mathbf{z}\boldsymbol{\lambda}}$, an $n_z \times n_z \times m$ tensor, is the Hessian of $\mathbf{F}$ with respect to $\mathbf{z}$ and $\boldsymbol{\lambda}$. $\mathbf{d}$ and $\mathbf{e}$ are the normalized extended right and left eigenvectors of $\mathbf{F}_\mathbf{z}$ corresponding to $j\omega^*$ such that $\mathbf{de} = 1$ and $|\mathbf{d}| = 1$. $\mathbf{d}$ and $\mathbf{e}$ are determined by solving the generalized eigenproblem [74]. Furthermore, if

$$\mathbf{N} = [n_\mu, n_{p_1}, n_{p_2}, ..., n_{p_{(m-1)}}], \tag{5.4}$$

[1] All the parameters and variables at a Hopf point are identified by the superscript $*$.

then

$$\mathbf{M}_{\mathbf{p}|\mathbf{p}_0} = -(n_\mu)^{-1}[n_{p1}, n_{p2}, ..., n_{p_{(m-1)}}], \tag{5.5}$$

where $\mathbf{M}_{\mathbf{p}|\mathbf{p}_0}$ is the sensitivity of the stability margin with respect to the controllable parameters. An example illustrating the procedure for calculating the sensitivity of the stability margin with respect to the design parameters is given in Appendix C.

5.3 Optimization Formulation

The objective of this study is to control the active power flows of the HVDC links of the study systems of Fig. 5.2 and Fig. 5.3 to increase the stability margin subject to system constraints. Thus, the active power set-points of the HVDC links are considered as the controllable parameters $\mathbf{p}$. Since $\mathbf{M}_{\mathbf{p}|\mathbf{p}_0}$ is a scaled projection of $\mathbf{N}$, movement away from the Hopf surface implies an increase in the stability margin and damping ratio of the oscillatory modes. In the optimization process (see below), the damping ratio is easier to calculate compared to the stability margin and increasing the damping ratio will tend to increase the stability margin. Thus, to improve the stability margin, the objective is to maximize the damping ratio of the least damped mode.

The optimum operating point of the HVDC system, which results in the highest damping ratio of the oscillatory dynamics, is obtained from the following optimization problem:

$$\max_{\mathbf{p_{DC}}} \zeta_{min}(\mathbf{x}, \mathbf{y}, \boldsymbol{\lambda}), \tag{5.6}$$

$$\text{s.t.} \qquad \mathbf{g}(\mathbf{x}, \mathbf{y}, \boldsymbol{\lambda}) = 0, \tag{5.7}$$

$$\mathbf{f}(\mathbf{x}, \mathbf{y}, \boldsymbol{\lambda}) = 0, \tag{5.8}$$

$$\mathbf{h}^{min} \leq \mathbf{h}(\mathbf{x}, \mathbf{y}, \boldsymbol{\lambda}) \leq \mathbf{h}^{max}, \tag{5.9}$$

where

$$\zeta_{min} = \min_{j \in \{1, ...n_{mode}\}} \zeta_j, \tag{5.10}$$

$$\lambda = [\mu, \mathbf{p}_{DC}], \tag{5.11}$$

and $\mathbf{p}_{DC}$ and n_{mode} are the vector of DC link active powers and the number of oscillatory modes, respectively. The objective is to determine the optimum active power set-points of the DC links to obtain the maximum damping ratio of the least damped oscillatory modes. The equality constraints (5.7)-(5.8) ensure the system is in steady-state. The inequality constraints (5.9) consist of the limits on the DC link power injections.

A flowchart of the optimization process is shown in Fig. 5.1. In this process, the initial operating point is assumed to be the solution of the conventional, cost-minimizing OPF problem. At this operating point, the selected non-controllable parameter (e.g., a load scaling factor) is varied until the system encounters a Hopf bifurcation, where the damping ratio of the least damped mode, ζ^0_{min}, is zero. Then, at the Hopf point, the sensitivities of the real parts of the critical eigenvalues with respect to the active power flow set-points of the HVDC links are determined. Finally, a line search is carried out to identify the optimum controllable parameters:

$$\tilde{P}_{DCi}(\alpha_{opt}) = P^{(0)}_{DCi} + \alpha_{opt} m_{P_{DCi}}$$

$$P^{opt}_{DCi} = \begin{cases} P^{min}_{DCi} & \text{if } \tilde{P}_{DCi} < P^{min}_{DCi} \\ \tilde{P}_{DCi}(\alpha_{opt}) & \text{if } P^{min}_{DCi} \leq \tilde{P}_{DCi}(\alpha_{opt}) \leq P^{max}_{DCi} \\ P^{max}_{DCi} & \text{if } \tilde{P}_{DCi}(\alpha_{opt}) > P^{max}_{DCi} \end{cases} \tag{5.12}$$

where $m_{P_{DCi}}$, α_{opt}, P^{opt}_{DCi} and $P^{(0)}_{DCi}$ are the sensitivity of the stability margin with respect to P_{DCi}, optimum step size, and the optimum and initial flows of the i^{th} HVDC link, respectively. For the line search, first, the maximum and minimum values of the step size, α_{max} and α_{min}, are determined based on $m_{P_{DCi}}$ and the limits of the active power set-points of the DC links, i.e., $\mathbf{p_{DC}}^{max}$ and $\mathbf{p_{DC}}^{min}$. Next, K equally-spaced points in the $[\alpha_{min}\ \alpha_{max}]$ interval are tested. During the line search process the governor-based power flow (GBPF) [75], in which the generators' output levels depend on the droop characteristics, is solved after each update to the DC set-points. In the GBPF problem, (i) the net DC load of each segment, defined as the difference between the DC powers injected to and absorbed from the neighboring segments, is determined, (ii) the change in the net DC load from the initial solution is calculated, and (iii) in each segment, the change in the output of each T-G unit is determined by its droop characteristic. The system model is linearized at the operating point obtained from the GBPF solution and then used to calculate the damping ratios of the oscillatory modes and evaluate the objective function (5.6).

5.4 Study Systems

To study the HVDC control operating point tuning scheme the IEEE 14-bus 3-segment system, Fig. 5.3, and 2-segment system, Fig. 5.2, are used. The 3-segment system is a more general case study compared to the 2-segment system; however, for illustrative

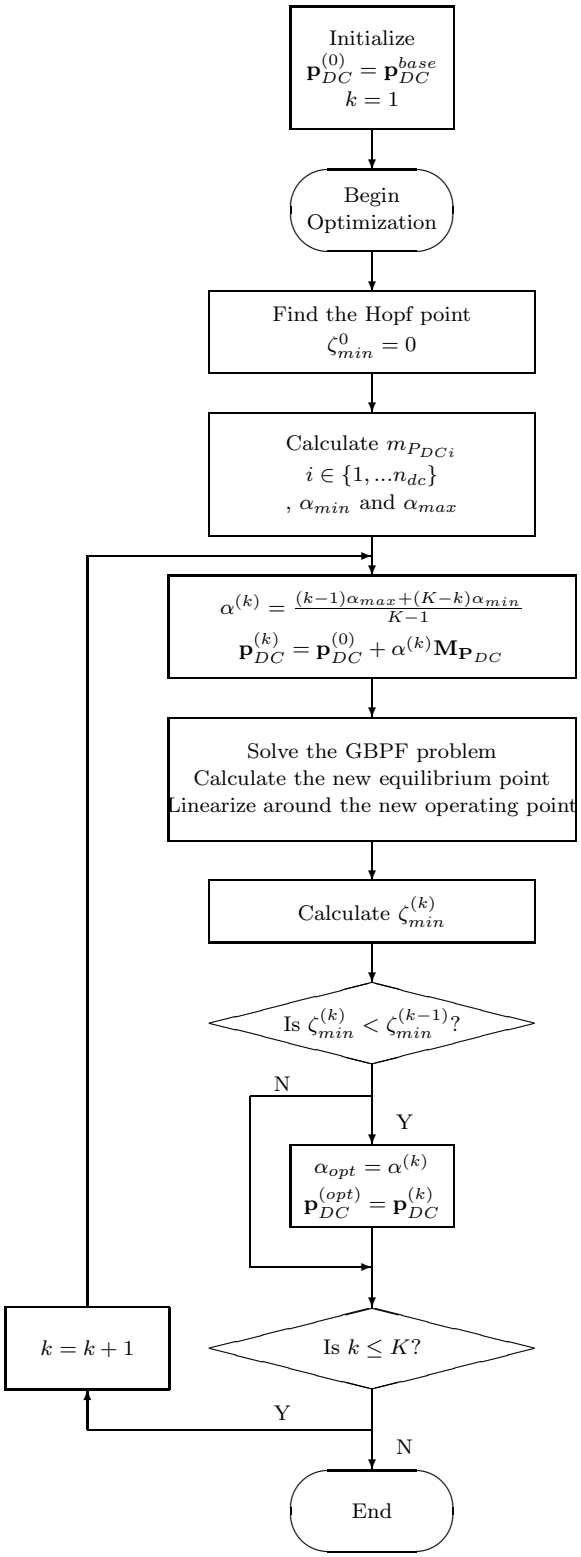

Figure 5.1: Optimization flowchart

purposes, the 2-segment case study is also considered.

The 2-segment system is composed of two identical segments where each one is a

Table 5.1: Cost function coefficients of the T-G units of the 2-segment system

Segment 1				**Segment 2**			
i	c_2^i	c_1^i	c_0^i	i	c_2^i	c_1^i	c_0^i
1	0.0645	30	0	1	0.043	20	0
2	0.375	30	0	2	0.25	20	0
3	0.015	60	0	3	0.01	40	0
4	0.015	60	0	4	0.01	40	0
5	0.015	60	0	5	0.01	40	0

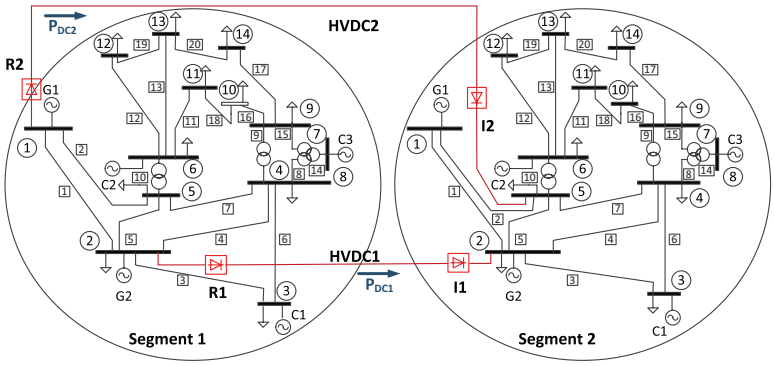

Figure 5.2: Schematic one-line diagram of the 2-segment system

copy of the IEEE 14-bus system. The segments are connected by two LCC HVDC links, i.e., HVDC1 and HVDC2. The rectifier (R) and inverter (I) stations of the HVDC links are also identified on Fig. 5.2. The cost coefficients for the T-G units of the 2-segment system are given in Table 5.1.

5.5 Study Results

In this section, two case studies in the MATLAB/Simulink environment are reported. The stability margin and eigenvalue plot of each test system operating at the optimum point are compared with those of the system at the operating point obtained from the conventional, cost-minimizing OPF solution. Hereafter, the conventional OPF solution,

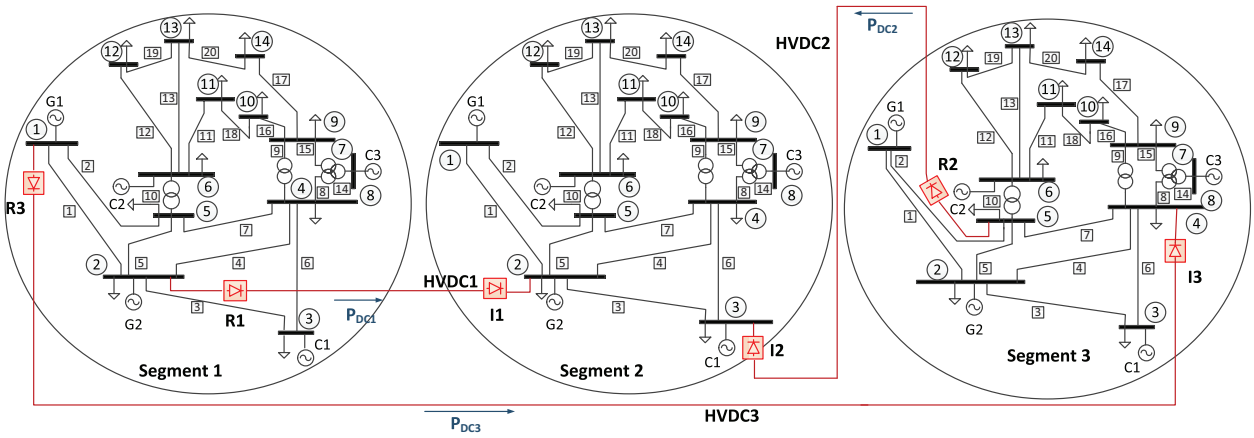

Figure 5.3: Schematic one-line diagram of the fully-DC-segmented test system

without any stability constraints, is referred to as the "base OPF" solution.

5.5.1 Case Study on the 2-Segment System

It is assumed that the HVDC lines of Fig. 5.2 are lossless, i.e., $P_{rec} = -P_{inv}$; therefore, there are only two controllable parameters, P_{DC1} and P_{DC2} (within the range [-1,1] pu). All loads in the system are varied with respect to the base values $\mathbf{p_{L0}}$ and $\mathbf{q_{L0}}$ as

$$\mathbf{p_L} = \mathbf{p_{L0}} \times (1 + \beta), \tag{5.13}$$

$$\mathbf{q_L} = \mathbf{q_{L0}} \times (1 + \beta), \tag{5.14}$$

where β is the loading factor. The initial active power set-points of the HVDC links are $P_{DC1} = -0.90$ pu and $P_{DC2} = -0.74$ pu. At the initial operating point all the system eigenvalues have negative real parts and the system is stable. When β is increased from 0 to 1.0 for the loads in segment 2 (the system operating point is obtained from the GBPF solution), the system encounters a Hopf bifurcation at $\beta^* = 1.0$.

To stabilize the system, first, the sensitivity vector of the real parts of the critical eigenvalues to P_{DC1} and P_{DC2} at the Hopf point is calculated. The sensitivity vector, $[m_{P_{DC1}}, m_{P_{DC2}}] = [11.11, 11.25]$, shows that to increase the damping ratio of the oscillatory modes, the flows of HVDC1 and HVDC2 should be increased in the positive direction. Second, knowing the sensitivity vector, a line search is used to calculate the optimum changes to P_{DC1} and P_{DC2}. In this case study, $\mathbf{P}_{DC}^{opt} = [1, 1]$ pu.

To demonstrate the effectiveness of the proposed method, the real part of the closest oscillatory eigenvalue to the imaginary axis, as a function of P_{DC1} and P_{DC2}, is shown in Fig. 5.4. Fig. 5.4 shows that the proposed method is able to determine the HVDC

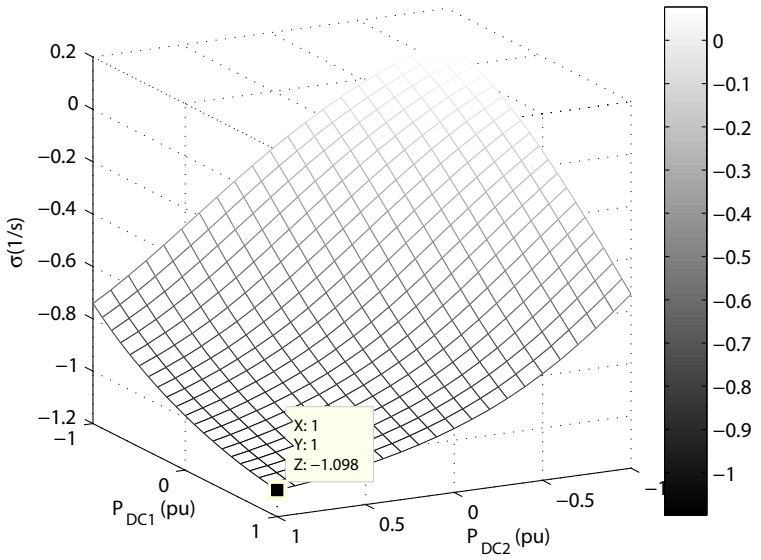

Figure 5.4: Real part of the closest eigenvalue to the imaginary axis versus the flows of HVDC links

set-points that achieve the highest damping of the system. It should be noted that since the frequency of the critical mode does not noticeably change with the operating point, the real part of the eigenvalue associated with the critical mode is an appropriate representative of the damping ratio.

Fig. 5.5 shows the system eigenvalues associated with the oscillatory modes with frequencies less than 2 Hz and damping ratios less than 0.5 when $\beta^* = 1.0$. When the system operates at the base OPF solution, the system is at the Hopf bifurcation. However, after the HVDC set-points are adjusted, the real part of the closest oscillatory eigenvalue to the imaginary axis is -1.1.

The trade-off between the increased generation cost and increased damping ratio is illustrated in Fig. 5.6. Fig. 5.6 (a) shows the real part of the closest oscillatory eigenvalue to the imaginary axis with respect to α. Fig. 5.6 (a) illustrates that the solution obtained from the optimization problem (moving in the direction of the sensitivity vector) results in an increase in the damping ratio of the oscillatory modes ($\alpha_{opt} = 0.17$). However, this increase in the damping is accompanied by an increase in the generation cost due to changes in the generators' output levels, as shown in Fig. 5.6 (b) (note: the generation costs in this figure are normalized with respect to the cost obtained from the base OPF solution).

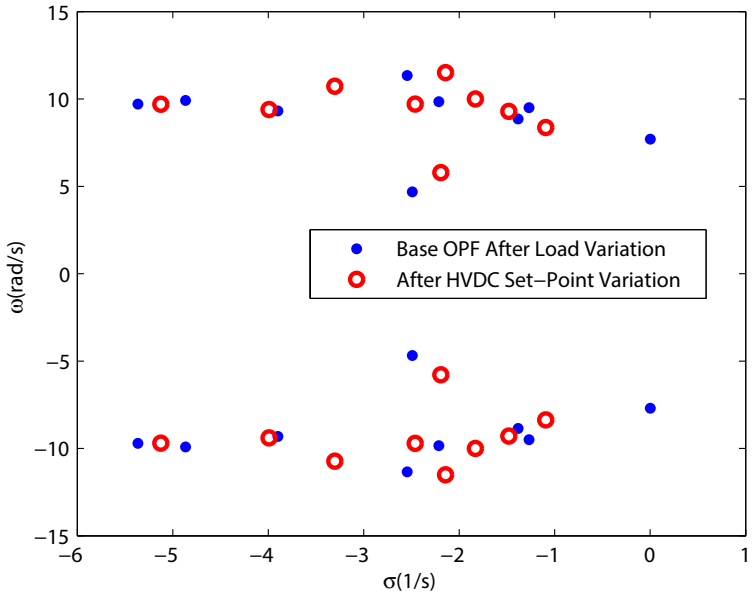

Figure 5.5: Eigenvalues plot of the system corresponding to the two operating points obtained from the base OPF and optimization problem

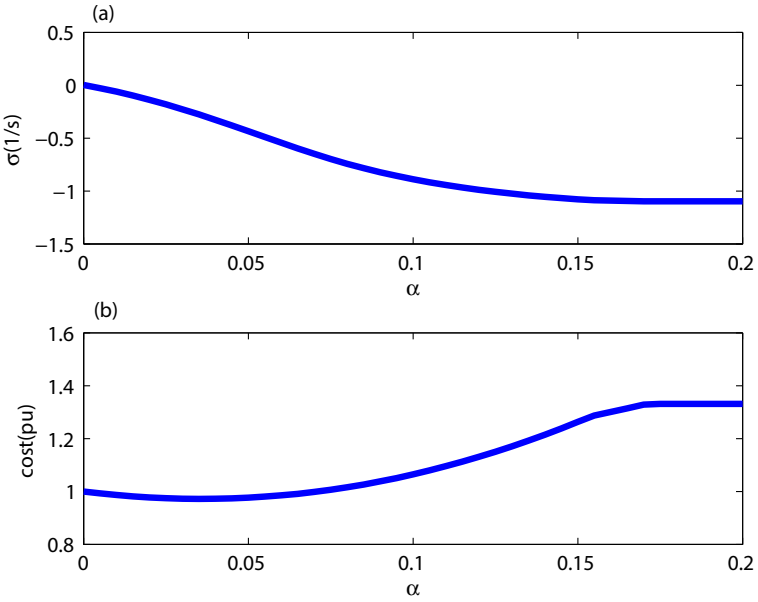

Figure 5.6: Generation cost and σ versus the optimization step size

5.5.2 Case Studies on the 3-Segment System

The controllable parameters in this case study are P_{DC1}, P_{DC2} and P_{DC3}. The system is forced to Hopf bifurcation due to either load variations (case 1) or line impedance changes (case 2). At the Hopf bifurcation point, the sensitivity of the real parts of the critical eigenvalues with respect to the controllable parameters is calculated and, using

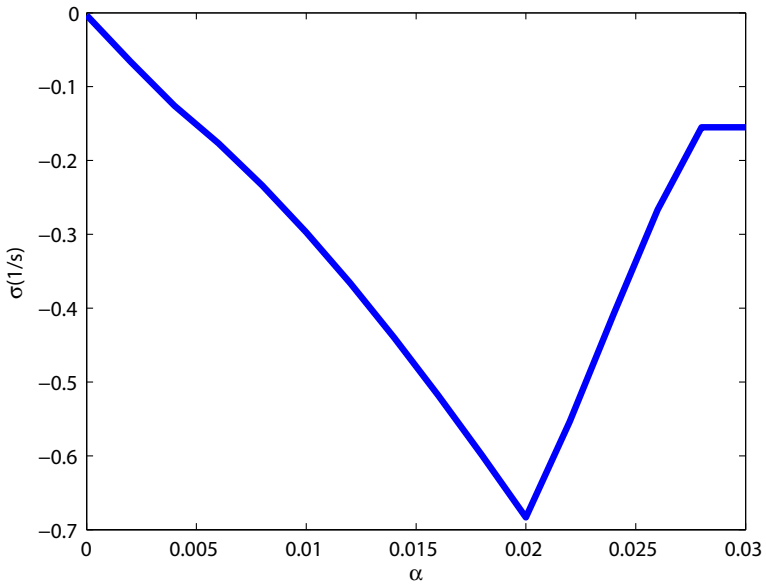

Figure 5.7: σ versus the optimization step size

the sensitivity information, the HVDC flows are adjusted to move the eigenvalues away from the imaginary axis.

5.5.2.1 Case 1: Load Variations

Using generator and HVDC set-points determined from the standard OPF, increasing β for the loads in segment 3 from 0 to 1.9 leads the system to a Hopf bifurcation. At the Hopf point, $\mathbf{P}_{DC}^{(0)} = [-0.72, -1, -0.80]$ pu and the sensitivities of the real parts of the critical eigenvalues with respect to the controllable parameters are $[m_{P_{DC1}}, m_{P_{DC2}}, m_{P_{DC3}}] = [0, 72.31, -70.89]$. Based on the optimum direction, the optimum step size is calculated ($\alpha_{opt} = 0.02$) and $\mathbf{P}_{DC}^{opt} = [-0.72, 0.45, -1]$ pu. If the HVDC links transfer the optimum flows, the real part of the closest oscillatory eigenvalue to the imaginary axis is less than -0.68. Fig. 5.7 shows the real part of the closest oscillatory eigenvalues to the imaginary axis with respect to α, and illustrates that the solution obtained from the optimization problem results in an increase in the damping ratios of the oscillatory modes.

Fig. 5.8 shows the system eigenvalues associated with the oscillatory modes with frequencies less than 2 Hz and damping ratios less than 0.3. When the system operates at the base OPF solution, all the eigenvalues are on the left side of the imaginary axis. When the load is increased, the eigenvalues move toward the imaginary axis until the system encounters a Hopf bifurcation. Based on the HVDC set-point adjustment, the oscillatory modes move away from the imaginary axis and the damping ratios of the

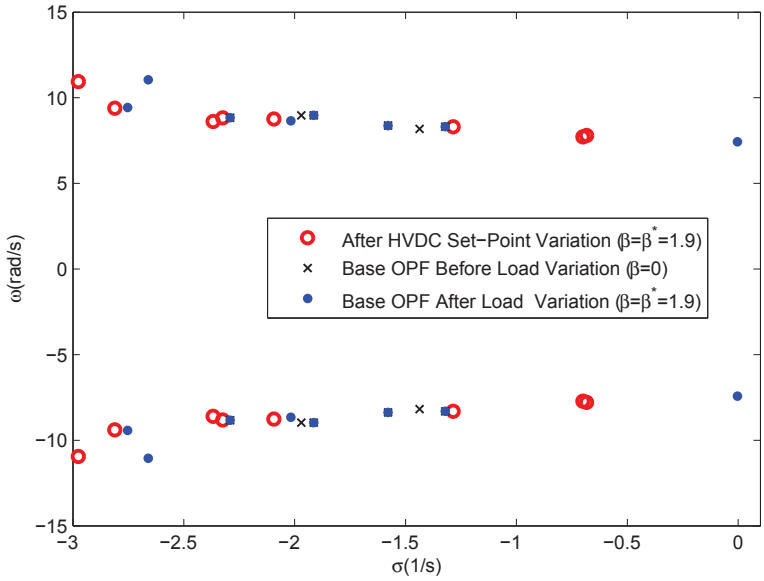

Figure 5.8: Eigenvalues plot of the system corresponding to three operating points obtained from the optimization problem, and base OPF solution after and before load variation

oscillatory modes increase.

5.5.2.2 Case 2: Line Impedance Change

The effects of changes in transmission system impedance on system stability have been reported in the technical literature [76]. In this section, the effect of such changes (rather than load scaling, as in case 1) on the system stability is studied and the application of the proposed operating point tuning method to stabilize the system, subsequent to a line outage, is demonstrated. In this case study β for loads in segments 1, 2 and 3 are 0, 0, and 0.6, respectively. To represent the line outage impact, the impedance of line 3 within each segment is increased to 100 times the nominal value. To stabilize the system due to the line outage, the sensitivity of the stability margin with respect to the set-points of the HVDCs is calculated and then, based on a line search, the optimum operating point is determined.

Fig. 5.9 shows the loci of the two least damped eigenvalues (mode 1 and 2 have the least damping as the line opens) for various line impedances at the base OPF solution and demonstrates that as the line impedance increases the system stability decreases (at the Hopf point, mode 1 crosses the imaginary axis). The eigenvalues at the Hopf point and the line outage are identified on Fig. 5.9. Fig. 5.9 also shows that the system stability improves as the DC flows are changed in the direction of the sensitivity. The loci of the

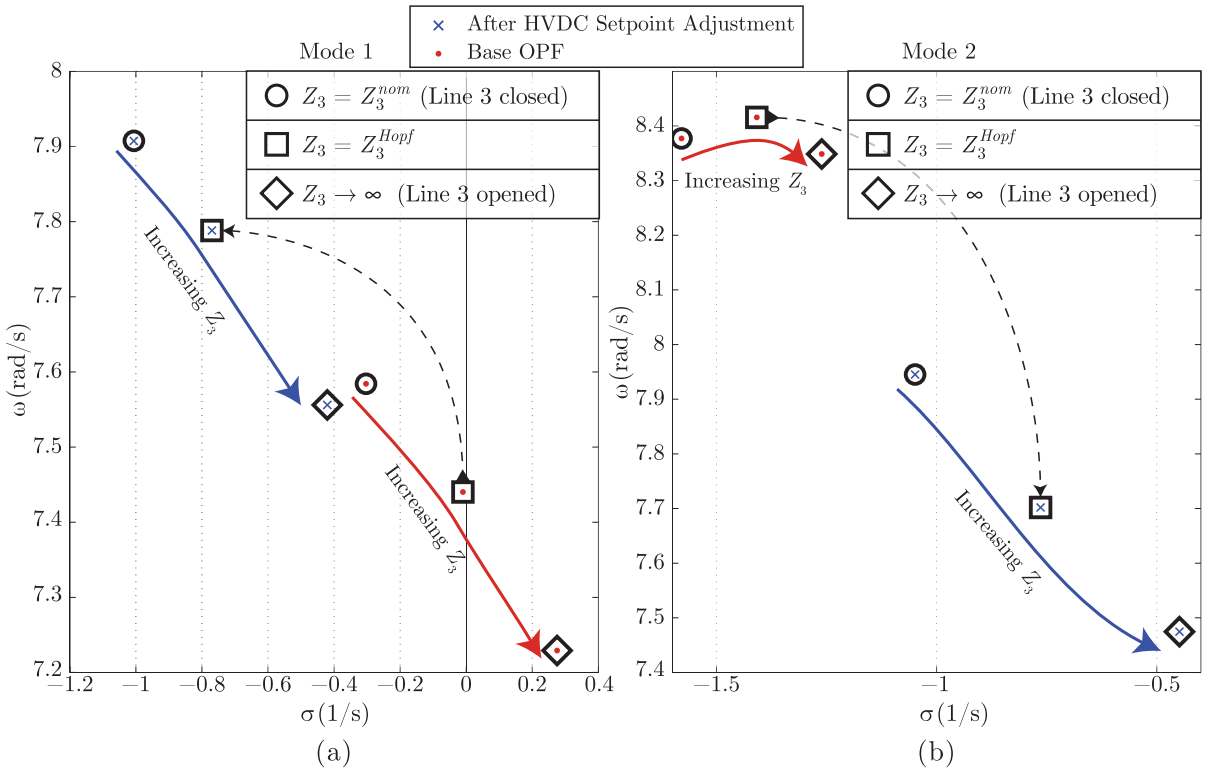

Figure 5.9: Loci of the eigenvalues associated with the least damped modes due to changes in line impedances. The dashed line indicates the change in operating conditions determined via the method detailed in Fig. 5.1

two eigenvalues associated with the least damped modes due to an increase in the line 3 impedance is depicted in Fig. 5.9. Fig. 5.9 shows that at the optimum operating point, mode 1 moves further away from the imaginary axis (increased damping) and mode 2 moves toward the imaginary axis (decreased damping). However, since the damping of the critical mode (mode 1) is increased, the system becomes more stable. Fig. 5.9 also shows that at the optimum operating point, for various line impedance values and even when the line three of each segment is disconnected ($Z_3 \to \infty$), the system remains stable at the new operating point.

5.6 Conclusions

This chapter proposes a new method, based on tuning the HVDC control set-points (reference values) of a DC-segmented AC system, to increase the stability margin. The system optimum operating point is obtained from an optimization process in which the set-points of the active power, transferred through the HVDC links, are the optimization variables. To solve the optimization problem, the sensitivity of the stability margin with respect to the controllable parameters at the Hopf point is used to determine the

direction in which the HVDC set-points should be changed and a line search is carried out to determine the optimum step size. At the optimum operating point, the eigenvalues associated with the least damped oscillatory modes are shifted away from the imaginary axis and the stability margin is improved.

The use of the optimum solution as a temporary operating point can help to restabilize the system subsequent to a change, e.g., a line outage. In the absence of the optimum solution, the system will definitely become unstable; however, the optimum solution directs the system toward a stable equilibrium. It can also be used as a preemptive operating point to increase the robustness of the system to changes, e.g., a line outage. Simulation results show that the proposed method can improve the stability margin and damping ratio caused by various events such as changes in the loading factor and line outages.

Chapter 6

Conclusions

6.1 Thesis Summary

This thesis proposes a control strategy for small-signal dynamic stability enhancement of a DC-segmented AC power system, in which the AC grid is decomposed into smaller AC segments connected through DC links, whereas the main power corridors among the segments are the DC links. Although there have been studies on the conceptual segmentation of the AC grid with HVDC links, to the best of our knowledge, this thesis is the first study which investigates the small-signal stability enhancement in such a configuration.

The proposed control strategy includes four control schemes based on HVDC supplementary control and modification of the operating condition of the HVDC system. Depending on the system characteristics, one or more of the proposed control schemes may be effective for the mitigation of the system oscillations.

Control scheme 1 provides a supplementary current control of an LCC HVDC link, based on MPC method to damp the oscillatory dynamics within a segment of a DC-segmented AC system. Control schemes 2 and 3 stabilize the system and provide coordinated LQG-based supplementary control to minimize the propagation of dynamics among the segments and selectively permit the propagation of the oscillations from the perturbed segment to the other segments, respectively. In control scheme 4, the Hopf bifurcation theory is utilized to steer the system away from instability, increase the stability margin and improve the damping of oscillatory modes by changing the HVDC set-points in the optimum direction determined based on the sensitivities of the Hopf stability margin to the set-point values of the HVDC links.

Since power system software tools exhibit limitations for advanced control design due to (i) inadequacy of a full model for the AC-DC system, (ii) lack of transparency of

model structures, (iii) inability to automatically generate a linearized state-space model, and (iv) inflexibility to accommodate custom-made models; this thesis also addresses the above issues and presents a methodology based on MATLAB/Simulink software to (i) systematically construct the nonlinear differential-algebraic model of an AC-DC system, and (ii) automatically extract a linearized state space model of the system. The developed framework is used for the design of the proposed control schemes of this thesis and a platform for the time-domain simulation of power system dynamics.

6.2 Thesis Conclusions

This thesis concludes that

- the developed MATLAB/Simulink-based framework (i) provides accurate time-domain simulations, (ii) enables for building an accurate nonlinear AC-DC power system model from the complete DAEs of the system (iii) automatically derives the linear model of the AC-DC system which can be used for linear control design, (iv) provides modeling flexibility, and (v) enables for easy inclusion of additional component models, e.g., those of FACTS controllers and custom-specified apparatus.

- the developed intra-segment MPC-based supplementary controller mitigates the dominant inter-area oscillatory modes of the AC-DC system while addressing actuator limitations and enabling operation closer to the system constraints on inputs, outputs and states. Study results show that the MPC-based supplementary controller has a time-varying gain which provides faster recovery times after faults compared to the traditional LQG-based supplementary controller. Furthermore, the MPC-based supplementary controller has satisfactory performance even if the communication delay is accounted for.

- the developed inter-segment LQG-based supplementary controllers improve the system small-signal stability by (i) minimizing the propagation of the oscillatory dynamics among the segments or (ii) selectively distributing the oscillatory dynamics among the segments. Furthermore, the sound performance of the inter-segment supplementary control schemes is maintained for various system operating points and fault locations.

- the developed HVDC control set-points tuning scheme increases the system stability margin and improves the damping ratio for Hopf bifurcations caused by various events such as changes in the loading factor and line impedances, e.g., line outages.

The optimum operating point, obtained from an optimization process, can be used as a temporary or permanent operating point to restabilize the system subsequent to a change, e.g., a line outage (which leads the system to instability) or to increase the robustness of the system to changes, e.g., a line outage, respectively.

6.3 Thesis Contributions

The contributions of this thesis are:

- developing a control strategy to damp oscillatory dynamics in a DC-segmented AC system including
  1. an intra-segment supplementary classical HVDC controller based on the MPC methodology.
  2. an inter-segment coordinated supplementary classical HVDC controller based on the LQG methodology to stabilize the system and minimize the transfer of oscillatory dynamics among the segments.
  3. an inter-segment coordinated supplementary classical HVDC controller based on the LQG methodology to distribute the oscillatory dynamics among the segments.
  4. an HVDC control system operating-point tuning scheme to shift the eigenvalues associated with the least damped oscillatory modes away from the imaginary axis and therefore enhance the stability margin.
- presenting a systematic approach to design each of the above control schemes.
- developing a MATLAB/Simulink-based framework for control design and time-domain simulation of the AC-DC power system transients.

6.4 Future Works

Further research in continuation of this work includes the following:

- inclusion of various component models to the MATLAB/Simulink-based framework, e.g., wind farms, power system stabilizers (PSS), and FACTS controllers.
- investigating the performance of other types of intra-segment supplementary controllers, e.g., adaptive [77] and robust controllers, to damp oscillatory dynamics.

- investigating the performance of other types of inter-segment supplementary controllers, e.g., adaptive and robust controllers, to improve system stability.
- developing a hierarchical control structure consisting of the proposed control schemes of this thesis, which coordinates all the proposed control schemes, to further improve the system stability. The hierarchical control structure should identify when each control scheme starts and stops coping with the oscillatory dynamics during a fault or disturbance scenario.

Appendix A

MPC Optimization Procedure

Consider a system of the form

$$\mathbf{x}(k+1) = \mathbf{A}\mathbf{x}(k) + \mathbf{B}\mathbf{u}(k) + \boldsymbol{\epsilon}(k), \tag{A.1}$$

$$\mathbf{y}(k) = \mathbf{C}\mathbf{x}(k) + \boldsymbol{\nu}(k). \tag{A.2}$$

In the optimization phase of the MPC control design, first the future outputs of the system are predicted and then the objective function is minimized. For prediction, the state space model of the system is used and the future outputs are calculated by

$$\begin{bmatrix} \mathbf{y}(k+1) \\ \vdots \\ \mathbf{y}(k+p) \end{bmatrix} = \mathbf{S}_x x(k) + \mathbf{S}_{u1}\mathbf{u}(k-1) + \mathbf{S}_u \begin{bmatrix} \Delta\mathbf{u}(k|k) \\ \vdots \\ \Delta\mathbf{u}(k+p-1|k) \end{bmatrix} \tag{A.3}$$

where

$$\mathbf{S}_x = \begin{bmatrix} \mathbf{CA} \\ \mathbf{CA}^2 \\ \vdots \\ \mathbf{CA}^p \end{bmatrix}, \mathbf{S}_{u1} = \begin{bmatrix} \mathbf{CB} \\ \mathbf{CB} + \mathbf{CAB} \\ \vdots \\ \sum_{h=0}^{p-1} \mathbf{CA}^h\mathbf{B} \end{bmatrix}, \tag{A.4}$$

$$\mathbf{S}_u = \begin{bmatrix} \mathbf{CB} & 0 & \dots & 0 \\ \mathbf{CB} + \mathbf{CAB} & \mathbf{CB} & \dots & 0 \\ \vdots & \vdots & \ddots & 0 \\ \sum_{h=0}^{p-1} \mathbf{CA}^h\mathbf{B} & \sum_{h=0}^{p-2} \mathbf{CA}^h\mathbf{B} & \dots & \mathbf{CB} \end{bmatrix}. \tag{A.5}$$

Substituting $\mathbf{y}(k+1), \ldots, \mathbf{y}(k+p)$ from (A.3) in (3.10)-(3.12), the MPC optimization problem is converted to a quadratic programming (QP) form given by

$$\min_{\mathbf{z}}(\mathbf{z}^T\mathbf{H}\mathbf{z} + 2\mathbf{f}^T\mathbf{z}), \tag{A.6}$$

subject to

$$\mathbf{b}_{min} \leq \Lambda\mathbf{z} \leq \mathbf{b}_{max}, \tag{A.7}$$

where

$$\mathbf{H} = \mathbf{W}_{\Delta_\mathbf{u}} + \mathbf{S}_u^T\mathbf{W}_y\mathbf{S}_u, \tag{A.8}$$

$$\mathbf{f}^T = \Big(\mathbf{u}(k-1)^T\mathbf{S}_{u1}^T + \mathbf{x}(k)^T\mathbf{S}_x^T - \begin{bmatrix}\mathbf{r}(k+1)\\ \vdots \\ \mathbf{r}(k+p)\end{bmatrix}^T\Big)\mathbf{W}_y\mathbf{S}_u, \tag{A.9}$$

$$\mathbf{z} = \begin{bmatrix}\Delta\mathbf{u}(k|k)\\ \vdots \\ \Delta\mathbf{u}(k+p-1|k)\end{bmatrix}, \tag{A.10}$$

$$\mathbf{W}_{\Delta\mathbf{u}} = diag(w_{0,1}^{\Delta u}, w_{0,2}^{\Delta u}, \ldots, w_{0,n_u}^{\Delta u}, \ldots, w_{p-1,n_u}^{\Delta u}), \tag{A.11}$$

$$\mathbf{W}_y = diag(w_{0,1}^{y}, w_{0,2}^{y}, \ldots, w_{0,n_y}^{y}, \ldots, w_{p-1,n_y}^{y}), \tag{A.12}$$

$$\Lambda = \begin{bmatrix}1 & 0 & \ldots & 0\\ 1 & 1 & \ldots & 0\\ \vdots & \vdots & \ddots & \vdots\\ 1 & 1 & \ldots & 1\\ & & \mathbf{I}_{p\times p} & \end{bmatrix}, \mathbf{b}_{\frac{max}{min}} = \begin{bmatrix}\mathbf{u}_{\frac{max}{min}}(0) - \mathbf{u}(k-1)\\ \vdots \\ \mathbf{u}_{\frac{max}{min}}(p-1) - \mathbf{u}(k-1)\\ \Delta\mathbf{u}_{\frac{max}{min}}(0)\\ \vdots \\ \Delta\mathbf{u}_{\frac{max}{min}}(p-1)\end{bmatrix}. \tag{A.13}$$

In the above equations $\mathbf{I}_{p\times p}$ is the identity matrix of size p.

Appendix B

System Differential-Algebraic Equations (DAEs)

This section describes how the HVDC system affects the AC-DC system algebraic equations in the optimization formulation of chapter 5. The algebraic and differential variables of the AC-DC system of (5.1) are also presented.

In (5.1), $g(\mathbf{x}, \mathbf{y}, \boldsymbol{\lambda}) = \mathbf{0}$ represents the algebraic equations of the stator circuitry of the SMs ($\mathbf{g}_{SM_{ac}}$), (2.1)-(2.2), network nodal equations ($\mathbf{g}_{NE}$), (B.1), coordinate transformation equations ($\mathbf{g}_{CO_{ac}}$) for all the generator buses, (2.30)-(2.33), and the DC algebraic equations. The network nodal algebraic equations represent the AC transmission network as

$$\bar{\mathbf{I}}_{inj} = \mathbf{Y}_{red}\bar{\mathbf{V}}_{inj}, \tag{B.1}$$

where $\bar{\mathbf{I}}_{inj}$ and $\bar{\mathbf{V}}_{inj}$ are the vectors of current and voltage phasors at the injection buses and $\mathbf{Y}_{red}$ is the reduced network admittance matrix [36]. Injection buses include the generator and HVDC buses. The DC algebraic equations include (B.2)-(B.3) for all HVDC buses.

$$P_{conv} - V_{D_{conv}} I_{D_{conv}} - V_{Q_{conv}} I_{Q_{conv}} = 0, \tag{B.2}$$

$$Q_{conv} - V_{Q_{conv}} I_{D_{conv}} + V_{D_{conv}} I_{Q_{conv}} = 0. \tag{B.3}$$

In this study, the vectors associated with the overall DAEs of a multi-machine AC-DC system represented in (5.1) are

$$\mathbf{x} = \begin{bmatrix} \mathbf{x}_1^T & \mathbf{x}_2^T & \dots & \mathbf{x}_{n_{TG}}^T \end{bmatrix}^T, \tag{B.4}$$

$$\mathbf{x}_i = [E_{qi}^{'}\, E_{di}^{'}\, \Psi_{1di}\, \Psi_{2qi}\, \delta_i\, \omega_i\, E_{fdi}\, R_{fi}\, V_{Ri}\, T_{svi}\, T_{mi}]^T, \tag{B.5}$$

$$\mathbf{y} = \begin{bmatrix} \mathbf{y}_{ac} \\ \mathbf{y}_{dc} \end{bmatrix}, \tag{B.6}$$

$$\mathbf{y}_{ac} = \begin{bmatrix} \mathbf{y}_{1_{ac}}^T & \mathbf{y}_{2_{ac}}^T & \cdots & \mathbf{y}_{n_{TG\,ac}}^T \end{bmatrix}^T, \tag{B.7}$$

$$\mathbf{y}_{i_{ac}} = \begin{bmatrix} V_{Di} & V_{Qi} & V_{di} & V_{qi} & I_{Di} & I_{Qi} & I_{di} & I_{qi} \end{bmatrix}^T, \tag{B.8}$$

$$\mathbf{y}_{dc} = \begin{bmatrix} \mathbf{y}_{1_{dc}}^T & \mathbf{y}_{2_{dc}}^T & \cdots & \mathbf{y}_{n_{dc\,dc}}^T \end{bmatrix}^T, \tag{B.9}$$

$$\mathbf{y}_{i_{dc}} = [V_{Di_{rec}}\, V_{Di_{inv}}\, V_{Qi_{rec}}\, V_{Qi_{inv}}\, I_{Di_{rec}}\, I_{Di_{inv}}\, I_{Qi_{rec}}\, I_{Qi_{inv}}]^T. \tag{B.10}$$

Appendix C

Calculating the Sensitivity of Stability Margin with Respect to Parameters

To demonstrate the procedure of calculating the sensitivity of the stability margin with respect to the parameters, a simple example where the damping ratio of the oscillatory modes has a closed form expression is provided. For a system of the form

$$\begin{bmatrix} \dot{x}_1 \\ \dot{x}_2 \end{bmatrix} = \begin{bmatrix} \alpha_1 - \alpha_2^2 & \beta \\ -\beta & \alpha_1 - \alpha_2^2 \end{bmatrix} \begin{bmatrix} x_1 \\ x_2 \end{bmatrix}, \alpha_2 \geq 0 \tag{C.1}$$

with $\lambda = [\mu \ p]^T$, $\mu = \alpha_1$, $p = \alpha_2$, $\mathbf{z} = [x_1 \ x_2]^T$, and $\mathbf{F_z} = \begin{bmatrix} \alpha_1 - \alpha_2^2 & \beta \\ -\beta & \alpha_1 - \alpha_2^2 \end{bmatrix}$, the eigenvalues are $\kappa = \alpha_1 - \alpha_2^2 \pm i\beta$. When α_1 increases from $\alpha_1^{(0)}$ to $\alpha_1^* = \alpha_2^2$, the system encounters a Hopf bifurcation and $\kappa^* = \pm i\beta^*$. Therefore, the Hopf bifurcation hypersurface can be written as:

$$\Sigma^{Hopf} = \left\{ [\alpha_1'^* \ \alpha_2'^*]^T : \alpha_1'^* = \alpha_2'^{*^2} \right\}.$$

The stability margin is then defined as $M = \alpha_1^* - \alpha_1^{(0)} = \alpha_2^{*^2} - \alpha_1^{(0)}$. The left and right eigenvectors corresponding to the Hopf point are $d = [\frac{1}{\sqrt{2}} \ \frac{-i}{\sqrt{2}}]$ and $e = [\frac{1}{\sqrt{2}} \ \frac{i}{\sqrt{2}}]^T$, respectively. In this example, $\mathbf{F_{zz}} = \mathbf{0}$ and $\mathbf{F_{z\lambda}}$ is a $2 \times 2 \times 2$ tensor where

$$\mathbf{F}_{\mathbf{z}\boldsymbol{\lambda}_1} = \begin{bmatrix} 1 & 0 \\ 0 & 1 \end{bmatrix}, \mathbf{F}_{\mathbf{z}\boldsymbol{\lambda}_2} = \begin{bmatrix} -2\alpha_2 & 0 \\ 0 & -2\alpha_2 \end{bmatrix},$$

$$n_{\alpha_1} = \mathbf{Re}([\frac{1}{\sqrt{2}} \ \frac{-i}{\sqrt{2}}]\begin{bmatrix} 1 & 0 \\ 0 & 1 \end{bmatrix}\begin{bmatrix} \frac{1}{\sqrt{2}} \\ \frac{i}{\sqrt{2}} \end{bmatrix}) = 1,$$

$$n_{\alpha_2} = \mathbf{Re}([\frac{1}{\sqrt{2}} \ \frac{-i}{\sqrt{2}}]\begin{bmatrix} -2\alpha_2 & 0 \\ 0 & -2\alpha_2 \end{bmatrix}\begin{bmatrix} \frac{1}{\sqrt{2}} \\ \frac{i}{\sqrt{2}} \end{bmatrix}) = -2\alpha_2,$$

$$\mathbf{N} = \begin{bmatrix} 1 \\ -2\alpha_2 \end{bmatrix},$$

$$M_{\alpha_2|\alpha_2^{(0)}} = 2\alpha_2^{(0)}.$$

$M_{\alpha_2|\alpha_2^{(0)}}$ indicates that in order to increase the stability margin, α_2 should be increased as expected, given that α_2^2 defines the limit on α_1 which results in a Hopf bifurcation. Increasing α_2 moves the eigenvalues further to the left of the imaginary axis and improves the damping ratio ($\zeta = \frac{\alpha_2^2 - \alpha_1}{\sqrt{\beta^2 + (\alpha_2^2 - \alpha_1)^2}}$).

Bibliography

[1] P. Kundur. *Power System Stability and Control*. McGraw-Hill, 1994.

[2] Final report on the August 14, 2003 blackout in the United States and Canada: causes and recommendations. [Online]: Available `https://reports.energy.gov/BlackoutFinal-Web.pdf`, 2004.

[3] C. Kim, V. K. Sood, G. Jang, S. Lim, and S. Lee. *HVDC Transmission: Power Conversion Applications in Power Systems*. IEEE Press-John Wiley and Sons (Asia) Pte Ltd, 2009.

[4] ABB HVDC reference projects. [Online]: Available `http://www.abb.com/industries/us/9AAF400191.aspx?country=00`, 2013.

[5] HVDC grid feasibility study. Technical report, Cigre Working Group B4-52, 2012.

[6] J. Pan, R. Nuqui, L. Tang, and P. Holmberg. VSC-HVDC control and application in meshed AC networks. In *IEEE Power Engineering Society General Meeting*, 2008.

[7] J. Pan, R. Nuqui, K. Srivastava, T. Jonsson, P. Holmberg, and Y. Hafner. AC grid with embedded VSC-HVDC for secure and efficient power delivery. In *IEEE Energy 2030 Conference*, pages 1–6, 2008.

[8] S. Zhou, J. Liang, J. Ekanayake, and N. Jenkins. Control of multi-terminal VSC-HVDC transmission system for offshore wind power generation. In *Proceedings of the 44th International Universities Power Engineering Conference (UPEC)*, pages 1–5, 2009.

[9] T. Ding, C. Zhang, Z. Hu, and Z. Duan. Coordinated control strategy for multi-terminal VSC-HVDC based wind farm interconnection. In *International Conference on Sustainable Power Generation and Supply (SUPERGEN)*, pages 1–6, 2009.

[10] D. Van Hertem and M. Ghandhari. Multi-terminal VSC-HVDC for the European supergrid: Obstacles. *Renewable and Sustainable Energy Reviews*, 14:3156–3163, 2010.

[11] H. Clark, A. Edris, M. El-Gasseir, K. Epp, A. Isaacs, and D. Woodford. Softening the blow of disturbances. *IEEE Power and Energy Magazine*, 6:30–41, 2008.

[12] F. Xinghao and J. H. Chow. Upgrading AC transmission to DC for maximum power transfer capacity. In *Power System Conference, 2008. MEPCON 2008. 12th International Middle-East*, pages 1–7, 2009.

[13] L. O. Barthold, H. Clark, and D. Woodford. Principles and applications of current-modulated HVDC transmission systems. In *Transmission and Distribution Conference and Exhibition, 2005/2006 IEEE PES*, pages 1429–1435, 2006.

[14] H. Clark, M. M. El-Gasseir, H. D. K. Epp, and A. Edris. The application of segmentation and grid shock absorber concept for reliable power grids. In *12th International Middle-East Power System Conference (MEPCON)*, pages 34–38, 2008.

[15] G. C. Loehr. Take my grid, please! A daring proposal for electric transmission. Technical report, IEEE HVDC-FACTS SUBCOMMITTEE MEETING, 2006 IEEE-PES Technical Committee Meeting, 2006.

[16] R. Eriksson and V. Knazkins. Nonlinear coordinated control of multiple HVDC links. In *IEEE 2nd International Power and Energy Conference*, pages 497–501, 2008.

[17] M. Noroozian, L. Angquist, M. Ghandhari, and G. Andersson. Improving power system dynamics by series-connected FACTS devices. *Power Delivery, IEEE Transactions on*, 12:1635 – 1641, 1997.

[18] Z. Huang, Y. Ni, C. M. Shen, F. F. Wu, S. Chen, and B. Zhang. Application of unified power flow controller in interconnected power systems-modeling, interface, control strategy, and case study. *Power Systems, IEEE Transactions on*, 15:817 – 824, 2000.

[19] S. Jiang, U. D. Annakkage, and A. M. Gole. A platform for validation of FACTS models. *Power Delivery, IEEE Transactions on*, 21:484 – 491, 2006.

[20] R. Rouco and F. L. Pagola. An eigenvalue sensitivity approach to location and controller design of controllable series capacitors for damping power system oscillations. *Power Systems, IEEE Transactions on*, 12:1660 – 1666, 1997.

[21] N. Martins, H. J. C. P. Pinto, and J. J. Paserba. Using a TCSC for line power scheduling and system oscillation damping-small signal and transient stability studies. In *IEEE Power Engineering Society Winter Meeting*, pages 1455–1461, 2000.

[22] S. Arabi, G. J. Rogers, D. Y. Wong, P. Kundur, and M. G. Lauby. Small signal stability program analysis of SVC and HVDC in AC power systems. *Power Systems, IEEE Transactions on*, 6:1147 – 1153, 1991.

[23] I. Kamwa, J. Beland, G. Trudel, R. Grondin, C. Lafond, and D. McNabb. Wide-area monitoring and control at Hydro-Quebec: past, present and future. In *IEEE Power Engineering Society General Meeting*, 2006.

[24] M. R. Iravani, P. L. Dandeno, K. H. Nguyen, D. Zhu, and D. Maratukulam. Applications of static phase shifters in power systems. *Power Delivery, IEEE Transactions on*, 9:1600 – 1608, 1994.

[25] K. V. Patil, J. Senthil, J. Jiang, and R. M. Mathur. Application of STATCOM for damping torsional oscillations in series compensated AC systems. *Energy Conversion, IEEE Transactions on*, 13:237 – 243, 1998.

[26] P. Kundur, M. Klein, G. J. Rogers, and M. S. Zywno. Application of power system stabilizers for enhancement of overall system stability. *Power Systems, IEEE Transactions on*, 4:614 – 626, 1989.

[27] I. Kamwa, R. Grondin, and Y. Hebert. Wide-area measurement based stabilizing control of large power systems-a decentralized/hierarchical approach. *Power Systems, IEEE Transactions on*, 16:136 – 153, 2001.

[28] D. Dotta, A. S. e Silva, and I. C. Decker. Wide-area measurements-based two-level control design considering signal transmission delay. *Power Systems, IEEE Transactions on*, 24(1):208–216, 2009.

[29] M. Xiao-ming, Z. Yao, G. Lin, and W. Xiao-chen. Coordinated control of interarea oscillation in the China Southern power grid. *Power Systems, IEEE Transactions on*, 21:845 – 852, 2006.

[30] I. Kamwa, G. Trudel, and L. Gerin-Lajoie. Robust design and coordination of multiple damping controllers using nonlinear constrained optimization. *Power Systems, IEEE Transactions on*, 15:1084 – 1092, 2000.

[31] P. Zhang and A. H. Coonick. Coordinated synthesis of PSS parameters in multi-machine power systems using the method of inequalities applied to genetic algorithms. *Power Systems, IEEE Transactions on*, 15:811 – 816, 2000.

[32] R. L. Cresap and W. A. Mittelstadt. Small-signal modulation of the Pacific HVDC intertie. *Power Apparatus and Systems, IEEE Transactions on*, 95:536 – 541, 1976.

[33] T. Smed and G. Anderson. Utilising HVDC to damp power oscillations. *Power Delivery, IEEE Transactions on*, 8:620–627, 1993.

[34] J. H. Chow and K. W. Cheung. A toolbox for power system dynamics and control engineering education and research. *Power Systems, IEEE Transactions on*, 7:1559–1564, 1992.

[35] MATLAB. *The MathWorks Simulink User's Guide R2012a*. The MathWorks Inc., 2010.

[36] P. W. Sauer and M. A. Pai. *Power System Dynamics and Stability*. Prentice-Hall, Inc, 1998.

[37] R. Preece and J. V. Milanovic. Comparison of dynamic performance of meshed networks with different types of HVDC lines. In *9th IET International Conference on AC and DC Power Transmission, 2010. ACDC.*, 2010.

[38] F. Milano. *Power System Modeling and Scripting*. Springer, 2010.

[39] R. M. Brandt, U. D. Annakkage, D. P. Brandt, and N. Kshatriya. Validation of a two-time step HVDC transient stability simulation model including detailed HVDC controls and DC line L/R dynamics. In *IEEE Power Engineering Society General Meeting*, 2006.

[40] Y. Y. Hong and W. C. Wu. New approach using optimization for tuning parameters of power system stabilizers. *Energy Conversion, IEEE Transactions on*, 14:780–786, 1999.

[41] X. Lei, E. N. Lerch, and D. Povh. Optimization and coordination of damping controls for improving system dynamic performance. *Power Systems, IEEE Transactions on*, 16:473–480, 2001.

[42] A. L. B. Do Bomfim, G. N. Taranto, and D. M. Falcao. Simultaneous tuning of power system damping controllers using genetic algorithms. *Power Systems, IEEE Transactions on*, 15:163–169, 2000.

[43] Y. N. Yu, K. Vongsuriya, and L. N. Wedman. Application of an optimal control theory to a power system. *Power Apparatus and Systems, IEEE Transactions on*, PAS-89:55–62, 1970.

[44] Y. Fan, C. Chen, and W. Xitian. Observer-based decentralized control of inter-area oscillation in multi-infeed HVDC system. In *IEEE/PES Transmission and Distribution Conference and Exposition*, pages 1–4, 2008.

[45] W. D. Yang, Z. Xu, and Z. X. Han. A co-ordinated large-signal modulation strategy for multi-infeed HVDC systems. In *Seventh International Conference on AC-DC Power Transmission*, pages 338–343, 2002.

[46] D. Q. Mayne, J. B. Rawlings, C. V. Rao, and P. O. M. Scokaert. Constrained model predictive control: Stability and optimality. *Automatica*, 36:789–814, 2000.

[47] S. Joe Qin and T. A. Badgwell. A survey of industrial model predictive control technology. *Control Engineering Practice*, 11:733–764, 2003.

[48] G. Welch and G. Bishop. An introduction to the Kalman filter. Technical Report TR 95-041, University of North Carolina, Department of Computer Science, 1995.

[49] E. F. Camacho and C. Bordons. *Model Predictive Control*. Springer, 2004.

[50] C. Schmid and L. T. Biegler. Quadratic programming methods for reduced hessian SQP. *Computers and Chemical Engineering*, 18:817–832, 1994.

[51] J. H. Chow, J. J. Sanchez-Gasca, H. Ren, and S. Wang. Power system damping controller design-using multiple input signals. *IEEE Control Systems*, 20(4):82–90, 2000.

[52] K. Morrison, L. Wang, and P. Kundur. Power system security assessment. *IEEE Power and Energy Magazine*, 2(5):30–30, 2004.

[53] R. Schainker, P. Miller, W. Dubbelday, P. Hirsch, and G. Zhang. Realtime dynamic security assessment. *Power Systems, IEEE Transactions on*, 4(2):51–58, 2006.

[54] K. Morrison, L. Wang, and P. Kundur. Implementation of online security assessment. *IEEE Power and Energy Magazine*, 4(5):46–59, 2006.

[55] G. De Nicolao, L. Magni, and R. Scattolini. On the robustness of receding horizon control with terminal constraints. *Automatic Control, IEEE Transactions on*, 41(3):451–453, 1996.

[56] H. Michalska and D. Q. Mayne. Robust receding horizon control of constrained nonlinear systems. *Automatic Control, IEEE Transactions on*, 38(11):1623–1633, 1993.

[57] G. De Nicolao, L. Magni, and R. Scattolini. Stability and robustness of nonlinear receding horizon control. *Journal of Nonlinear model predictive control*, 26:3–22, 2000.

[58] P. M. Anderson and A. A. Fouad. *Power System Control and Stability*. IEEE Press, 1994.

[59] R. E. Kalman. Mathematical description of linear systems. *SIAM Journal on Control and Optimization*, 1:152–192, 1963.

[60] S. Skogestad and I. Postlethwaite. *Multivariable Feedback Control: Analysis and Design*. John Wiley and Sons, 1996.

[61] Y. Halevi. Stable LQG controllers. *IEEE Transactions on Automatic Control*, 39:2104–2106, 1994.

[62] C. D. Vournas, M. A. Pai, and P. W. Sauer. The effect of automatic voltage regulation on the bifurcation evolution in power systems. *Power Systems, IEEE Transactions on*, 11:1683–1688, 1996.

[63] A. A. P. Lerm and A. Silva. Avoiding Hopf bifurcations in power systems via setpoints tuning. *Power Systems, IEEE Transactions on*, 19:1076–1084, 2004.

[64] A. A. P. Lerm. Control of Hopf bifurcation in multi-area power systems via a secondary voltage regulation scheme. In *Power Engineering Society Summer Meeting, 2002 IEEE*, pages 1615–1620, 2002.

[65] S. Wang, Y. Yi, Q. Jiang, X. Chen, and Y. Cao. On-line control of Hopf bifurcations in power systems. In *IEEE Power and Energy Society General Meeting - Conversion and Delivery of Electrical Energy in the 21st Century*, pages 1–7, 2008.

[66] N. Mithulananthan, C. A. Canizares, J. Reeve, and G. J. Rogers. Comparison of PSS, SVC, and STATCOM controllers for damping power system oscillations. *Power Systems, IEEE Transactions on*, 18:786–792, 2003.

[67] A. I. Zecevic and D. M. Miljkovic. The effects of generation redispatch on Hopf bifurcations in electric power systems. *Circuits and Systems I: Fundamental Theory and Applications, IEEE Transactions on*, 49:1180–1186, 2002.

[68] H. Zhenyu, N. Zhou, F. Tuffner, C. Yousu, D. Trudnowski, W. Mittelstadt, J. Hauer, and J. Dagle. Improving small signal stability through operating point adjustment. In *IEEE Power and Energy Society General Meeting*, pages 1–8, 2010.

[69] S. K. M. Kodsi and C. A. Canizares. Application of a stability-constrained optimal power flow to tuning of oscillation controls in competitive electricity markets. *Power Systems, IEEE Transactions on*, 22:1944–1954, 2007.

[70] G. G. Lage, G. R. M. da Costa, and C. A. Canizares. Limitations of assigning general critical values to voltage stability indices in voltage-stability-constrained optimal power flows. In *2012 IEEE International Conference on Power System Technology (POWERCON)*, pages 1–6, 2012.

[71] A. A. P. Lerm. Control of Hopf bifurcation in power systems via a generation redispatch. In *IEEE Porto Power Tech Proceedings*, pages 1–8, 2001.

[72] Independent Electricity System Operator. Review of the dispatch algorithm's compliance with market rules. [Online]: Available `http://www.ieso.ca/imoweb/pubs/dso-2012.pdf`, June 2012.

[73] I. Dobson, F. Alvarado, and C. L. DeMarco. Sensitivity of Hopf bifurcations to power system parameters. In *Proceedings of the 31st Conference on Decision and Control*, 1992.

[74] T. Smed. Feasible eigenvalue sensitivity for large power systems. *Power Systems, IEEE Transactions on*, 8:555–563, 1993.

[75] M. Lotfalian, R. Schlueter, D. Idizior, P. Rusche, S. Tedeschi, L. Shu, and A. Yazdankhah. Inertial, governor, and AGC/economic dispatch load flow simulations of loss of generation contingencies. *Power Apparatus and Systems, IEEE Transactions on*, PAS-104:3020–3028, 1985.

[76] D. J. N. Limebeer, R. G. Harley, and M. A. Lahoud. Suppressing subsynchronous resonance with static filters. *Generation, Transmission and Distribution, IEE Proceedings C*, 128:33–44, 1981.

[77] S. Lefebvre, M. Saad, and R. Hurteau. Adaptive control for HVDC power transmission systems. *Power Apparatus and Systems, IEEE Transactions on*, PAS-104:2329–2335, 1985.